Techniques for Reducing Beam-Induced Damage in Electron Microscopy

by

Navid Abedzadeh

S.M. Electrical Engineering, Massachusetts Institute of Technology (2018)

B.ASc. Nanotechnology Engineering, University of Waterloo (2015)

Submitted to the Department of Electrical Engineering and Computer Science
in Partial Fulfillment of the Requirements for the Degree of

Doctor of Philosophy

at the

MASSACHUSETTS INSTITUTE OF TECHNOLOGY

May 2022

Author: .....

Department of Electrical Engineering and Computer Science
May 13, 2022

Certified by .....

Karl K. Berggren
Professor of Electrical Engineering and Computer Science
Thesis Supervisor

Accepted by .....

Leslie A. Kolodziejski
Professor of Electrical Engineering and Computer Science
Chair, Department Committee on Graduate Students

Techniques for Reducing Beam-Induced Damage in Electron Microscopy

by

Navid Abedzadeh

Submitted to the Department of Electrical Engineering and Computer Science
on May 13, 2022, in Partial Fulfillment of the Requirements for the Degree of
Doctor of Philosophy

Abstract

Imaging biomolecules in their natural state at an atomic scale resolution is crucial to the understanding of such molecules. Under the banner of Quantum Electron Microscopy (QEM), two novel electron microscopy schemes have been proposed to achieve nanometer-scale resolution while practically eliminating beam-induced damage to biological samples. The first approach is based on a quantum mechanical principle known as interaction-free measurement (IFM) and the second approach is known as multipass transmission electron microscopy, a type of phase contrast imaging in which the probe electrons transmit through a thin sample multiple times. I have been involved in the development of major components of the IFM scheme such as electron mirrors and diffractive electron mirrors for lossless splitting of incident electron beams. Furthermore, I have made major progress in developing various components of the simplest form of multipass microscopy which could be performed in a scanning electron microscope. I developed a theoretical framework to understand the effects of beam shift and hydrocarbon contamination in multipass microscopy and the limit they place on the choice of sample in this scheme. This experiment would be the first demonstration of contrast enhancement due to multipassing in an electron microscope.

Thesis Supervisor: Karl K. Berggren

Title: Professor of Electrical Engineering and Computer Science

Acknowledgments

The work presented in this thesis would not have been possible without the support and guidance of my research supervisor, Prof. Karl K. Berggren. I will forever be grateful to him.

I would like to thank Dr. Phillip "Donnie" Keathley, the co-PI of the group. Aside from Donnie's expertise in optics being an invaluable asset to the group, I greatly benefited from conversations with him about my research and otherwise.

I would like to thank my thesis committee: Prof. Karl K. Berggren, Prof. Peter Hagelstein, Dr. Phillip D. Keathley, and Prof. William Putnam. Their thoughtful comments and advice are greatly appreciated.

I would like to thank Prof. Marc Baldo, my academic advisor, for his guidance and support.

I would like to acknowledge Dr. Chung-Soo Kim and Prof. Richard Hobbs, my first two postdocs when I joined the group. Richie was the person who sparked in interest in me regarding the QEM project and Chung-Soo taught me almost everything I know about constructing electron optical experiments. I thank them for their patience with me.

I would like to acknowledge my collaboration with Dr. Rudolf Tromp who graciously agreed to test my samples in his LEEM system. His experiments and the consequent analyses that he provided to me expanded my understanding of my own research and made this work stronger. I thank him for that.

I would like to acknowledge our collaborators in the QEM team: Stanford University, TU Delft and University of Erlangen. Specifically, I would like to thank Prof. Pieter Kruit of TU delft whose endless knowledge and expertise in all things electron optics were an indispensable asset to me. I would also like to thank Prof. Mark Kasevich (Stanford) and Prof. Thomas Juffmann (University of Vienna) for their help and guidance with the double-pass experiment.

I would like to thank my friend and colleague John Simonaitis who helped me with almost every step of the experiments that I present in this thesis. His expertise in electrical engineering was invaluable to my work.

I would like to acknowledge the many helpful conversations I have had throughout the years with current and past members of the QNN team including Dr. Akshay Agarwal, Dr. Marco Turchetti, Dr. Stewart Koppell, Dr. Mina Bionta, Dr. Brenden Butters and Dr. Murat Onen. Also

from the QNN group, I would like thank Marco Colangelo who never hesitated to help and guide me with nanofabrication. I would like to thank Dr. Maurice Krielaart my collaboration with whom started years ago before he joined MIT. I have always benefited from his theoretical and experimental expertise.

I would like to thank the admins of the group, Dorothy Fleischer and Rinske Wijtmans, who make sure that everything goes smoothly behind the scenes.

I would like to thank the technical staff of the NanoStructures Laboratory at MIT, Jamse (Jim) Daley and Mark Mondol who helped me at the cleanroom. Jim also helped me evaporate thin films on my samples. I would also like to thank a former member Dr. Timothy (Tim) Savas who trained me in the cleanroom and taught me about the Lloyd's mirror.

I would like to acknowledge the help and support from the staff at the EECS Graduate Office: Janet Fischer, Kathleen McCoy, Alicia Duarte and the Department Committee Chair, Prof. Leslie Kolodziejski.

I thank Gordon and Betty Moore Foundation for supporting the Quantum Electron Microscope project.

I thank the Natural Sciences and Engineering Research Council of Canada (NSERC) for partial funding of my graduate studies.

I would like to thank my best friend Dr. Emily Toomey whom I met seven years ago during our first day at MIT. Ever since that fateful day, I have enjoyed her company and our thousands of conversations.

I would like to thank the many friends who helped and supported me throughout my MIT years: Marco Colangelo, Marco Turchetti, John Simonaitis, Murat Onen, Owen Medeiros, Matthew Yeung, Rana Isak, Erik and Monique Eisenach, Josue Lopez, and Luciana Castellan.

I would like to thank my parents. Their unwavering support and belief in me helped me go beyond what I imagined possible. I will never forget their sacrifice of giving up on a comfortable life and immigrating to Canada to give me and my sister better lives. I will always be in their debt.

Finally, I would like to thank my amazing girlfriend, Dr. Maria Pabon. Meeting her about two years ago was one of the greatest things that happened during my PhD. I am truly lucky to have her. I thank her for her constant love and support. I would also like to acknowledge our dog Milo

who brings so much joy into our lives.

List of Figures

Contents

Chapter 1

Avoiding radiation damage in electron microscopy

1.1 Introduction

High-resolution imaging of biomolecules down to atomic-scale is critical to our understanding of biological processes such as protein folding. Due to diffraction, the smallest feature size resolvable using optical microscopy is often larger than biomolecules of interest such as DNA, RNA, or proteins. Since the de Broglie wavelength of electrons is much smaller than that of photons at typical energies, electron microscopy has been the tool of choice for resolving atomic-scale features over the past several decades. The scanning electron microscope (SEM) is the most widely used tool for achieving nanometer (nm) resolution images while the transmission electron microscope (TEM) and the scanning transmission electron microscope (STEM), operating at higher electron energies, can offer resolutions down to a fraction of a nanometer [1, 2, 3, 4]. And yet, imaging of biological molecules at atomic-scale resolution remains a challenge [5].

The diffraction limit in electron microscopy is quite often not the real limiting factor when it comes to the imaging of biological specimens. Instead, the damage caused by the highly energetic electrons incident on the fragile biological specimen tends to occur faster than one could produce an image with atomic resolution. Egerton and Malac have identified heating, electrostatic charging, radiolysis, displacement and sputtering as some of the mechanisms through which an energetic electron beam could partially damage or destroy a biological molecule [6]. For a given

specimen, the two main factors in determining the extent of beam-induced damage have been shown to be the electron beam energy and the electron dose [7]. Most conventional approaches to "low-damage" electron microscopy are based on optimizing one or both of these factors.

1.2 Conventional approaches

Although in general, higher-energy electrons are capable of imparting more severe radiation damage to samples, there are subtleties involved which will be discussed in this section. The impact of electron dose goes as one would expect: the higher the dose, the more damage the sample will sustain.

1.2.1 Low-energy approaches

Among the examples of electron microscopy approaches which attempt to lower radiation damage by using low-energy electrons are low-energy electron microscopy (LEEM) [8, 9, 10] and low-energy electron in-line holography [11, 12]. In practice, the landing energy in LEEM is kept within 0-100 eV to stay below energy thresholds for different damage mechanisms for various samples. The ionization energy of C–H bonds, prominent in all biological samples, is 4.2 eV [13]. At this electron energy, the de Broglie wavelength is 0.6 nm. However, taking other effects such as optics, specimen characterization and current requirements into account, the theoretical resolution of LEEM is estimated to be in the range of 2-4 nm [9, 14]. Meanwhile, it has been observed that even ultra low-energy electrons (0-4 eV) could, in sufficient doses, cause single strand breaks in DNA molecules [15]. Another important consideration in microscopy with ultra low-energy electrons is that at a certain point, the gains from small de Broglie wavelengths of electrons begin to dissipate. [13, 16].

1.2.2 Low-does approaches

As one would expect, by lowering the dose of probing electrons, one could lower the damage imparted onto the sample. However, due to the quantum nature of electrons, the information in electron microscopy is shot-noise limited. In practice, this noise appears as randomly distributed

black and white pixels on a micrograph, and at low electron doses, the noise dominates the useful information that the image could hold. Phase contrast imaging, turning electrons' phase information into amplitude contrast, is known to be the most dose-efficient conventional technique for imaging weak-phase objects such as biological samples [17, 18]. Phase contrast imaging in electron microscopy is achieved in conventional TEMs by deliberately introducing some defocus or other aberrations or by the use of phase plates [19] or through in-line [11] or off-axis holography [20]. Ptychography is another technique that has been shown to achieve relatively dose-efficient phase contrast imaging by taking advantage of phase information in the overlapping diffraction disks formed in STEM [18]. However, although these techniques achieve better dose-efficiencies ($\sim 10^6$ e^-/nm^2) [18] compared to conventional amplitude-contrast imaging, to prevent damage to biological samples, electron dose must be limited to $\sim 10^3$ e^-/nm^2 [21]. At such low beam currents, current phase contrast imaging techniques are not capable of producing acceptable image contrast for weak-phased objects such as biomolecules.

To avoid this problem, cryo-electron microscopy (cryo-EM) was developed to use large ensembles of identical molecules as opposed to imaging an individual molecule, effectively dividing the risk of damage between many molecules. Imaging each individual molecule at a very low electron dose would not allow for production of images with acceptable SNR; however, by averaging over thousands of such low-SNR images, cryo-EM is capable of creating apparently high-SNR images of biological molecules at an atomic-scale resolution [22]. Although a technological breakthrough [23], cryo-EM does not address a fundamental challenge in electron microscopy; namely, it does not allow for atomic-scale imaging of an individual biomolecule without damaging it. This limitation becomes obvious when one considers the fact that not all molecules could be prepared with thousands of their exact copies inside the same sample. Furthermore, conformational information of the individual molecule is lost in the averaging process [22, 24].

1.3 Quantum Electron Microscopy

As daunting a hurdle as shot-noise is in microscopy, it is not a deeply-rooted limit of physical measurement but rather a consequence of the employed classical detection scheme [25]. It has been demonstrated that through the use of the principles of quantum mechanics such as entan-

gled photons or squeezed photon states one can perform sub-shot-noise measurements [26, 27]. Unfortunately, when it comes to electron microscopy, most of these quantum mechanical advancements have been largely unfulfilled. Under the banner of Quantum Electron Microscopy (QEM) two novel electron microscopy schemes have been proposed to achieve low-damage imaging of biological specimens by overcoming the shot-noise limit. The first of these schemes relies on interaction-free measurement with electrons while the second one relies on multipass transmission electron microscopy.

1.3.1 Interaction-free measurement

Interaction-free measurement (IFM) is based on a thought experiment proposed by Elitzur and Vaidman (EV) who theorized that the presence or absence of an opaque object could be detected without directly interacting with it [28]. Their measurement scheme relied on the preservation or destruction of quantum superposition between the states of an elementary particle such as a photon or an electron. To setup the problem, they assumed a Mach-Zehnder interferometer similar to the one shown in Fig. 1.1. It is possible, by setting up the interferometer's arm lengths just right, to ensure that single photons entering the system from the left, will always, with 100% certainty, be detected by detector D_1 (bright port). This task is done by taking advantage of the wave nature of photons at the second beam-splitter; namely, due to destructive interference at detector D_2 (dark port), the photons will always emerge at D_1. At this point, if an opaque sample is placed in one of the arms of the interferometer as shown in Fig. 1.1, three possible outcomes could occur:

(i) no detector clicks

(ii) detector D_2 clicks

(iii) detector D_1 clicks

In the case of no detector clicking, we can conclude that the input photon was absorbed (or scattered) by the opaque sample. This outcome would occur 50% of the time — when the input photon is transmitted, rather than reflected at the first 50-50 beam splitter. Therefore, the case of no click could be thought of as *interaction* with or *damage* to the sample.

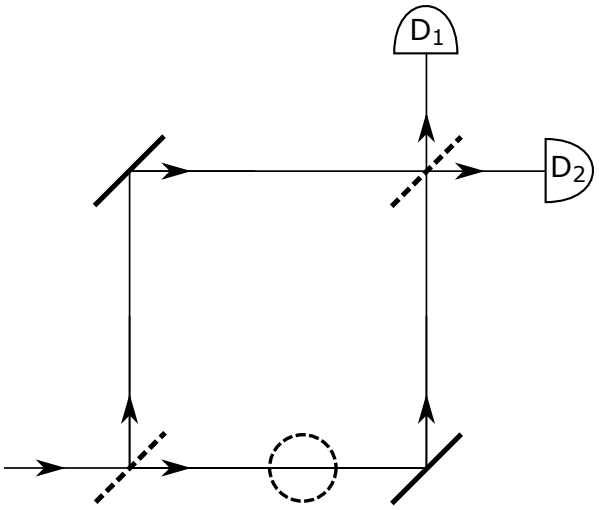

Figure 1.1: Schematic of a Mach-Zehnder interferometer. Dashed lines represent 50-50 beam splitters; solid thick lines represent mirrors; dashed circle represents an opaque object. In the absence of an object, the optical path lengths have been set up such that a single photon entering the interferometer from the bottom left port would always end up at detector D_1 (bright port). The presence of an opaque object placed on one of the arms of the interferometer could destroy the interference even when the photon is not absorbed by the object (detection at D_2, dark port), enabling interaction-free measurement [28]

Now, consider the case where detector D_2 clicks. Note that the initial setup ensured that in the absence of any sample, all photons would end up at D_1. Therefore, a click at D_2 indicates that not only there must have been a sample in one of the arms of the interferometer, but also that the sample did not absorb the photon for if it had, the photon would not have caused a click at D_2. This case constitutes as interaction-free measurement.

Finally, consider the case where detector D_1 clicks. Keeping in mind that the initial state of the interferometer was set up such that in the absence of a sample, D_1 always clicked, this outcome does not tell us much. It could be that D_1 clicks because there is no sample or that it clicks because the photon reflected off of both beam splitters.

Note that the wave-particle duality of a single quantum is central to IFM: in the absence of an object, the wave nature of a single photon ensures, through destructive interference, that only the bright port (D_1) clicks. However, in the presence of an object, it is the indivisibility of the single photon that guarantees that in the event of a click at the dark port (D_2), IFM has occurred [29].

An obvious shortcoming of the EV scheme is its low efficiency: IFM outcomes occur only

quarter of the time while damage to the sample occurs half the time. To solve this problem, Kwiat *et al.* proposed a higher-efficiency IFM scheme [29] whereby they envisioned a resonant cavity housing at its center a beam splitter with a sufficiently large reflectivity. As can be seen in Fig. 1.2, the sample to be probed is placed on the right side of the beam splitter while a single photon is in-coupled on the left side of the beam splitter. The cavity is designed such that in the absence of an opaque sample, constructive interference would lead to a gradual transfer of photon probability density from the left side to the right side of the cavity. After a set number of reflections, upon measurement, the photon will be found on the right side of the cavity — analogous to a click at detector D_1 in the original EV scheme. However, the presence of an opaque sample on the right side would prevent this gradual accumulation of probability density on the right side while the low transmissivity of the beam splitter ensures an arbitrarily small probability of damage to the sample. By analogy to the original EV scheme, finding the photon on the left side after a set number of reflection is like a click at D_2, i.e. IFM. All together, this improved version of the experiment could lead to IFM outcomes with an efficiency arbitrarily close to 100% and damage probability arbitrarily close to 0% — just increase the number of reflection as well as the reflectivity of the beam splitter.

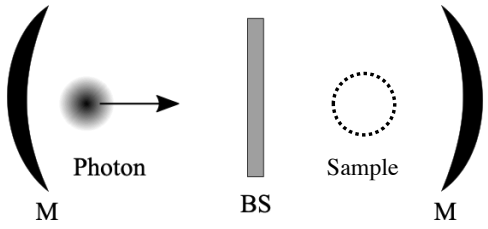

Figure 1.2: Schematic of high efficiency interaction-free measurement inside a cavity bounded by two mirrors (M) and a beam splitter (BS) of reflectivity $R = \cos^2\left(\frac{\pi}{2N}\right)$. When an opaque object is placed on the right side of the cavity, the photon will be found on the left side of the cavity after a large number of round trips N, indicating the presence of the object without directly interacting with it [29].

It is worth noting that the Kwiat scheme constitutes as a form of discrete quantum Zeno effect — the repeated coherent interrogation of a region that might contain a sample modifies the evolution of the wave function and in the case that an opaque object is present, the transference of the wave function to the sample side is inhibited [29].

A conclusive demonstration of IFM with electrons would require a number of scientific in-

novations such as the realization of a coherent electron cavity and a lossless means to split and re-couple electrons. The first theoretical attempt was made by Putnam and Yanik in 2009 [30]. Several more practical approaches to designing IFM-based electron microscopes were introduced in 2016 by Kruit *et al* [31]. In the course of my research, I followed one such design which involves an electron cavity in the volume between two parallel electron mirrors and a diffractive electron mirror to split and recouple the electrons. Note that these components, two mirrors and a beam splitter, are the bare minimum requirements to conduct IFM. In practice, many more components are required to execute this scheme with electrons.

Figure 1.3 showcases the major components of Kruit *et al*'s QEM design in schematic form. In this design, the electron is coupled into the cavity when a short positive voltage pulse is applied to the upper gated mirror, lowering the potential barrier and creating an opening for the incoming electron. After the dissipation of this voltage pulse, the gated mirror's voltage restores to its original value — closed gate state — and the mirror behaves like a flat mirror. The duration of this voltage pulse must be shorter than a few nanoseconds — the round trip time of the in-coupled electron inside the cavity. Although crucial to the final QEM instrument, the development of the gated electron mirror is not discussed in this thesis. However, my research into flat electron mirrors and their implementation inside an SEM is discussed in Chapter 2.

Another notable aspect of this design is the use of a diffractive electron mirror (DEM), a biased diffraction grating which combines the mirror element with the beam splitter by taking advantage of electron diffraction to split the incident beam. This component is discussed in detail in Chapter 3. To make matters more complicated, in the final instrument, there is a need for integration of the DEM and the bottom gated mirror such that upon completing the requisite number of round trips, the electron would be out-coupled for measurement. The proposed plan for this integration requires the DEM to be fabricated on top of a thin, suspended silicon nitride (SiN) film. In its closed mode, the DEM acts as a mirror and a beam splitter while in its open mode, the voltage applied to the DEM would drop, allowing the electron to pass through the thin SiN film with minimal inelastic scattering. This integration was beyond the scope of my research.

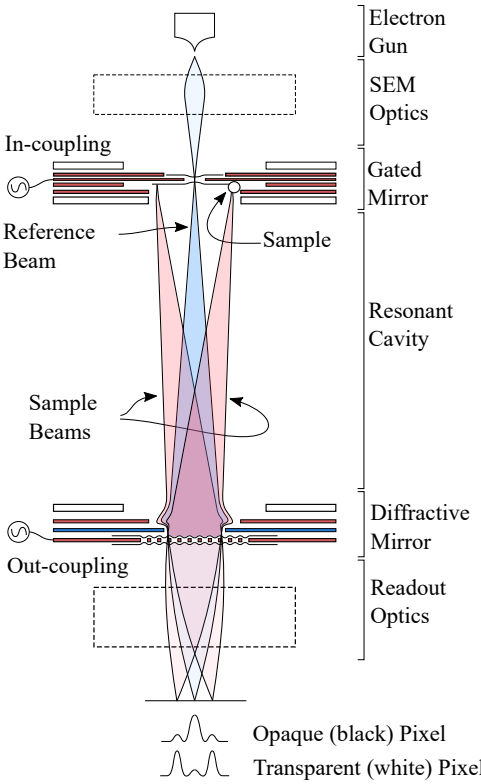

Figure 1.3: Design for an interaction-free measurement scheme with electrons (IFM QEM). This design consists of an electron cavity mounted inside a conventional field emission SEM. A diffractive electron mirror, analogous to the beam splitter in the optical setup, splits/re-couples the electron beam. In the absence of an opaque object (white pixel), the electron probability density would have maxima corresponding to the sample beams. With an opaque sample present (black pixel), consequent measurement on the electron would indicate that the electron exhibited the reference beam inside the cavity. Figure courtesy of Marco Turchetti.

1.3.2 Multipass

In conventional phase contrast TEM, a phase object is placed in the path of a high-energy electron beam. Upon passing through the sample, the electrons undergo a certain amount of phase shift. Through various methods [19], it is possible to convert the available phase information to contrast information. What is of particular importance here is the fact that under the weak-phase approximation (valid for most biological samples), larger phase shifts lead to more contrast information — images with higher signal-to-noise ratios. Now considering the fact that biological samples, mostly comprised of lower-atomic-number elements, tend to impart a very small phase shift onto the passing high-energy electrons. As such, producing high resolution, high contrast images of biological specimens remains challenging and largely unfulfilled. One obvious approach would

be to send a larger number of electrons through the sample in order to extract more information out of the phase object (sample); however, this approach would inevitably lead to more beam-induced damage to the sample. Multipass TEM bypasses this problem by passing the same probe electrons multiple times through the sample, gradually obtaining more phase information while not increasing the probability of damage quite as much.

One might wonder what makes multipass TEM's reusing of transmitted electrons less damaging than an equivalent electron dose in conventional phase contrast TEM. For the comparison to be valid, one must keep either the signal-to-noise ratio (SNR) or the dose constant across the two schemes. In general, a large SNR with a small dose is desirable. Here, let us assume that the number of electrons used are constant across the two schemes. In other words, in conventional phase contrast TEM, we pass N electrons through the sample once, while in multipass TEM, we pass N electrons through the sample m times. Furthermore, let us assume that the main source of noise in both scenarios is shot noise, the average value of which is equal to the square of the number of electrons:

$$\langle \text{noise} \rangle = \sqrt{N}. \tag{1.1}$$

The average value of signal in the case of conventional TEM (single pass, $m = 1$) could be expressed as the amount of phase shift, $\Delta\phi$, picked up by each electron:

$$\langle \text{signal}_{m=1} \rangle = N\Delta\phi. \tag{1.2}$$

SNR could then be expressed for single-pass TEM as

$$\text{SNR}_{m=1} = \sqrt{N}\Delta\phi. \tag{1.3}$$

It is useful for this analysis to consider a critical SNR of 1. By equating the SNR to 1 in Eq. 1.7, we get

$$N_{0_{m=1}} = \frac{1}{(\Delta\phi)^2} \tag{1.4}$$

where N_0 is the critical dose to achieve SNR $= 1$. Next, knowing that damage probability is

proportional to dose, we can can write

$$\text{Damage}_{m=1} \propto \frac{1}{(\Delta\phi)^2}. \tag{1.5}$$

A similar analysis for multipass TEM with N electrons and m passes through the sample could be used to find the same average noise but a scaled average signal:

$$\langle \text{signal}_{m>1} \rangle = mN\Delta\phi. \tag{1.6}$$

The SNR for multipass would therefore also scale with the number of passes m:

$$\text{SNR}_{m>1} = m\sqrt{N}\Delta\phi. \tag{1.7}$$

For $\text{SNR}_{\text{critical}} = 1$, the critical dose could be found:

$$N_{0_{m>1}} = \frac{1}{m^2(\Delta\phi)^2}. \tag{1.8}$$

Damage probability also scales with the number of passes. This is due to the fact that with each pass, we expose the sample to the risk of damage. Therefore, damage in multipass TEM could be expressed as:

$$\text{Damage}_{m>1} \propto m\frac{1}{m^2(\Delta\phi)^2}. \tag{1.9}$$

From Eqs. 1.5 and 1.9 one could find the ratio of damage between conventional phase contrast TEM and multipass TEM given a constant electron dose and SNR:

$$\frac{\text{Damage}_{m>1}}{\text{Damage}_{m=1}} = \frac{1}{m}. \tag{1.10}$$

In other words, for fixed dose and SNR, at large enough number of passes, the damage advantage of multipass TEM becomes significant when compared with conventional phase contrast TEM.

Multipass microscopy, already demonstrated to beat the shot-noise limit in optical microscopy [32], is another avenue which holds promise for sub-shot-noise imaging in electron microscopy. It has been shown that multipass achieves similar gains in SNR as entangled-probe-particle mea-

surements do for a given damage, without a need for entangled particles [32]. Theoretically, this gain in SNR could be achieved in multipass TEM as suggested by the simulation results shown in Fig. 1.4 adapted from [33].

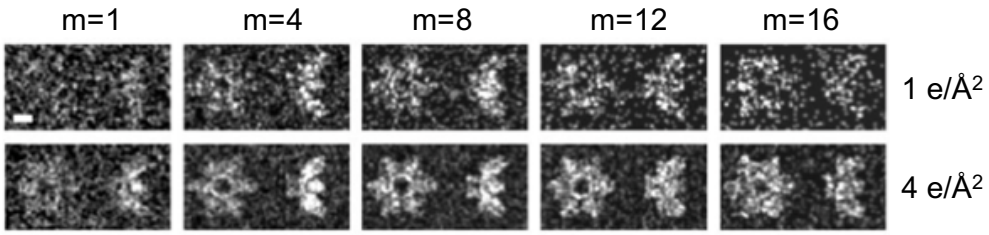

Figure 1.4: Multi-pass TEM simulation of the HIV-1 Gag protein structure under two different projections for 300 keV electrons at two different doses of 1 e/Å^2 and 4 e/Å^2. For a given dose, more electron passes through the sample (m) leads to increased image contrast. Figure adapted from [33]

Similar to IFM with electrons, multipass TEM relies on an electron cavity consisting of two electron mirrors between which electrons bounce back and fourth to interact with a sample. Figure 1.5, borrowed from [33], shows a conceptual schematic of multipass TEM in which the sample lies in between two gated electron mirrors. Similar to the case of IFM with electrons, the gated electron mirror is perhaps the most challenging component of this design since it must transition between being a flat mirror and a gate through which electrons can pass in time scales of a few nanoseconds. In Chapter 4, I outline the theory behind the simplest form of multipass TEM which could be attempted in a scanning electron microscope (SEM) with only two passes through the sample (double-pass, m=2). Finally, I will present the various components and challenges associated with the experimental demonstration of double-pass.

1.4 Structure of this thesis

In Chapter 2, I present my work on the development of tetrode electron mirrors for use inside an SEM. I demonstrate simultaneous imaging of the top and the bottom surfaces of a sample using the tetrode electron mirror. Furthermore, I discuss various regimes of mirror operation, the properties of images produced under each regime, and their potential applications.

In Chapter 3, I present my work on the diffractive electron mirror (DEM), a proposed scheme to coherently and losslessly split electron beams. I heavily drew from the theoretical work by

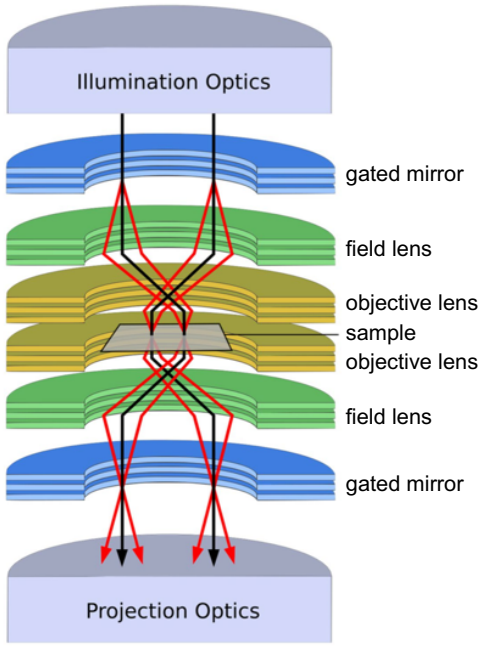

Figure 1.5: Conceptual schematic of a multipass TEM design. The upper gated mirror during its "open" phase, allows electrons to be coupled into the cavity before quickly closing the voltage barrier and becoming a flat mirror. The in-coupled electrons bounce back and fourth multiple times in order to accumulate phase shift after each pass through the sample. Finally, the lower gated mirror opens to let the electrons out towards the projection optics. Figure adapted from [33].

Krielaart and Kruit in this chapter. I present results from experiments performed in our SEM at MIT as well as in a LEEM system at IBM. Neither of these experimental setups yielded results that could be confidently deemed as coherent diffraction. Finally, I examine the current hypotheses for the null results.

In Chapter 4, I discuss my approach to attempting the simplest form of multipass TEM in an SEM without an electron cavity. I present the experimental design as well as my progress in developing various components of this experiment such as the detection scheme, the test sample, and the laser heater to avoid hydrocarbon contamination. Furthermore, I analyze the deleterious effects of beam shift during this experiment and the effective limit it places on how small the period of the phase grating test sample could be.

Chapter 2

Imaging with electrostatic electron mirrors in SEM

The material in this chapter is taken directly and without modification from my published work in Ultramicroscopy [34]. The authors as they appear on this publication are as follows: Navid Abedzadeh, M.A.R Krielaart, Chung-Soo Kim, John Simonaitis, Richard Hobbs, Pieter Kruit, and Karl K. Berggren.

Abstract: The use of electron mirrors in aberration correction and surface-sensitive microscopy techniques such as low-energy electron microscopy has been established. However, in this work, by implementing an easy to construct, fully electrostatic electron mirror system under a sample in a conventional scanning electron microscope (SEM), we present a new imaging scheme which allows us to form scanned images of the top and bottom surfaces of the sample simultaneously. We believe that this imaging scheme could be of great value to the field of in-situ SEM which has been limited to observation of dynamic changes such as crack propagation and other surface phenomena on one side of samples at a time. We analyze the image properties when using a flat versus a concave electron mirror system and discuss two different regimes of operation. In addition to in-situ SEM, we foresee that our imaging scheme could open up avenues toward spherical aberration correction by the use of electron mirrors in SEMs without the need for complex beam separators.

2.1 Introduction

In its simplest form, an electron mirror creates an electric field in which incident electrons slow down to a complete standstill before being accelerated away in the opposite direction. Multi-electrode electron mirrors have been used in mirror electron microscopy (MEM) [35, 36, 37, 38, 39] and low-energy electron microscopy (LEEM) [40, 9, 41, 42]. Today, aside from LEEM, the most prominent application of electron mirrors is in chromatic and spherical aberration correction [43, 44, 45]. More recently, designs for novel electron microscopy schemes that lower beam-induced damage to fragile biological samples have been proposed. Under the banner of quantum electron microscopy (QEM), two such designs have been proposed that are based on electron cavities consisting of two electron mirrors between which electrons would reflect back and forth to probe a sample multiple times [31, 33, 46]. Implementation of electron mirrors in SEMs has not been widely reported. In this work, we explore the use of tunable, easy to construct electron mirror systems in an SEM under different imaging regimes.

During the development of electron mirrors for the QEM project, we incorporated a fully electrostatic multi-electrode mirror in a conventional SEM, and found a new imaging scheme in which it is possible to produce simultaneous scanned images of top and bottom surfaces of perforated samples. As shown in Fig. 2.1(a) a focused electron beam scans a perforated sample, e.g. a transmission electron microscope (TEM) copper mesh. Where the sample obstructs this scanning probe, a scanned image of the top surface of the sample is produced. At scan positions where the probe is not obstructed, the electrons pass through the sample plane towards the electron mirror system placed below. This electron mirror system which consists of a mirror electrode and three electrodes to form a lens is commonly referred to as a tetrode mirror and in this case reflects and refocuses the beam back on the sample plane. Where this reflected scanning probe strikes the bottom surface of the sample, a scanned image of the bottom surface of the sample is produced in the same micrograph. This is due to the fact that the greyscale value of each pixel in an SEM micrograph is dependent only on the number of secondary electrons detected while the beam was dwelling over that pixel as opposed to the source of those secondary electrons. The end result is an SEM micrograph in which the top and bottom surfaces of the sample are simultaneously visible as shown in Fig. 2.1(b). It must be noted that we employ the term “simultaneous” loosely

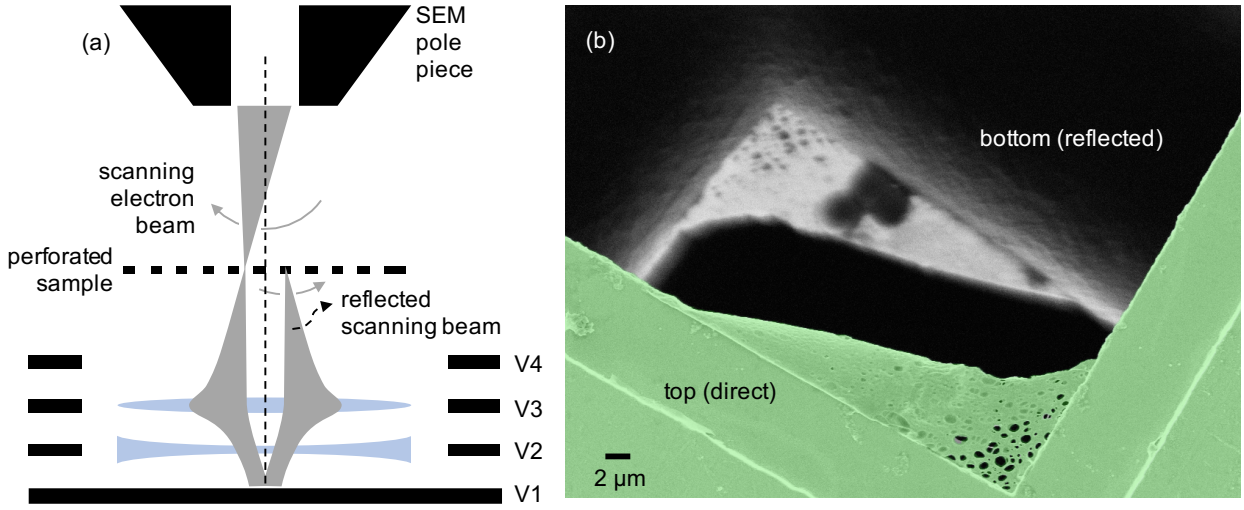

Figure 2.1: Simultaneous imaging of the top and bottom surfaces of a sample in SEM. (a) Schematic of the optical design and electron ray trajectory: the tetrode mirror system, comprised of electrodes V1-V4, reflects a scanning electron beam where it is not obstructed by the perforated sample, and refocuses it on the bottom surface of the sample. The schematic is not drawn to scale and the light optics lenses (blue) are drawn only as an analogy. (b) SEM micrograph showing the top (colorized in green) and bottom (greyscale) surfaces of a sample within the same frame. The sample shown here consists of a suspended holey carbon membrane that is attached to a TEM copper grid. The reflected image shows particles on the bottom side of the membrane which are not visible in the direct image.

here; depending on the scan speed, there is microseconds to milliseconds between when the top and the bottom images form. In this work, we refer to the image of the top surface as the direct image and the image of the bottom surface as the reflected image.

A similar imaging technique in a different context was demonstrated by Crewe et al. using custom made scan coils and a magnetic lens [47]. In our approach, we take advantage of a fully electrostatic tetrode mirror, which could be easily retrofitted in most conventional SEMs. Furthermore, since the operation of our mirror does not rely on a magnetic immersion lens, the sample could be held at a nominally field-free region which is of interest for investigation of magnetic samples.

The most immediate application of our imaging technique is its potential use in in-situ SEM where it is of interest to image dynamic changes such as crack propagation or melting of a sample [48, 49]. Currently, in-situ SEM is limited to capturing changes on one side of the sample at a time. The multi-electrode mirror and the imaging scheme described in this work could be used

to simultaneously capture dynamic changes on both surfaces of a thin sample. Incorporation of this mirror system in an SEM chamber could be easily achieved due to its relatively small form factor and ease of assembly and operation. For achieving the highest possible resolution, careful design, machining and assembly of multi-electrode electron mirrors are crucial. We demonstrate that even without meeting those stringent requirements, a simple electron mirror system constructed with off-the-shelf components is nonetheless capable of reflecting the beam and forming a scanning focused probe of about 100 nm diameter to produce reflected images.

Another potential application for our imaging scheme is mirror aberration correction. Conventional mirror aberration correction has relied on separation of the incident (uncorrected) and the reflected (corrected) beams by means of either Y-separators [43, 44] or 90-degree separators [50]. These separators often introduce chromatic dispersions of their own to the beam. Although later designs, notably one by R. Tromp [45] eliminated these chromatic dispersions, such beam separators remain complex and are generally not designed for use in SEMs. More recently, Dohi and Kruit showed a promising design in which two miniaturized electron mirrors along with small-angle deflectors are used in order to correct the aberrations of an SEM objective lens [51]. However, their approach requires significant modifications to the electron column.

Our imaging scheme could lead to a fundamentally different approach to mirror aberration correction by eliminating the need for deflectors of any kind. In a similar imaging setup as shown in Fig. 2.1(a), one could replace the flat mirror electrode (V1) with an aperture electrode in order to create a tunable curved mirror potential. With the mirror voltages tuned correctly, one could image the bottom surface of a perforated sample with a spherical- and/or chromatic-aberration-corrected probe without the need for beam separators. This simple approach comes with a number of limitations chief among which is the need for samples that do not block the entire field of view. It must be noted that although we demonstrate image resolution improvements when using a concave five-electrode mirror system, we do not attempt rigorous aberration correction which is an involved process and hence beyond the scope of this work.

2.2 Experimental design

To produce simultaneous scanned images of the top and bottom surfaces of a sample in an SEM, maintaining focus at the sample plane for the beam on its way down as well as its way up is a crucial requirement. To achieve this requirement, two electron optical elements in addition to the ones the SEM is already equipped with are needed: (1) an electron mirror, and (2) an electron lens that is positioned between the mirror and the sample plane. The mirror reflects the incident beam and redirects it towards the sample plane while the lens refocuses the reflected beam. Depending on the strength of the lens element, however, this requirement could be met in one of two different regimes of operation. These regimes are defined by whether the back-focal plane or the image plane of the mirror system coincides with the sample plane. Furthermore, the mirror element could be flat or curved depending on the intended application and voltage restrictions.

In this work, as shown in Fig. 2.1(a), we refer to the mirror system electrodes, as V1 through V4 from bottom to top. Electrode V1 is a flat stainless steel plate to which a negative bias larger in magnitude than that of the acceleration voltage of the beam is applied. Electrode V2, sometimes referred to as the cap electrode, is an electrode with an aperture at its center. It acts as a field limiting aperture for the mirror electric field and due to the curved field lines near its aperture, effectively behaves as a diverging lens [39, 52]. For simplicity, we keep this electrode grounded. The role of electrode V3 is to provide a positive lensing effect, allowing for refocusing of the reflected electron beam onto the bottom surface of the sample. Hence, we refer to this electrode as the lens electrode. Finally, the grounded electrode V4 completes the lens component of the tetrode mirror and minimizes the amount of stray fields from the electrodes below.

2.2.1 Mechanical considerations

The form factor of the electron mirror system is dictated by the available space inside the SEM, mechanical and machining constraints, as well as electric field and electron optical requirements. With these considerations, we opted to use commercially available stainless steel plates with regularly spaced through-holes in order to construct the mirror stack. Figure 2.2 shows these plates in grey, assembled using plastic bolts and alumina balls. The plates, acquired from Kimball Physics Inc., are 0.635 mm (0.025 inches) thick and the through-holes are 3.175 mm (0.125 inches)

in diameter, including the central hole which is the aperture through which the electron beam passes. The alumina balls provide electrical insulation between the electrodes, as well as stability to the structure by fixing the plates in the lateral direction under the vertical pressure from the bolts. We used alumina balls of radius 3.5 mm which set the separation between the electrodes to about 1.35 mm. The minimum distance between the sample plane and the mirror electrode is set by the thickness of the mirror stack and the sample holder and in our case is about 25 mm. The distance between the sample and the SEM objective lens (working distance) was set to about 7 mm.

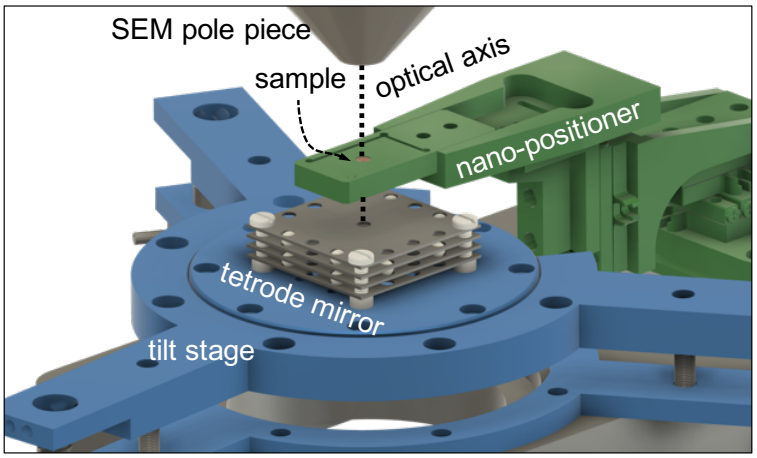

Figure 2.2: Experimental setup: 3D CAD diagram of a perforated sample (copper grid) mounted on a three-axis nano-positioner (green). The sample is held above a tetrode electron mirror (gray) which is mounted on a tilt stage (blue). Both the nano-stage and the tilt stage are mounted on a three axis translation stage which is connected to the SEM door (not shown). The optical axis of the tetrode mirror is aligned with that of the SEM objective lens. The square plates (gray) used in the mirror assembly are 5 cm on each side.

The alignment of the mirror stack with respect to the SEM objective lens is crucial to the performance of the electron mirror. For this alignment, we made use of separate translation and tilt stages, as shown in Fig. 2.2. The sample was mounted on a dedicated 3-axis nano-positioner which provided independent positioning of the sample relative to the mirror stack. In order to ensure that the mirror is level, the mirror stack was mounted on a piezo-controlled tilt stage. Both the nano-positioner and the tilt stage were in turn mounted on a 3-axis translation stage which is attached to the SEM door inside the vacuum chamber.

We used a variety of samples in our experiments. However, in all cases these samples were only partially obstructing the field of view, allowing for electrons to pass through undisturbed at

some scan positions. Furthermore, all samples were relatively thin (tens of micrometers) and had nanometer to micrometer features to resolve during imaging. Among these samples were TEM copper grids of varying mesh sizes, and holey carbon films on copper grids.

The SEM used in our experiment is a Zeiss LEO 1525 with a Schottky electron source with an energy spread of about 1 eV. To allow for construction of taller experimental setups inside the SEM chamber, we replaced the original SEM door and the 5-axis stage with a custom door and a 3-axis translation stage with a smaller form factor. The appropriate flanges for high-voltage connection in order to bias the mirror electrodes were incorporated in the custom SEM door.

2.2.2 Electron optical considerations

Electric field and electron ray trajectory simulations performed on the commercial software Lorentz 2E provided insight into the approximate voltages for each electrode in the mirror system. From there, minor voltage adjustments were needed in order to obtain an in-focus micrograph. For consistency, we performed all experiments in this work at the beam acceleration voltage of 3 kV, beam current of about 10 pA, and beam convergence angle of about 2 mrad. The upper limit for the beam acceleration voltage is set by how large of a voltage could be safely applied to the mirror system.

The voltage applied to the mirror electrode defines the plane of reflection. In the case of the flat tetrode mirror, a schematic of which is shown in Figs. 2.1(a) and 2.2, the magnitude of this voltage must be at least as large as the beam acceleration voltage to avoid collision between the electrons and the mirror electrode. In practice, we must account for the inherent roughness in the surface of the stainless steel mirror plate which leads to a non-uniform electric field near the surface. We set the magnitude of this negative bias to 20-50 V above the acceleration voltage of the electron beam in order to ensure that the beam is reflected on a flat potential surface. Failure to do so could result in distortion and loss of image resolution. In the case of the five-electrode aperture mirror used for curved mirror operation, a much larger negative voltage applied to the mirror electrode is required in order to achieve a potential more negative than beam acceleration voltage at the center of the aperture.

The cap electrode V2 was grounded in order to terminate the electric field lines formed above the mirror electrode V1. In certain applications, it is beneficial to apply a positive bias to the cap

electrode in order to increase the magnitude of the electric field in the mirror region. However, in our experiment, high electric fields are not crucial and we opted for a grounded cap electrode which lowers the risk of electrical breakdown between the mirror and the cap electrodes.

The voltage applied to the lens electrode (V3) controls the convergence angle of the beam entering and exiting the mirror system. It is worth noting that the effects of the lens voltage are not fully decoupled from the cap electrode (V2). In other words, an increase in the positive voltage of the cap electrode leads to more severe diverging action which must be counteracted with a larger voltage on the lens electrode to maintain a fixed focal length. By applying a negative voltage to the lens electrode (V3) we opted for a decelerating lens which achieves the same focal length at a smaller voltage compared to an accelerating lens, reducing the risk of electric breakdown in the setup.

Typical factors limiting SEM image resolution include the probe size, sample material, acceleration voltage and for slow scans, beam and stage stability [53]. In our imaging scheme, since the sample and the beam energy for the incident and the reflected beams are the same, the image resolution comes down to the probe size before and after reflection. With the added complexity of the electron mirror system as well as the added optical path in our imaging scheme, the reflected beam is expected to suffer from various additional aberrations and distortions beyond the ones that the SEM objective lens imparts on the incident beam. Therefore, it would be reasonable to expect a larger probe size and hence poorer resolution of the reflected image (bottom) compared to the direct (top) image. The aberrations of the tetrode mirror can be kept relatively small when the spacing between the mirror and cap electrodes is small compared to the radius of the aperture in the cap electrode [54]; however, this requires the use of micromachined optics which we do not pursue in this work, as we focus here on an "off-the-shelf" approach.

2.3 Results and discussion

In this section, we discuss imaging under different electron optical regimes defined by the trajectory of the reflected beam as determined by the strength of the lens element within the mirror system. Furthermore, we present reflected images produced with a curved mirror constructed with five electrodes. We analyze image properties associated with each regime and experimental

setup.

2.3.1 Broad beam over the mirror surface

The first regime of operation is defined by the tetrode mirror voltages set such that for a given beam energy, the back-focal plane of the mirror and lens coincides with the sample plane. An incoming electron beam that is focused on the sample plane by the objective lens of the SEM will enter the tetrode mirror and consequently be spread out over the mirror electrode. After reflection, the beam will be refocused on the sample plane. Figure 2.3(a) shows a schematic of the electron trajectory and Figure 2.3(b) shows an example of a micrograph produced under this regime of operation.

A property of images obtained in this regime is point symmetry about the optical axis between the direct image and the reflected image. The reason is apparent from the electron trajectory schematic: the incident and the reflected beams pass through the sample plane at the same distance to but opposite sides of the optical axis. This is especially useful when performing in-situ microscopy on samples both sides of whom undergo dynamic changes that are of interest.

Ideally, our imaging scheme in this regime would produce the best image resolution over the entire field of view with the SEM settings and the mirror voltages set such that the pivot point of the SEM scan is imaged on the reflection plane. The SEM pivot point is a virtual stationary point below the scan coils around which the scanning beam hinges. By imaging this point at the spot where the optical axis meets the reflection plane, we could ensure that the broad beam remains stationary over the reflection plane near the optical axis as opposed to scanning over the surface of the mirror which could lead to increased aberrations and distortions. Unfortunately, meeting this condition is not trivial in our Zeiss SEM due to software overrides for currents applied to the scan coils and the objective lens.

Since the incident beam is spread out over the mirror plane, this regime of operation is also useful for applications in which manipulations to the electron wave front using an electron mirror is of interest. An example of such application is electron diffraction by means of a diffractive electron mirror [55] which is of interest in novel low-damage electron microscopy schemes [31, 56]. Another example of an application in which this regime of operation is used is mirror aberration correction which will be discussed in Section 2.3.3.

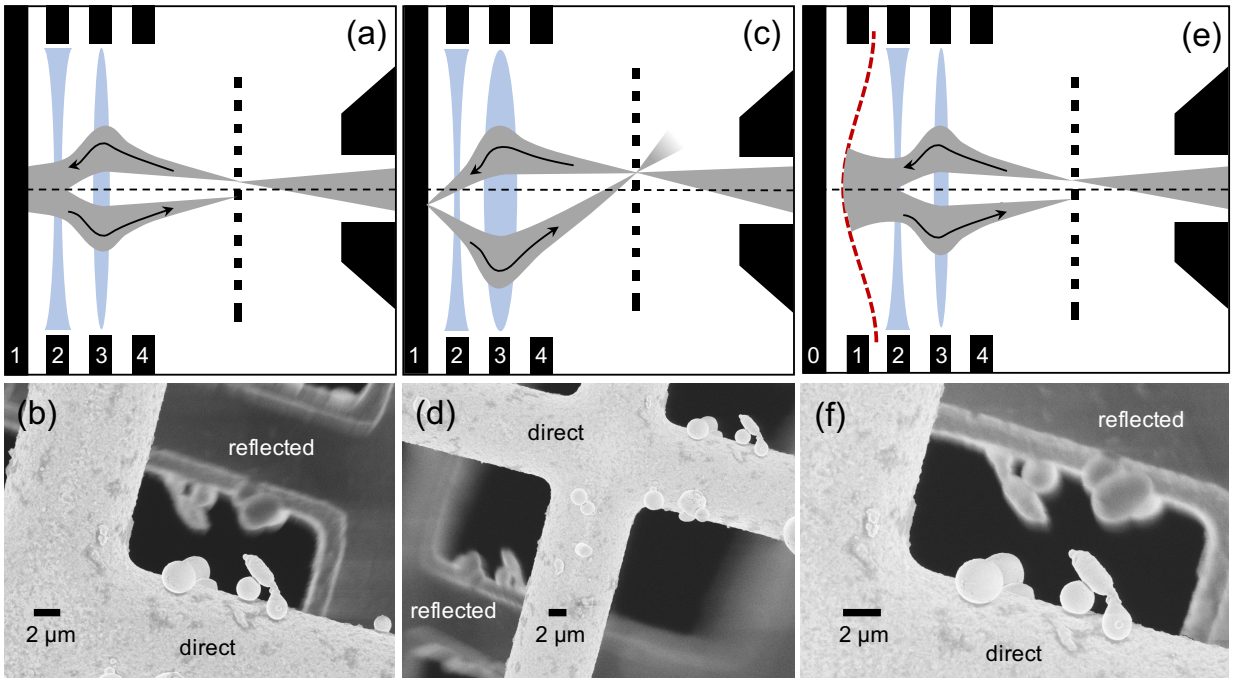

Figure 2.3: Schematic electron trajectories and their corresponding SEM micrographs obtained under different regimes of mirror imaging. (a)-(b) Tetrode mirror voltages tuned such that the back-focal plane of the mirror system coincides with the sample plane (dashed line) resulting in an SEM micrograph with point symmetry between the direct and reflected images. (c)-(d) Tetrode mirror voltages tuned such that the image plane of the mirror system is conjugated with the sample plane. Note that the micrograph in (d) demonstrates a misaligned experimental setup while the schematic in (c) corresponds to a perfectly aligned system such that the incident and the reflected beams pass through the exact same spot on the sample plane. (e)-(f) Five-electrode mirror with voltages tuned such that the incident beam is reflected on a curved potential surface (red dashed line). Careful engineering of the curved potential could eliminate the spherical aberration of the objective lens in the reflected beam (not attempted here). Schematics are not drawn to scale. All scale bars are 2 µm.

2.3.2 Focused beam over the mirror surface

Another mode of operation is realized by increasing the positive lens strength of the mirror system until the image plane coincides with the sample plane. In other words, the lens component images the sample plane onto the mirror electrode, and vice versa. We achieve this regime electrically by keeping all settings constant while increasing the magnitude of the voltage applied to the lens electrode (V3) compared to the voltage required for the first regime discussed above. The electron trajectory schematic for this regime is shown in Fig. 2.3(c), from which it becomes clear that the incident and the reflected beams pass through the sample plane at exactly the same point and hence for an opaque sample, no (scanned) image of the bottom surface could form since the object would block the path of the incident beam whose reflection would have otherwise reached the bottom side of the sample. In practice, we only observe simultaneous images of top and bottom surfaces of a sample in this regime when there is a slight misalignment between the optical axes of the mirror system and that of the SEM objective lens. This misalignment could be achieved by a tilt or lateral shift of the mirror. Figure 2.3(d) shows an SEM micrograph obtained under this regime when there was a misalignment in the setup.

A noteworthy difference between the first regime of operation with a broad beam over the mirror and this regime is regarding where the pivot point of the SEM scan is imaged. With the sample plane being imaged over the reflection plane in the latter regime, the pivot point by definition cannot be imaged on the reflection plane, causing the focused beam to scan over the reflection plane. This deviation from the optical axis near the reflection plane leads to significant aberrations and distortions which are apparent in the peripheries of the reflected image in Fig. 2.3(d).

Although not very useful for producing scanned images of a sample, this regime of operation is of particular interest for applications such as multi-pass electron microscopy where multiple interactions between a stationary beam and a weak phase object inside an electron cavity could lead to more efficient phase contrast imaging [33]. It is crucial for multi-pass electron microscopy that the reflected beam be re-imaged exactly back on the sample in order for the beam to accrue the correct phase. Although in multi-pass electron microscopy the beam incident on the sample must not be focused, the mirror settings, namely having the sample on the image plane of the

tetrode mirror, is identical to what we present in this work.

2.3.3 Broad beam over a curved mirror potential

Appropriately curved electron mirrors have been shown to be capable of inducing spherical and chromatic aberrations with sufficiently negative coefficients in order to cancel out the aberrations of the objective lens [43, 45]. Here, without attempting to demonstrate quantitative cancellation of spherical aberration, we show that the same imaging technique discussed above could be performed with a curved mirror. To create a curved mirror, we added an aperture electrode to our previous tetrode mirror assembly. In this new five-electrode system, as shown in Fig. 2.3(e), a concave reflection plane is formed by applying a negative bias to the aperture electrode V1. Similar to the first regime where the beam is spread over the mirror, the voltages are tuned such that the back-focal plane of the mirror system coincides with the sample plane.

The voltage applied to the flat electrode in this setup (V0) could control the curvature of the reflection potential surface while keeping the mirror voltage (V1) constant. A negative voltage applied to the flat electrode V0 would make the curved mirror potential less concave whereas a positive V0 would create a more concave mirror potential surface. Although, in principle, the flat electrode V0 is not necessary to produce a curved mirror potential, in practice, it proves useful for two reasons: it acts as a flat surface terminating the field lines emanating from the mirror electrode (V1), and also when biased negatively, it allows for an identical mirror potential curvature under a lower V1 voltage for less chance of electric breakdown.

A concave mirror potential has some positive lensing effect which must be accounted for by applying a smaller voltage to the lens electrode (V3) in order to maintain a focused beam on the sample plane. In addition, the curvature of the mirror dictates the amount of spherical and chromatic aberrations imparted on the beam. These considerations create a multi-variable problem and in practice, sweeping the phase space of various voltages in an electron trajectory simulation is the efficient way to ensure minimization of spherical and chromatic aberrations while maintaining a set focal length as shown by Tromp et al. [45].

The reflected image shown in Fig. 2.3(f) shows qualitative resolution improvements compared to the reflected image in Fig. 2.3(b). We attribute this improvement in image resolution to the lower spherical and chromatic aberrations of the curved mirror system compared to those of

the flat mirror system. Although, this is not an exercise in aberration correction, it does point towards our ability to change the aberration coefficients of our mirror system by manipulating the curvature of the reflection surface. It is conceivable that our imaging scheme combined with an accurately tuned curved mirror could be used in the future to correct the aberrations of the SEM objective lens without the need for a beam separator.

2.3.4 Reflected image resolution and field of view

The discrepancy in image resolution and contrast between the direct and the reflected images is observed to various degrees in all regimes of operation as apparent in all micrographs presented in this work. The poorer resolution and contrast of the reflected image is to be expected considering the added spherical and chromatic aberrations that the uncorrected mirror system imparts onto the reflected beam. In this section, we use micrographs to quantify the beam spot size after reflection, comment on the contrast of the reflected image, and discuss the useful field of view and magnification of the reflected image.

As a measure of the electron probe size after reflection, we obtained the intensity profile of the edge indicated by the dashed line in Fig. 2.4(a). Figure 2.4(b) shows this line profile (solid) along with its first derivative (dashed) after an average filter of window size 3 was applied to the latter for slight smoothening. The full width at half maximum of the derivative indicates a probe diameter of about 100 nm for the reflected beam. This region of the reflected image was chosen for its apparent sharpness and lack of astigmatism compared to the rest of the micrograph. However, factors such as mechanical vibration and the finite sharpness of the edge of the sample make this measurement pessimistic – the true probe size may be slightly smaller than 100 nm. Note that this measurement is not of the direct beam whose diameter, devoid of the aberrations of the mirror system, is considerably smaller.

To compare the resolution of the direct and the reflected images, we imaged samples with relatively fine features. We deposited micrometer-sized tin particles on a TEM copper grid with a thin carbon membrane on top. In certain areas, the carbon membrane ruptured and wrapped around the tin particles. The result, as shown in Fig. 2.4(c), is suspended tin particles wrapped in thin strands of carbon. The blue and red dashed lines represent the line scans whose profiles are shown in Fig. 2.4(d). The width of one of the carbon strands as measured on the line profile on

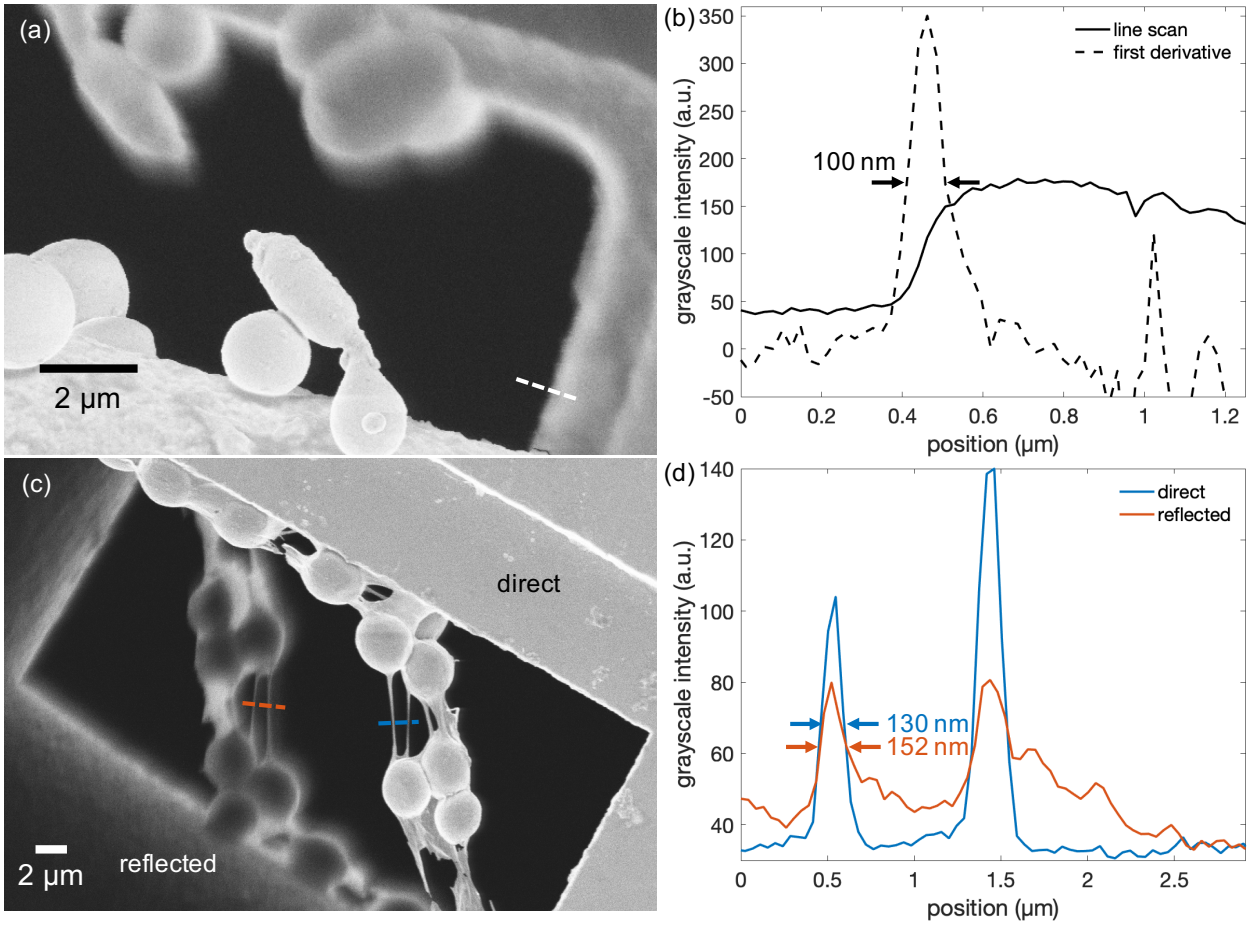

Figure 2.4: Approximating the reflected probe size and resolution of the reflected image. (a) Reflected image of a sharp edge appropriate for a knife-edge measurement. (b) Image intensity at the reflected image of the sample edge (solid) and its derivative (dashed) measured at the line indicated by the dashed line shown in (a). Note that this is not a measure of the direct beam whose diameter is significantly smaller. (c) Simultaneous imaging of top and bottom surfaces of a sample containing fine features. The dashed lines indicate the lines over which image intensity profiles were obtained for the direct (blue) and the reflected (red) images. (d) The width of one of the carbon strands as measured on the direct image (blue) and reflected image (red) is about 130 nm and 152 nm, respectively.

the direct image (blue) is about 130 nm. The same strand measured on the reflected image (red) is about 152 nm wide, which indicates slight beam broadening after reflection. More significantly, however, the reflected image shows a one-sided halo to the right side of the sample as evident from the micrograph in Fig. 2.4(c) and the intensity level of the reflected line profile (red) to the right of each peak in Fig. 2.4(d). This one-sided halo is resulted from a distorted scanning probe which we speculate could be due to a combination of astigmatism imparted onto the reflected beam by a slightly misaligned mirror system and the residual electric field from the mirror system near the grounded sample.

The lower contrast and brightness of the reflected image compared to the direct image, as visually apparent from micrographs as well as from the line scans shown in Fig. 2.4(d), is largely attributed to the lower detection efficiency of secondary electrons that originated from the back-side of the sample. When the in-lens secondary electron detector in our Zeiss SEM is activated, the electric field of the suction tube in the vicinity of the objective lens pole piece accelerates the secondary electrons upward towards the detector placed inside the SEM column. However, in our imaging scheme, the secondary electrons that were generated by the reflected beam on the backside of the sample have to go through a U-turn while the ones from the top surface of the sample have a more direct path to the in-lens detector. The longer, indirect path of the secondary electrons contributing to the reflected image leads to a lower number of them making it to the detector causing the lower brightness and contrast of the reflected image.

The field of view in an SEM image is set by how far from the optical axis the scan coils deflect the incident probe. In our imaging scheme, the area over which the reflected beam scans the bottom side of the sample is coupled to the direct beam scan. However, downstream of the sample, where the beam enters the mirror system, the scan causes the beam to deviate from the optical axis, leading to more aberrations in the reflected probe as a function of scan angle. Consequently, the reflected image has a smaller useful field of view as shown in Fig. 2.5(a). As indicated by the circle in Fig. 2.5(a), the acceptable sharpness in the reflected image is limited to an area of about 120 μm while the direct image is sharp over the entire frame, in this case 560 μm. We observe an improvement in the useful field of view of the reflected image when using a five-electrode aperture mirror system as opposed to the flat tetrode mirror. In this case, as indicated by the dashed circle shown in Fig. 2.5(b), the useful field of view is 200 μm. We attribute this

improvement to partially diminished aberrations of the mirror system achieved by the curved mirror potential surface.

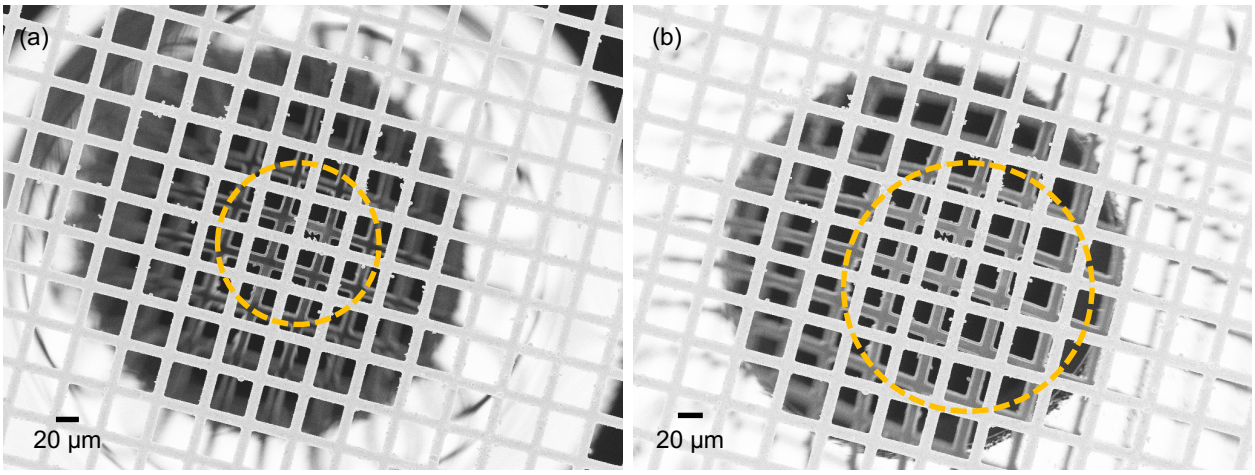

Figure 2.5: Approximating the area over which the reflected image remains sharp, what we define as the reflected image's useful field of view. The brighter grid in the foreground is the direct image and the darker background grid is the reflected image of the bottom side of the sample. Imaging was conducted under the regime where the back-focal plane of the mirror system coincides with the sample plane. (a) Reflection imaging using a tetrode electron mirror setup. The yellow dashed circle points towards a useful field of view of about 120 µm in diameter. (b) Reflection imaging using a five-electrode aperture mirror. The useful field of view as indicated by the yellow dashed circle is approximately 200 µm in diameter.

Another practical limit to the field of view of the reflected image comes from the white halo appearing outside of the central region of the image as shown in Fig. 2.5. What causes this bright halo is the divergent reflected beam striking the bottom of the objective lens pole piece of the SEM after passing through the image plane and generating a large number of secondary electrons which are in turn detected by the in-lens detector. This halo lowers the signal to noise ratio and places a practical limit on the field of view of the reflected image.

The relative magnification of the direct image compared to the reflected image is 1:1 for the first regime of operation where the sample overlaps the back-focal plane of the mirror system in both the tetrode mirror setup and the five-electrode aperture mirror setup (see Fig. 2.5). However, as seen in Fig. 2.6, there is considerable demagnification of the reflected image when the sample overlaps the image plane of the mirror system in the five-electrode aperture mirror setup. In this regime, a focused probe scans the surface of the concave mirror and hence there is a nonlinear relationship between the scan angle of the incident and the reflected beams. This nonlinear rela-

tionship, defined by the curvature of the reflection plane, is generated by the spherical aberration of the aperture mirror. Note that the reflected image of features farther away from the optical axis are more severely demagnified leading to the appearance of barrel distortion in the reflected image. A potential application of this effect could be probing of the curvature of the mirror for diagnostics and characterization of its spherical aberration.

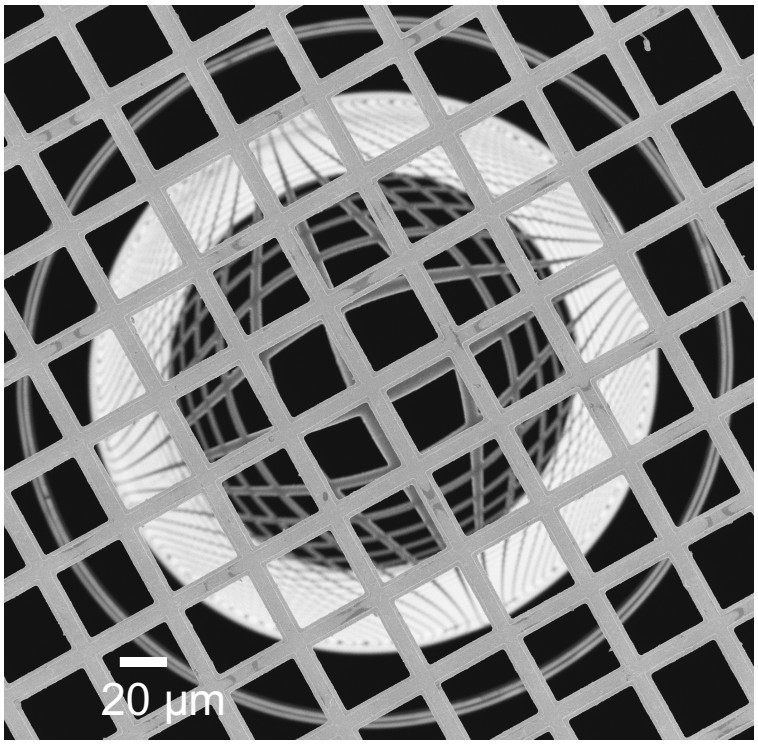

Figure 2.6: Demagnification of the reflected image when using a five-electrode aperture mirror under the regime where the image plane of the mirror system coincides with the sample plane. The foreground shows the direct image and the background shows the reflected image. The reflected image of features farther away from the center are demagnified more severely, leading to appearance of barrel distortion.

2.4 Conclusion and future work

We demonstrated a scheme for simultaneous imaging of top and bottom surfaces of a sample using multi-electrode electron mirrors in an SEM. We believe that this technique could be of value to the in-situ SEM community where simultaneously observing dynamic changes on both sides of a sample may be of interest. We analyzed the image resolution currently attainable in our

setup and identified ways through which this resolution could be improved. Most crucially, by imaging the pivot point of the SEM onto the reflection center, we hope to improve the resolution of the reflected image in areas farther away from the optical axis.

Next, by slightly altering the mirror setup, we demonstrated that the reflected image resolution could be improved when using a five-electrode concave mirror system. We speculate that the smaller aberrations of the curved mirror could be responsible for this improvement. We believe that for the special case of perforated samples, our imaging scheme could allow for "in-line" spherical aberration correction in an SEM without the need for beam separators of any kind. Rigorous analysis as well as fulfillment of the aforementioned design improvements to the experimental setup are necessary for realization of this aberration correction strategy.

In parallel, we have been developing tetrode electron mirrors fabricated using MEMS fabrication techniques. This alternative approach enables the manufacturing of very round lens apertures that eliminate the need for a stigmator to correct for the non-roundness of apertures that is encountered in conventionally machined electrode apertures [57]. Furthermore, the miniaturization of electron mirrors would allow for easier integration in a wider range of commercial SEMs. Finally, due to the smaller electrode aperture and electrode separation of these micromachined mirror systems, it would be possible to maintain similar electric fields as used in this work but with smaller applied voltages. This could open up the possibility of using accelerating lensing as opposed to decelerating lensing which would reduce the spherical aberration for a given focal length.

The potential applications of the imaging scheme reported in this work are not limited only to microscopy; indeed, it is feasible to envision this technique being extended to focused ion-beam milling. Considering that ion beams, much like electron beams, could be reflected and refocused using an electrostatic multi-electrode mirror system, one could incorporate a multi-electrode mirror under the sample in an ion-milling system. By programming the scan, the user could achieve ion milling on the top and bottom surfaces of a sample without the need to flip the sample over. Furthermore, since most focused ion beam tools come equipped with an electron column, one could envision using our mirror imaging technique to monitor the bottom surface of the specimen for signs of damage or redeposition while the sample is being milled on the top surface.

Acknowledgments

This work was supported by Gordon and Betty Moore Foundation and the Natural Sciences and Engineering Research Council of Canada. This research was part of the Quantum Electron Microscopy project and we would like to thank the entire QEM team (MIT, Delft University of technology, Stanford University, and University of Erlangen). We are grateful to our MIT colleagues Marco Turchetti, Akshay Agarwal, Marco Colangelo, Phillip Keathley, Brenden Butters, and Emma Batson for valuable discussions. Finally we would like to acknowledge Ben Caplins and Ryan M. White of NIST for suggesting the FIB application for our imaging scheme.

Chapter 3

Diffractive electron mirror as a loss-less electron beam splitter

The IFM scheme of QEM as designed by Kruit *et al.* [31] is proposed to achieve two superimposed states of an electron by means of electron diffraction. Krielaart and Kruit have theoretically demonstrated that a diffraction grating with a small enough period when biased to a sufficiently large negative voltage is capable of diffracting an incident electron beam and thus behaving as an electron beam splitter [55]. In this thesis, I refer to such a device as a diffractive electron mirror (DEM). Conventional transmission gratings or thin crystals inevitably lead to some inelastic losses since electrons have to pass through matter in order to undergo diffraction. DEMs however, could in theory operate with zero loss since electrons interact only with potential surfaces formed above the physical surface of the grating. The lossless operation of the beam splitter becomes crucial in QEM which would operate at low enough acceleration voltages (3-10 kV) where inelastic losses would be significant even when the beam passes through very thin crystals.

Conversations with Dr. M.A.R Krielaart, Prof. Pieter Kruit, Dr. Rudolf Tromp, and Dr. Akshay Agarwal greatly helped my understanding of the theory involved in this chapter. Dr. Timothy Savas, Marco Colangelo, James Daley, and Mark Mondol provided support and advice throughout the fabrication process. John Simonaitis helped me with many of the experiments performed at MIT. Dr. Tromp conducted all LEEM experiments and simulations based on devices I fabricated at MIT.

3.1 Theory

In this section, I will go over the theory behind the use of DEMs as lossless beam splitters for use in quantum electron microscopy. First I will review the work done by Krielaart and Kruit on the relationship between various DEM parameters and diffraction intensity. Next, I will discuss the importance of electron coherence in my experiments. Finally, I will discuss some of the practical challenges associated with this experiment such as small diffraction angles, and electron energy spread.

3.1.1 Phase shift modulation

Consider the DEM in its simplest form, a corrugated conductive plate biased to the mirror voltage U_{m}, and a field-limiting plate to terminate the field lines in a controlled geometry. The field limiting plate, here referred to as the cap electrode, is usually grounded and contains a small aperture at its center for the passage of electrons. It is worth noting that this hole is small enough to not severely disturb the largely flat and parallel potential surfaces formed between the two plates. Figure 3.1 shows a schematic of such a simple DEM along with various regions labeled according to the type of potential energy the incident electron experiences. Note that the schematic is not drawn to scale; in particular, the quasi-sinusoidal potential surfaces formed near the physical surface of the grating are exaggerated for clarity. Furthermore, other electrodes needed for a functional DEM have been omitted for simplicity.

Region I in Fig. 3.1 is largely field-free as the cap electrode is assumed to block most of the field from leaking outside the mirror region. Passing through the small aperture of the cap electrode and entering region II, the electron experiences a gradual increase in potential energy as depicted with the red linear ramp shown in Fig. 3.1. In this region, the incident electron gradually loses its kinetic energy and begins to slow down. Region III is defined by its proximity to the physical grating where the potential surfaces are quasi-sinusoidal as opposed to flat. The boundary between regions II and III is somewhat arbitrary; however, as the electron penetrates deeper into region III, the amplitude of the sinusoidal potential surfaces increase exponentially and if the incident electron started with sufficient kinetic energy, it could experience the maximum amplitude immediately above the physical surface of the grating. Less energetic electrons

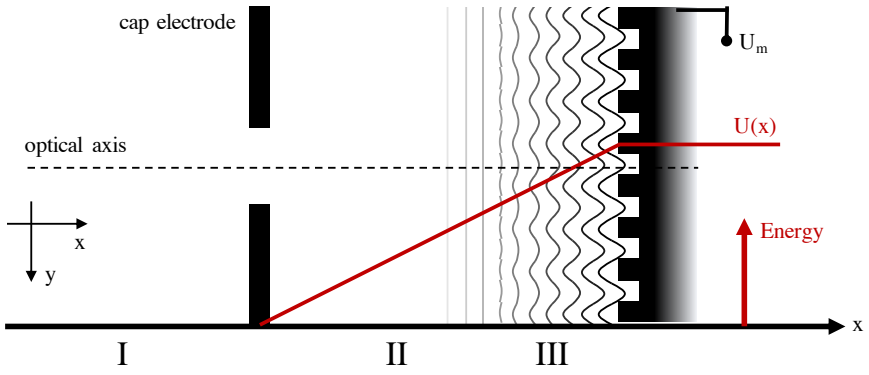

Figure 3.1: Schematic of the simplest form of a diffractive electron mirror (DEM) with various regions marked in accordance to the type of electric potential that the incident electron experiences. The negatively biased diffraction grating produces quasi-sinusoidal potential surfaces which could impart a phase shift modulation onto the electron wavefront, leading to diffraction in far-field.

lose all their kinetic energy before reaching the grating and begin accelerating in the opposite direction — classical turning point. Note that in reality, the extent of region III is much smaller than that of region II due to exponential decay of the amplitude of the sinusoidal equipotential surfaces — the distance between the two electrodes is of the order of 1 mm while region III spans over a few micrometers.

Conventionally, electrons are diffracted by transmission through a thin crystal or a nanofabricated periodic structure such as a phase gratings. This type of diffraction could be thought of as the far-field consequence of a periodic disturbance in the electron wavefront which presents itself as constructive and destructive interferences in the far-field — a diffraction pattern. In the case of a DEM, since the reflection plane is quasi-sinusoidal, the spatially spread out incident electron plane wave undergoes a phase shift modulation upon reflection due to the path length differences within it. The consequent far-field diffraction is the mechanism by which QEM has been proposed to achieve coherent electron beam splitting.

Krielaart and Kruit laid the theoretical ground work for DEMs by calculating the relationship between the mirror voltage and diffraction spot intensities in far-field [55]. To solve for diffraction intensities, they first had to calculate the amount of phase shift each part of the electron wave front undergoes after being reflected by the DEM. Crucially, this phase shift is dependent on the position of the classical turning point along the direction of propagation. For instance, if

the voltage applied to the mirror electrode is considerably more negative than the acceleration voltage, the classical turning point would lie in region II where the reflection planes are largely flat, leading to no significant phase shift modulation being imparted on the electron. However, at a less negative voltage, the classical turning point could be placed in region III where the reflection planes are quasi-sinusoidal. At mirror voltages equal to or smaller than the electron acceleration voltage, the incident electron strikes the physical surface of the grating, leading to inelastic scattering.

Approximating the shape of potential surfaces formed near the grating as sinusoidal, an equation for the potential in between the two electrodes (regions II and III) could be written as:

$$U(x, y) = U_{\mathrm{m}} \left[1 + \frac{1}{d} \left(\delta \sin\left(\frac{2\pi}{p} y \right) \exp\left(\frac{2\pi}{p} x \right) - x \right) \right] \tag{3.1}$$

where U_{m} is the constant potential applied to the grating mirror, d is the distance between the two electrodes, p is the period of the grating and δ is the (maximum) amplitude of the sinusoidal potential surface forming immediately above the physical surface of the grating. The electric potential modulation due to the grating is apparent from the sine term along the y-direction while the exponential decay of the amplitude of the sinusoidal potential surfaces is apparent from the exponential term along the direction of propagation (x). Importantly, Eq. 3.1 entails that for a given distance to the grating along the $-x$-direction, the smaller the grating period, p, the smaller the amplitude of the sinusoidal potential surface would be. In other words, gratings with larger periods tend to maintain a larger amplitude sinusoidal potential surface farther away from the grating surface. By Krielaart's estimation, for a distance $\frac{5}{2\pi} p \ll d$ above the physical surface of the grating, the potential surfaces are practically flat [55].

Having an equation that describe how the potential varies spatially in between the two electrodes, Krielaart and Kruit numerically calculated the phase modulation due to the grating mirror by integrating along various parallel paths along the direction of propagation using two different methods. First, they used the WKB approximation in region II where the potential is linear and slow-varying. Next, due to the limitation of the WKB approximation near classical turning points ($\lambda_{\mathrm{e}} \to \infty$), they numerically solved the Schrodinger's equation in region III. Note that due to the sinusoidal nature of the potential in this region, integration along the direction of propagation

must be carried out for each point along the transverse direction, y. In practice, since the problem is periodic along the y-axis, one could numerically solve for the accumulated phases over one period of the grating to then generalize across the entire grating.

Figure 3.2 borrowed from [55] shows the numerical results that Krielaart and Kruit calculated for electron phase accumulation over one period of the grating. In this case, they chose a grating with a period of 500 nm and an electron acceleration voltage of -2000 V. As expected, the phase accumulation as a function of the transverse direction follows a similar sinusoidal geometry imposed by the potential surfaces. Furthermore, the relationship between phase shift modulation and mirror voltage is apparent: lower mirror voltages lead to more pronounced phase shift modulation after reflection. An intuitive way to think about this relationship is to recall the fact that lower mirror voltages bring the classical turning point closer to the surface of the grating where the amplitudes of the sinusoidal potential surfaces are larger.

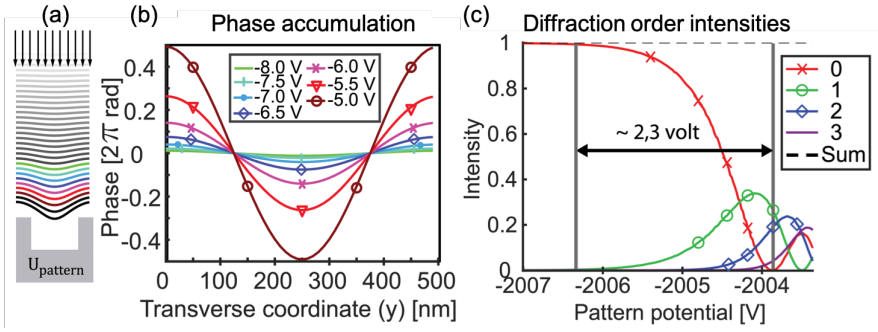

Figure 3.2: Theoretical analysis of the relationship between the mirror voltage and diffraction intensity. (a) Unit cell used in numerical calculations. (b) Phase accumulation for various mirror voltages. In general, lower mirror voltages lead to a more pronounced phase shift modulation. (c) Diffraction order intensity as a function of mirror voltage. Over a span of $\sim$ 2.3 V the intensity in the zeroth order beam diminishes entirely and the intensity is transferred to higher order diffracted beams. Figure taken from [55]. In this thesis, U_{pattern} is referred to as U_{mirror}.

Analogous to the way the thickness of a thin crystal dictates the amount of phase shift imparted onto a beam and consequently the intensity in each diffraction order, the voltage applied the DEM could be used to control the amount of signal in each diffraction order. This effect is apparent in Fig. 3.2(c) where at larger (negative) voltages, almost all the intensity is detected within the central zeroth order beam. As the pattern potential (mirror voltage) is lowered, the incident electron penetrates deeper into the mirror field where larger-amplitude sinusoidal reflection planes impart a more severe phase shift modulation onto the beam, sending more and

more of the total intensity into the higher order diffraction orders. Krielaart notes that by lowering the voltage by only a few volts, one can achieve a fully attenuated zeroth order beam with the intensity transferred to higher order diffraction orders. Note that only the positive diffraction orders have been presented in this plot.

In Chapter 1, it was discussed that an efficient interaction-free measurement (IFM) scheme requires a beam splitter with a relatively high reflectivity to ensure minimal probability of damage to the sample. In the context of the DEM, this requirement means that the user must tune the mirror voltage such that the majority of the intensity remains in the central beam (zeroth order) and only a small fraction of the intensity is transferred to the ±1 orders.

3.1.2 A note on electron coherence and energy spread

Spatial coherence for an electron could be loosely defined as the extent to which there is a fixed phase relation between two spatially separated parts of the electron wave [58]. Naturally, this concept gives rise to the notion of a coherence length, defined as the length over which the beam is fully coherent. Note that electrons are fermions and as such, there can be no coherence between two separate electrons. Any discussion of electron coherence refers to coherence within the same electron wave [58]. The Young's double slit experiment is often resorted to in discussions of spatial coherence length. Consider the classic two-slit experiment with a fully coherent electron beam. In this case, due to constructive and destructive interference, one observes intensity fringes on a screen (photographic film), placed on the other side of the slits. Now consider a beam with limited spatial coherence, say a coherence length of 100 nm. So long as the slits are not separated more than the spatial coherence length, one is able to observe the interference fringes. However, for slits that are farther separated, the visibility of the fringes decreases and eventually no fringes could be recorded. By analogy, in the case of using a DEM as an electron beam splitter, it is crucial for the coherence length of the electron to be longer than the period of the grating.

For a fixed electron source brightness, one can always ensure spatial coherence across the entire beam by reducing the beam current using current-limiting apertures to effectively remove the incoherent components of the beam [58]. However, depending on the experiment, working with such low beam currents may be challenging.

Temporal coherence for an electron could be defined as the extent to which the electron is

coherent along the direction of propagation [58]. A useful experimental setup in discussions of temporal coherence is the Michelson interferometer in which a photon is made to interfere with itself after a delay. If the temporal coherence length is longer than the path length difference associated with that delay, then one would expect to observe an interference pattern form on the screen. In electron microscopy with a continuous-wave electron beam, where it is assumed that the inherent energy spread of the beam is due to incoherent phenomena, the limit on temporal coherence is associated with the inherent energy spread of the electrons emitted from the source. A perfectly monochromatic beam ($\Delta E = 0$) would have a very long temporal coherence length [58]; however, in reality, electron sources have a finite energy spread and therefore a finite temporal coherence length.

Perhaps more pressing than its influence on temporal coherence, the finite energy spread of the beam limits the efficacy of the DEM system as a lossless beam splitter. The extent of the problem becomes more clear when one considers the fact that a spread in electron energy would necessarily mean a spread in the velocity of the electrons. At a given nominal beam acceleration voltage and mirror voltage, set to ensure reflection above the physical surface of the grating mirror, faster electrons would penetrate deeper into the mirror field while slower electrons reflect at a larger distance from the surface of the grating. This spread in height above the grating over which various electrons experience their classical turning point would mean that various electrons obtain different amounts of phase shift upon reflection. Recall that for DEMs with smaller periods, the mirror voltage must be set such that the incident electrons would reflect relatively close to the physical surface of the grating. In this case, a spread in the electron beam energy may mean collision with the grating — inelastic scattering — for faster electrons.

Consider the following example: a DEM with a grating period of 100 nm, nominal electron beam energy of 3 keV with 1 eV of energy spread (common for Schottky sources), and an electric field of 10 kV/mm in between the mirror and cap electrodes. It is the rule of thumb that for sufficient phase shift modulation, the distance between the classical turning point and the physical surface of the grating should be of the same order as the period of the grating. In this case, we can assume a classical turning point lying roughly about 100 nm above the grating. Given the strength of the electric field, an energy spread of 1 eV corresponds to a height spread of 100 nm. In other words, if the slower electrons reflect at a height of 100 nm above the grating, some of

the fastest electrons may strike the grating and be lost to inelastic scattering, liming the extent to which this beam splitter would be lossless.

One way to mitigate the deleterious effects of the electron energy spread is to increase the electric field strength between the mirror and cap electrodes. For a given electron acceleration voltage and energy spread, the extent in the direction of propagation over which electrons are reflected could be minimized if the electric field is increased. For instance, at a mirror voltage of -3000 V and an electron energy spread of 1 eV, the spatial separation of the reflection planes for the fastest and the slowest electrons would be 100 nm and 200 nm for electric fields of 10 kV/mm and 5 kV/mm, respectively. Greater electric fields could be achieved in three ways: (1) increasing the negative voltage applied to the mirror electrode, (2) reducing the distance between the two electrodes, and (3) applying a positive bias to the normally grounded cap electrode. Since the amount of phase shift imparted onto the electrons is coupled to the mirror voltage, the first strategy is not acceptable. Furthermore, reducing the distance between the electrodes may not be convenient as it requires a change in the physical construction of the DEM. Therefore, one is left with applying a positive voltage to the cap electrode. This strategy leads to a greater negative lensing effect at the cap electrode's aperture which could be countered with a larger bias applied to the lens electrode (see Chapter 2). However, fundamentally, one cannot reliably achieve electric fields greater than 10 kV/mm due to electric breakdown (arcing) between various DEM electrodes.

3.1.3 Diffraction angle and practical challenges

To find the angle of diffraction, one can draw an analogy with the multiple-slits experiment in which diffraction angle is approximated based on the electron wavelength and the period of the grating:

$$\theta_{\text{diff}} \approx \lambda_{\text{e}}/p \tag{3.2}$$

where λ_{e} is the de Broglie wavelength of the electron in free-space (region I), and p is the period or pitch of the DEM. With an electron lens (not depicted in Fig. 3.1), one can form a diffraction pattern on the back-focal plane of the lens system. The diffraction spot separation could be approximated as:

$$d_{\text{spot}} \approx \theta_{\text{diff}} f \tag{3.3}$$

where f is the focal length of the lens system. From Eqs. 3.2 and 3.3 one can readily see how for a given electron energy (wavelength), the diffraction spot separation increases as the DEM period decreases. Generally, larger diffraction spot separations are desirable purely for practical reasons — ease of measurement. However, due to various difficulties associated with smaller periods such as the need for the reflection plane to be very close to the physical surface of the grating and risk of inelastic scattering, smaller pitches are not always a viable solution.

3.2 Fabrication

The period of the DEM is one of the factors that dictates the angle of diffraction [59, 55]. Therefore, depending on the experimental design requirements, I fabricated DEMs using two different fabrication methods: (1) optical interference lithography for periods of 300-500 nm, and (2) electron-beam lithography for periods of 40-200 nm. Here, I briefly describe the steps involved in each method.

3.2.1 Optical interference lithography (Lloyd's mirror)

In optical interference lithography, a photosensitive resist film is exposed by a periodic light pattern created by constructive and destructive interferences. The Lloyd's mirror setup is a simplified approach to optical interference lithography whereby a carefully positioned flat mirror reflects part of the spread-out wavefront from a monochromatic laser onto the direct wavefront, creating optical interference. The periodicity of the pattern depends on the angle of illumination and the wavelength of the laser [60]. This dependence on the wavelength places a lower-bound on how small a period can be fabricated using this technique. Nonetheless, the advantage of this approach over higher resolution fabrication methods such as electron-beam lithography, is throughput. Areas as large as several centimeters in diameter could be exposed and patterns in a matter of minutes as opposed to several hours or even days.

Figure 3.3 shows an overview of the fabrication process while a more detailed account of

the fabrication process could be found in Chapter 4 of my Master's Thesis [59]. It is however worth noting that heavily doped silicon wafers, 25 mm in diameter, were chosen as the substrate due to their size and smooth, polished edges (sharp edges of cleaved chips may lead to electrical breakdown in large electric fields). Gratings with periods ranging from 300 nm to 500 nm were fabricated in this work. Figure 3.4(a) shows a cross section SEM micrograph of a silicon grating with a 300 nm period. Figure 3.4(b) shows a silicon wafer mounted on the mirror electrode using silver paint after the fabrication process. The mirror electrode is then assembled in a tetrode mirror stack using precision ceramic balls for mechanical stability and electrical insulation as was discussed in Chapter 2. The advantage of the large grating area made possible by this fabrication process becomes apparent when it comes to the alignment effort. Namely, since the entire surface of the silicon wafer is patterned, there is no need for precision alignment between the grating and the aperture hole of the cap electrode.

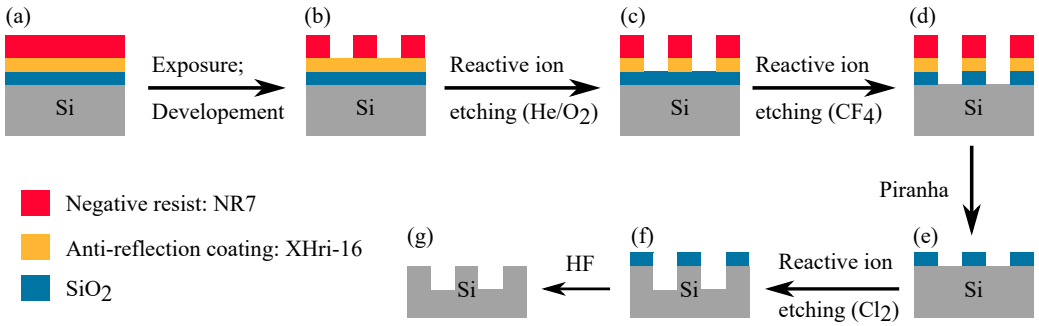

Figure 3.3: Diffraction grating fabrication at a glance. Optical interference lithography (Lloyd's mirror setup) followed by reactive ion etching was used to fabricate one-dimensional diffraction gratings on a 25 mm diameter silicon wafer. Process developed by Timothy Savas.

3.2.2 Electron-beam lithography

In electron beam lithography (EBL), a rastering electron beam exposes an electron-sensitive resist sequentially to write the desired pattern. Figure 3.5 shows an overview of the fabrication process I used in order to fabricate smaller-period DEMs. The advantage of EBL over optical lithography is the ability to pattern considerably smaller features for the fundamental reason that the de Broglie wavelength of electrons is much smaller than that of photons at typical energies. The downside of EBL, however, is that large-area patterning is slow and limited. For instance, in our EBL tool

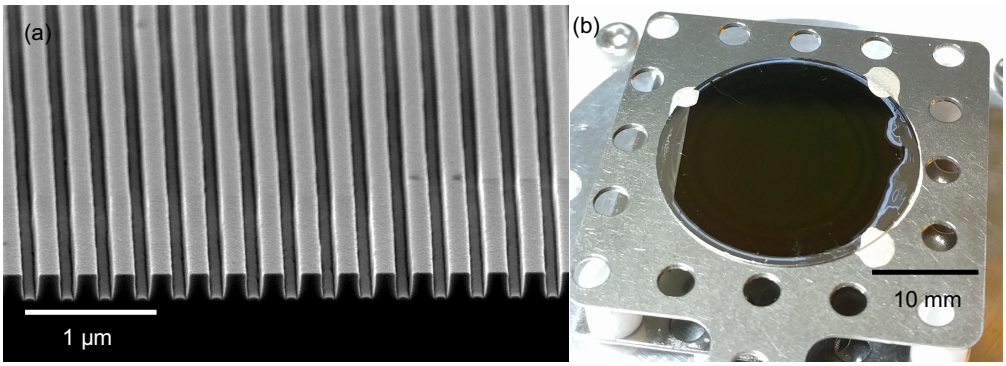

Figure 3.4: (a) SEM micrograph of a silicon diffraction grating with a period of 300 nm fabricated through optical interference lithography (Lloyd's mirror setup). (b) Photograph of the 25 mm diameter silicon wafer after the fabrication process, mounted on the mirror electrode using silver paint.

(Elionix ELSF125) the writing field is limited to an area of 500 μm × 500 μm; larger writes would involve the stitching of two fields together which may cause discontinuity between the fields.

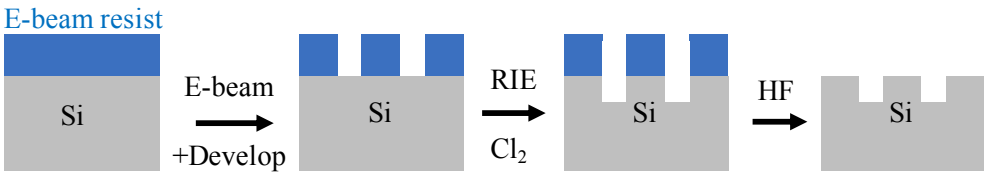

Figure 3.5: Diffraction grating fabrication at a glance. Electron-beam lithography followed by reactive ion etching was used to fabricate one-dimensional diffraction gratings.

The resist used to fabricate these DEMs was 2% HSQ spun at 4000 rpm to achieve a thickness of 32 nm (measured using a reflectometer). The appropriate electron dose for each period was established by writing dose matrices. The patterned chip was developed in salty developer: a solution of 1% NaOH and 4% NaCl by weight in 1 L of DI water. Next, reactive ion etching (RIE) with chlorine gas was used to etch through the silicon while the developed HSQ acted as a mask against chlorine. The RIE power, gas pressure and etch time were found by trial and error. Finally, the residual HSQ was removed by dipping the chip in HF for about 1 minute.

Figure 3.6 shows cross section micrographs of two diffraction gratings with periods of 40 nm and 80 nm. It is apparent that the grating with the smaller period suffers from a more severe line-edge roughness. Indeed, it is a general tendency in EBL for line-edge roughness to become an appreciable percentage of the feature size as the features shrink. This phenomenon is in part

due to the finite diameter of the electron beam. However, other factors such as electromagnetic interference and mechanical vibration during the write, as well as harsh RIE chemistry can play a significant role. Line-edge roughness could lower the efficiency of the DEM as a beam splitter by introducing high-frequency noise components to the otherwise smooth sinusoidal potential surfaces forming above the grating.

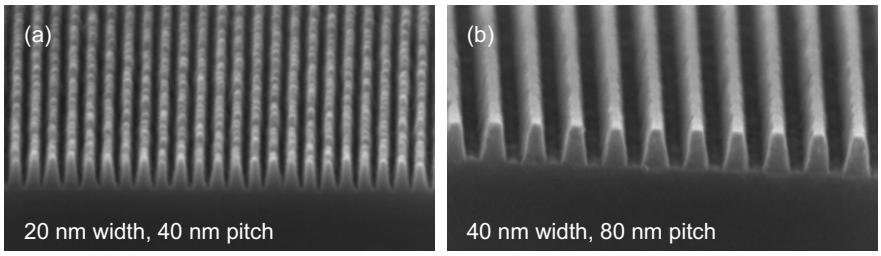

Figure 3.6: Diffraction gratings fabricated on silicon chips. (a) 20 nm wide lines, 40 nm period. (b) 40 nm wide lines, 80 nm period. At smaller periods, line-edge roughness becomes significant which could lower the efficiency of the DEM as a beam splitter.

3.3 Attempts at demonstrating electron diffraction using a DEM

Early in the course of this project, I tested the fabricated gratings in an experimental setup constructed in our own SEM at MIT. Later on, the need for smaller-period gratings necessitated that we test the samples in a more precise instrument. Towards that end, I began a collaboration with Dr. Rudolf Tromp who operates a low-energy electron microscope (LEEM) at his IBM facility. The results from the SEM experiments, although appearing to point towards coherent diffraction, could not be confidently deemed as such. Later, coherent diffraction was ruled out as a phenomenon leading to the results of the LEEM experiments as well. In this section, I discuss the results and analysis associated with either approach and provide hypotheses as to why we were unable to demonstrate electron diffraction using my fabricated DEMs in either experimental setup.

3.3.1 DEM experiments in a scanning electron microscope

In Chapter 2, it was demonstrated that a flat tetrode electron mirror could be installed in an SEM in order to image the backside of a sample when the mirror reflects and refocuses the incident beam onto the sample plane. Now consider the flat mirror electrode being replaced by a diffraction grating of the kind fabricated using optical interference lithography as introduced above. In this case, the incident electron beam would diffract before being reflected and refocused on the back-focal plane of the DEM system where the sample lies. Since the incident beam is scanning, the zeroth order reflected beam along with higher order diffracted beams are expected to scan the bottom side of the sample, producing multiple scanned images of it within the same frame. For this result to constitute as a demonstration of coherent electron diffraction, three criteria must be met: (1) the separation between the reflected images must correspond to the expected diffraction spots separation; (2) the direction in which the repeated images appear must be orthogonal to the lines of the diffraction grating; (3) the voltage applied to the grating must control the amount of signal in various diffraction orders as shown by the theory [55]. In this section, I present the experimental results obtained while testing the DEM in our SEM and discuss why the current results, although resembling electron diffraction, do not necessarily constitute as strong evidence for diffraction.

The DEM system was installed in our SEM in a similar setup as shown in Fig. 2.2 from Chapter 2 and operated under the regime whereby the incident scanning beam is focused on the sample plane on its way towards the tetrode mirror. The tetrode mirror voltages were set such that the back-focal plane coincided with the sample plane. Under this regime of operation, the beam is expected to be nearly collimated at the plane of reflection. Ideally, by imaging the pivot point of the SEM scan coils onto the surface of the reflection plane, one would ensure that the collimated beam is stationary near the optical axis on the reflection plane; however, as was discussed in Chapter 2, I failed to achieve this requirement due to practical limitations of our SEM. As a result, the collimated beam moved along the surface of the mirror in the transverse direction as the incident beam was scanned, leading to potential exacerbation of spherical and chromatic aberrations.

Conveniently, at large enough mirror voltages, due to the flattening of the quasi-sinusoidal

potential surfaces, the DEM system behaves like a simple flat tetrode electron mirror. I used this fact for initial alignment of the sample, electron beam and the mirror system by forming simultaneous images of the sample (right) and the reflection of its backside (left) as shown in Figure 3.7 (a). This sample originally started as a thin carbon film suspended on a TEM copper grid atop whom micrometer-sized tin particles were deposited. However, in certain areas, the carbon film ruptured and wrapped around the tin particles. The thin carbon strands made for a useful sample with relatively small features. In this case, the nominal beam acceleration voltage was -3 kV. The voltages applied to the four electrodes of the DEM system were $V_{\mathrm{m}} = -3050$ V, $V_{\mathrm{c}} = 0$ V, $V_{\mathrm{L}} = -3809$ V, and $V_{\mathrm{g}} = 0$ V for the mirror, cap, lens and ground electrodes respectively. When the mirror voltage was lowered to $V_{\mathrm{m}} = -3018$ V in order to allow the incident electron beam to interact with the grating potential, a faint side-image appeared on the right side of the original reflected image and partially covered by it as shown in Fig. 3.7 (b).

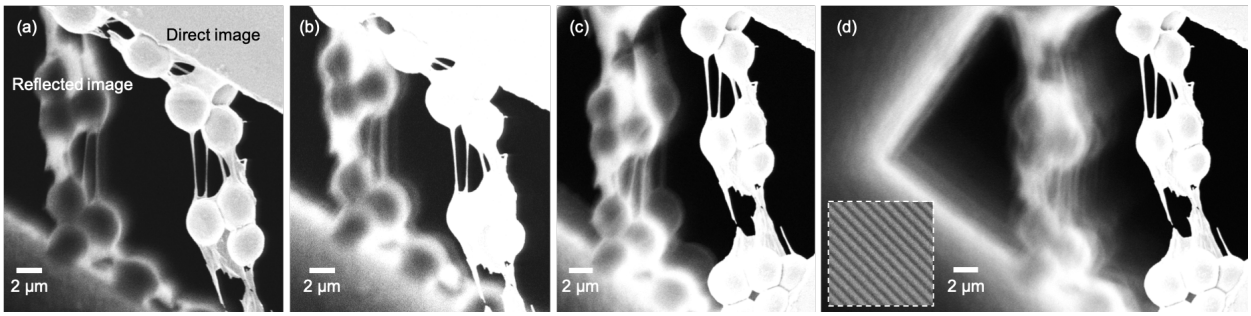

Figure 3.7: Testing the 500 nm period diffractive electron mirror (DEM) in an SEM. (a) At a high enough mirror voltage, the DEM system behaves like a flat tetrode electron mirror: $V_{\mathrm{m}} = -3050$ V, $V_{\mathrm{c}} = 0$ V, $V_{\mathrm{L}} = -3809$ V. (b) Lowering the mirror voltage and tuning the lens voltage leads to appearance of a faint side-image: $V_{\mathrm{m}} = -3018$ V, $V_{\mathrm{c}} = 0$ V, $V_{\mathrm{L}} = -3800$ V. (c) Increasing the electric field strength between the mirror and cap electrodes leads to a prominent side-image: $V_{\mathrm{m}} = -3026$ V, $V_{\mathrm{c}} = +2000$ V, $V_{\mathrm{L}} = -4047$ V. (d) Multiple partially overlapping repeated images appear next to the reflected image: $V_{\mathrm{m}} = -3019$ V, $V_{\mathrm{c}} = +2000$ V, $V_{\mathrm{L}} = -4041$ V. The inset in (d) shows the orientation of the diffraction grating. In micrographs (b)-(d) the image brightness and contrast were increased by 20% and 10% respectively for more visibility.

Note that the transition from a single reflected image to repeated, spatially separated, reflected images shown in Fig. 3.7 (a)-(b) is not achieved only by lowering the mirror voltage. In practice, in order to maintain a sharp image of the backside of the sample, I had to change the lens voltage of the tetrode mirror system after changing the mirror voltage. This requirement is due to the fact that a change to the voltage applied to one electrode has consequences to the rest of the electron

optics in the system. For instance, a change in the mirror voltage leads to a change in the electric field between the mirror and cap electrodes which in turn alters the negative lensing strength of the cap electrode. This change in the cap electrode's lensing effect must be accompanied by a change in the voltage applied to the lens electrode in order to maintain a sharp reflected image.

As was discussed in Section 3.1.2, higher electric fields in between the mirror and cap electrodes is generally desirable. Towards that end, the same experiment was repeated with a positive bias of $V_c = +2000$ V applied to the cap electrode. The results are shown in Fig. 3.7 (c)-(d). Under this regime, a prominently distinct repeated image is visible to the right side of the reflected image even at a mirror voltage of $V_m = -3026$ V as shown in Fig. 3.7 (c). Lowering the mirror voltage to $V_m = -3019$ V, multiple, partially overlapping, repeated images appear on the right side of the original reflected image as shown in Fig. 3.7 (d). It is noteworthy that normally diffraction occurs with positive and negative orders on either sides of the central zeroth order beam. However, as apparent in the results shown in Fig. 3.7, the repeated images do not populate both sides of the original reflected image. The one-sided nature of these repeated images are currently not satisfactorily explained and raise doubt as to whether coherent diffraction is indeed the phenomenon behind these observations.

The inset in Fig. 3.7 (d) shows the orientation of the diffraction grating during the above experiments. It is apparent that the direction in which the repeated images appear is orthogonal to the lines of the grating as one would expect. The slight deviation from the expected direction may be the consequence of external and internal stray magnetic fields rotating the reflected images. The additional rotation of the reflected images compared to the direct image is due to the fact that the electrons that contribute to the reflected images go through an additional round trip trajectory below the sample and as such, they are more susceptible to stray magnetic fields.

Due to the fact that the sample width is larger than image separation in results shown in Fig. 3.7, measurements of image separation and rotation are not very convenient. As such, we[1] fabricated a thin suspended platinum cantilever on a copper TEM grid using focused-ion beam (FIB) deposition. Figure 3.8 shows a micrograph of this sample.

A series of similar DEM experiments were conducted using this new sample in our SEM. Figure 3.9 shows the results of an experiment in which all parameters were kept constant and only

[1]FIB fabrication was done with the help of Dr. Akshay Agarwal

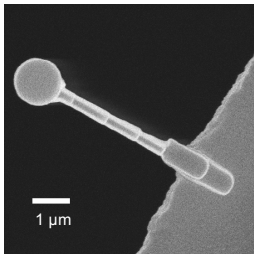

Figure 3.8: A suspended platinum cantilever fabricated using focused ion beam deposition. The narrow nature of this sample allows for easier measurement of image separation and rotation. Fabricated was done with help from Dr. Akshay Agarwal.

the mirror voltage was varied. Note that the direct images of the sample are not included in these micrographs (cropped out) and in all cases, the top, bright reflected image is the primary reflected image. It is apparent that as the negative bias applied to the mirror electrode is increased from −3019 V to −3026 V, the distinct side-images appearing below the primary reflected image fade away and blend together. A simple line scan analysis shown in Fig. 3.9 (e) conducted by averaging over several lines crossing the repeated images in the vicinity of the dashed lines shown in Figs. 3.9 (a)-(d) confirms that the side-images cease to be distinct at higher mirror voltages. Crucially, the signal in these side-images do not simply transition to the main reflected image but rather the signal redistributes spatially over the same area to form a blur. This observation does not fit neatly in the diffraction picture. Note that at higher mirror voltages, it is possible to remove the blur by aligning the SEM aperture and stigmation, as well as tuning the lens voltage; however, the purpose of this experiment was to maintain the variables that led to multiple reflected images throughout testing.

The next criterion in the way of determining whether or not the observations in the DEM experiments constitute coherent diffraction is diffraction spot separation. Theoretically, as determined by Eqs. 3.2 and 3.3, for an incident electron energy of 3 keV, grating period of 500 nm, and a grating-to-sample distance of $\sim$ 13 mm, one would expect a diffraction spot separation of $\sim$ 580 nm. However, measuring the image separation in the micrograph shown in Fig. 3.9 (a) shows a considerably larger separation of $\sim$ 1.5 µm. Moreover, throughout my DEM experiments, I made the observation that the voltages applied to the DEM electrodes have an influence on the separation between the reflected images. An example of this effect could be seen in Fig 3.7 where the side-image in 3.7 (c) is notably farther away to the right of the main reflected image when

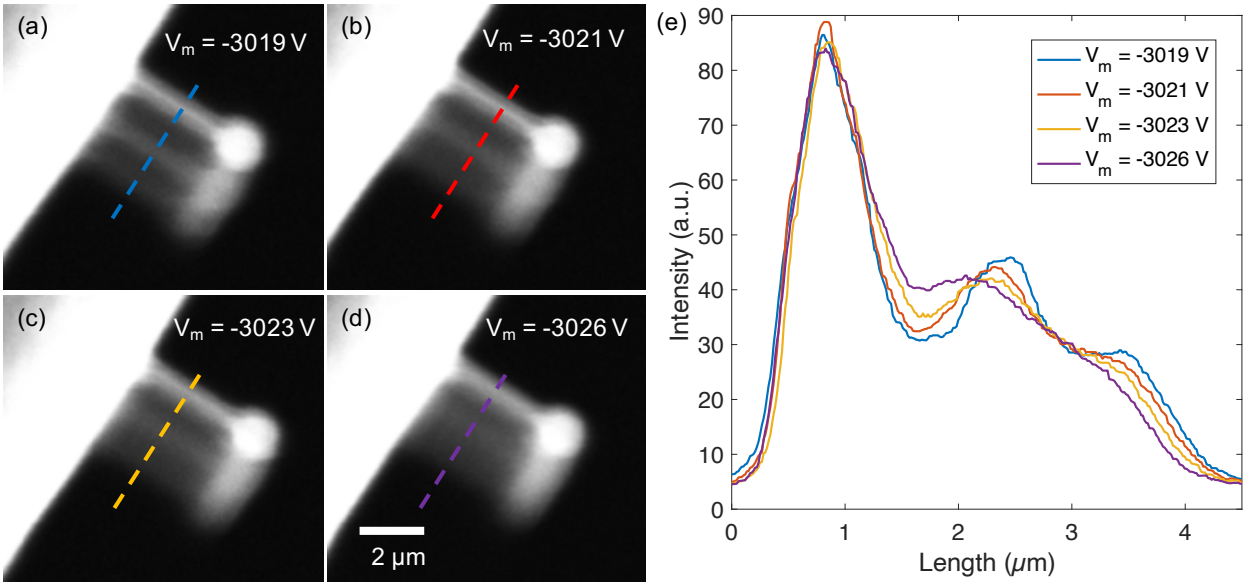

Figure 3.9: Effects of mirror voltage on side-images. All voltages applied to the DEM system except for the mirror voltage were kept constant. As the magnitude of the mirror voltage increases, the side-image blend together to form a blur. SEM beam settings were kept constant. (e) Line scan analysis performed by averaging over several lines parallel to and in the vicinity of the dashed lines. For better visibility, image brightness and contrast were increased by 45% and 10% respectively.

compared to the side-image in 3.7 (b). Currently, the best explanation for this observation is a potential deviation from the ideal imaging regime in which the incident beam should be nearly collimated over the reflection surface. Failure to image in this regime would mean that the tetrode lens voltages change the angle of illumination near the mirror and hence the effective period of the grating as well as the placement of the back-focal plane along the direction of propagation.

The influence of SEM aperture alignment on the results of DEM experiments are also noteworthy. In general, current-limiting apertures are used in most SEMs in order to control the beam current as well as the convergence angle of the beam. Dedicated coils are implemented in order to control the angle and the placement of the beam as it passes through the aperture. In conventional SEM imaging, one must align the aperture[2] such that slight changes to the lensing power of the SEM objective lens leads to minimal image shift. In the context of my DEM experiments, I took advantage of the SEM's aperture alignment coils in order to control the angle with which the incident beam enters the tetrode system and interacts with the grating. Figure 3.10 shows

[2]In our SEM (Zeiss LEO 1525), electrostatic deflectors are used to align the beam to the stationary aperture.

how changes to the aperture alignment coils leads to a modulation of intensity in the side images. Interestingly, this observation is what one would expect from changes applied to the mirror voltage (as theoretically shown by Krielaart and Kruit in [55]). Note that upon disappearance of a side image, the intensity that used to reside in that side-image appears to be transferred to the remaining reflected images. A convincing explanation for this observation is yet to be developed.

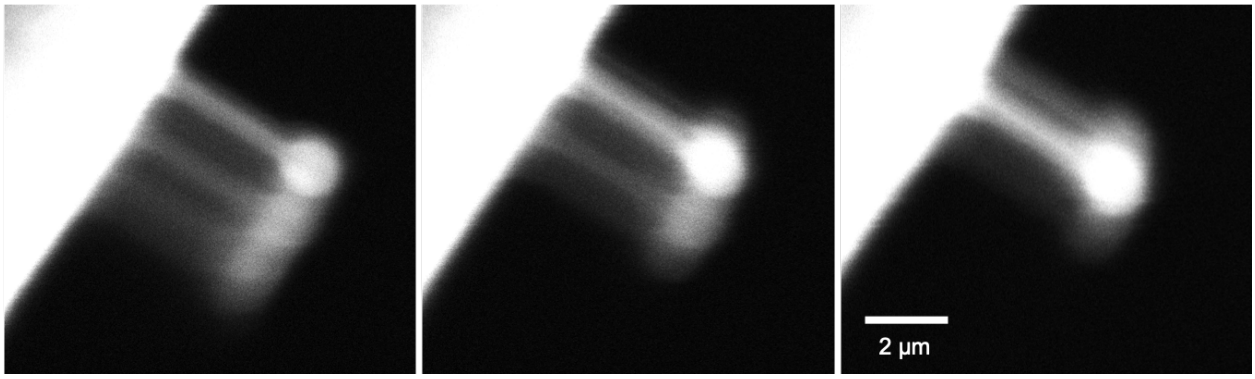

Figure 3.10: Intensity modulation effects of the SEM aperture alignment. Voltages applied to the DEM electrodes were kept constant while only the SEM alignment was varied. For better visibility, image brightness and contrast were increased by 45% and 10% respectively. $V_{\mathrm{m}} = -3019$ V, $V_{\mathrm{c}} = +4000$ V, $V_{\mathrm{L}} = -4450$ V.

Another important detail of this experiment is that although the nominal electron energy was 3 keV, at mirror voltages smaller than ~ -3017 V, the reflected image tended to disappear as the incident electrons struck the physical surface of the mirror and were lost to inelastic scattering. Ideally, one would expect this transition to occur at -3000 ± 1 V. The most likely hypothesis for this voltage discrepancy is the use of separate ground references for the the SEM electron gun and the voltage supply used to bias the DEM electrodes.

Although a retroactive observation of the DEM experiment whose results are shown in Fig. 3.7 showed that the repeated images appear in the direction orthogonal to the lines of the grating, a dedicated experiment was later designed and conducted. In this new experiment, as shown in Fig. 3.11, a 45° rotation of the DEM system led to a corresponding rotation in the direction in which the repeated reflected images appeared. Note that for consistency, the tetrode mirror system was not disassembled in between the two experiments. Instead, the entire mirror stack along with the diffraction grating was rotated.

As a general comment on reproducibility of the results presented in this section, it must be

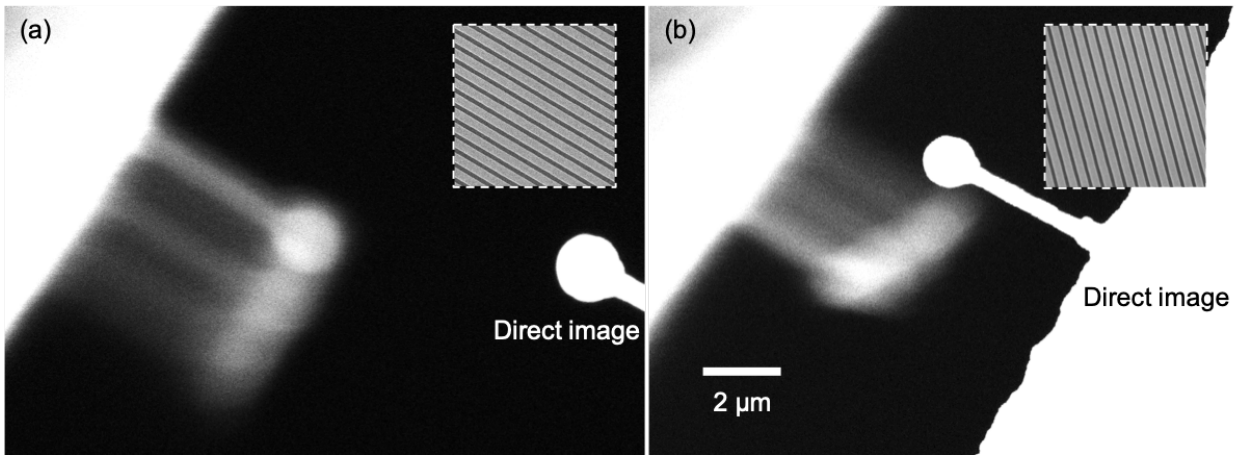

Figure 3.11: Effects of diffraction grating orientation on the direction in which repeated images appear. The insets show the orientation of the diffraction grating during each experiment. (a) $V_m = -3019$ V, $V_c = +4000$ V, $V_L = -4450$ V. (b) $V_m = -3019$ V, $V_c = +2000$ V, $V_L = -4211$ V.

noted that the reliance on certain factors such as deliberate introduction of misalignment in SEM's aperture and stigmation settings makes the process somewhat difficult and arbitrary at times. Simply put, a certain amount of "art" may have to be mixed in with the science. But microscopists are already aware of this necessity!

3.3.2 DEM experiments in a low-energy electron microscope

Apropos of the results of the DEM experiments conducted in the SEM not conclusively pointing towards coherent electron diffraction, a series of parallel experiments were designed to be conducted in a low-energy electron microscope (LEEM) at Dr. Rudolf Tromp's laboratory at IBM. This decision was made since LEEM was developed with imaging of the reflected beam in mind which made it a well-suited instrument for the testing of our DEMs. Furthermore, LEEM is a tool capable of *imaging* in the true sense of the word while an SEM produces images by scanning a focused beam over a sample. This scanning is detrimental to DEM experiments where a beam deviating away from the optical axis while scanning could experience a higher degree of spherical aberration. Moreover, the LEEM at the IBM facility is equipped with a cold field emission source with an energy spread of ~ 220 meV which would allow for the use of diffraction gratings with smaller periods at a lower risk of inelastic scattering (see discussion in Section 3.1.2). All LEEM experiments presented in this section were conducted by Dr. Tromp using the diffraction

gratings that I fabricated at MIT.

Originally, LEEM was developed as a highly surface-sensitive imaging tool in which a sample was biased to a potential close to the equivalent beam acceleration voltage. Figure 3.12 shows a simplified schematic of a LEEM system. The incident beam produced by the electron gun would experience a 90° bend as it passes through a magnetic prism before it interacts with the negatively biased sample. If the sample potential is slightly more negative than the beam acceleration voltage, the LEEM would operate under the mirror regime: the electrons lose all their kinetic energy near the surface of the sample before accelerating in the opposite direction towards the prism and then imaged using the projection optics. At sample potentials slightly less negative than the beam acceleration voltage, the electrons penetrate the sample before losing all their kinetic energy and back-scattering out of the sample to be imaged. Usually, the landing energy of the incident electrons under this regime does not exceed ~ 100 eV to ensure surface sensitivity.

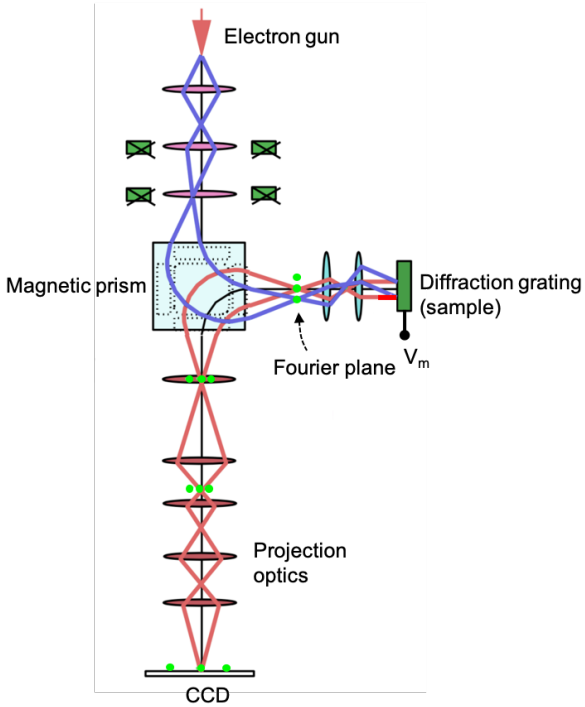

Figure 3.12: Schematic of the low-energy electron microscope (LEEM). Diffraction spots (green dots) appearing on the mirror system's Fourier plane could be imaged onto a CCD using the projection optics. Figure borrowed from [61] and slightly modified.

The design of the DEM experiment in the LEEM system was as follows. As shown in Fig. 3.12 a fabricated silicon diffraction grating was mounted on the sample holder of the LEEM system. The

bias applied to the grating was the independent variable. In the mirror mode ($|V_{\mathrm{m}}| > |V_{\mathrm{gun}}|$), it was expected that the beam would interact with the quasi-sinusoidal potentials near the grating, experience diffraction before being reflected and focused on the back-focal plane (Fourier plane) of the objective lens. With the projection optics tuned to image the Fourier plane, the distinct diffraction spots would be imaged onto a CCD.

For consistency with the earlier SEM experiments, the first sample used in the LEEM system was a silicon diffraction grating with a period of 500 nm and a height of 250 nm. Figure 3.13 shows a series of images of the Fourier plane as the mirror voltage was changed from −3 V to +3 V relative to the beam acceleration voltage of −15 kV. For simplicity, I refer to the relative voltage between the mirror and the gun as the mirror voltage in this section. Note that as shown in Fig. 3.13 (a), at $V_{\mathrm{m}} = -3$ V, a slight beam spread is observed in the horizontal direction while an even smaller spread could be seen along the vertical direction. The former is associated with the chromatic spread of the beam as it passes through the magnetic prism which would inevitably impart different radii of curvature onto electrons of different energies. The latter is associated with beam astigmatism. Unfortunately in this initial experiment, diffraction is also expected to occur along the horizontal direction, making it difficult to distinguish between the effects of energy spread and diffraction.

As the relative voltage is increased to $V_{\mathrm{m}} = 0$ V, the beam profile further lengthens in the horizontal direction as seen in the first row of Fourier plane images shown in Fig. 3.13. Although this spread is due to the nonuniform potential in the vicinity of the diffraction grating, no diffraction spots are observed. When the mirror voltage is increased even further into the positive relative voltages, the system switches from mirror mode to LEEM mode where electrons gently land on the sample before being back-scattered. The appearance of the Ewald sphere is the prominent feature of Fourier plane images in this mode with the sphere size increasing as the landing energy of electrons increases, as seen in Figs. 3.13 (e)-(h). Also notable is the highly nonuniform intensity distribution within the Ewald sphere. This observation is attributed to the fact that as the ultra-low-energy electrons (< 3 eV) emerge out of the physical surface of the grating, they are greatly influenced by the highly non-uniform electric fields in the vicinity of the biased diffraction grating.

After a 90° rotation of the diffraction grating in order to decouple the effects of beam energy

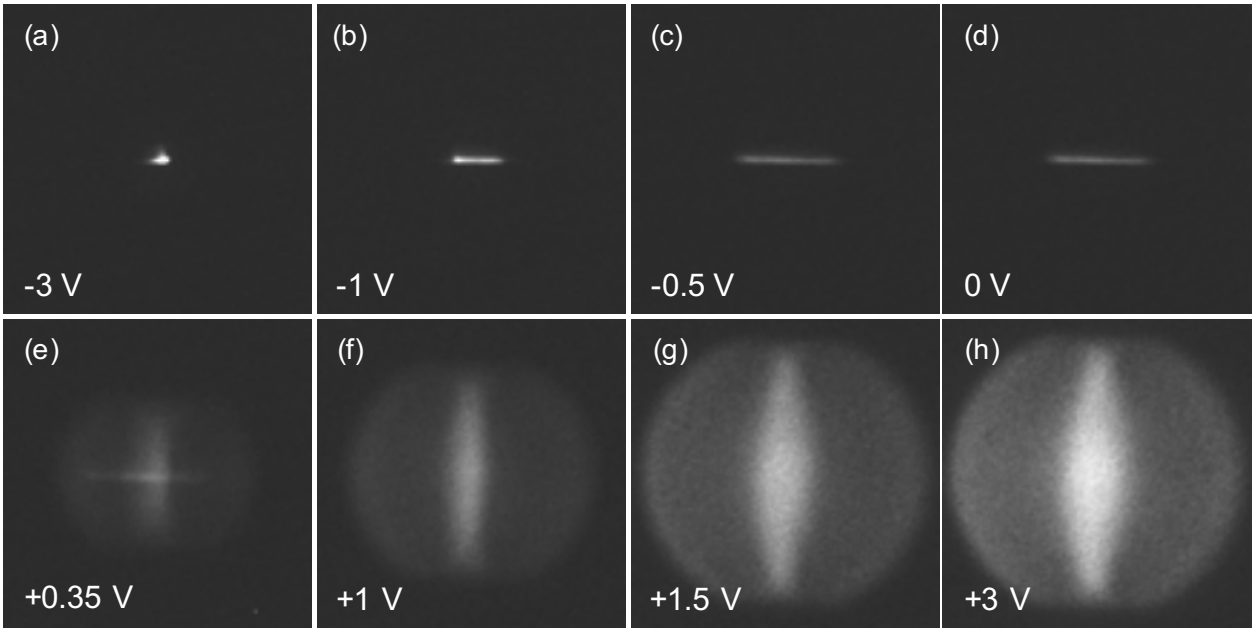

Figure 3.13: LEEM Fourier plane images for different relative mirror voltages (electron landing energies). (a)-(d) Mirror mode with electrons reflecting above the physical surface of the mirror. Lengthening of the beam profile in this mode is attributed to the non-uniform electric field in the vicinity of the biased grating. (e)-(h) LEEM mode with electrons penetrating the sample. Ewald sphere size increases as the electron landing energy increases.

spread and any potential diffraction effects, a similar set of experiments were conducted. Figure 3.14 (a) shows an image of the Fourier plane at a mirror voltage of $V_{\mathrm{m}} = -1$ V. Considering that the electric field at the mirror region is $10\frac{\mathrm{kV}}{\mathrm{mm}}$, at this mirror voltage, the electrons get within $\sim$ 100 nm of the grating surface. However, it is important to note that the beam is not monochromatic. The inherent 220 mV energy spread of the beam entails a height spread of 22 nm. In other words, by assuming a symmetrical energy distribution around the nominal beam energy (not necessarily true), the height of the reflection plane above the surface of the diffraction grating could be calculated to be 100 ± 11 nm. The effect of beam energy spread is apparent in the spatial spread of the beam along the horizontal direction in Fig. 3.14 (a). The contributions of slower and faster electrons appear on the left and right sides of the image respectively.

The beam spread along the vertical direction in the Fourier plane image shown in Fig. 3.14 (a) is due to the nonuniform potential surfaces formed near the grating surface. This spread is more pronounced for faster electrons (right) as they penetrate deeper into the mirror field and are more influenced by the grating field. Note that there is a splitting of the signal along the vertical

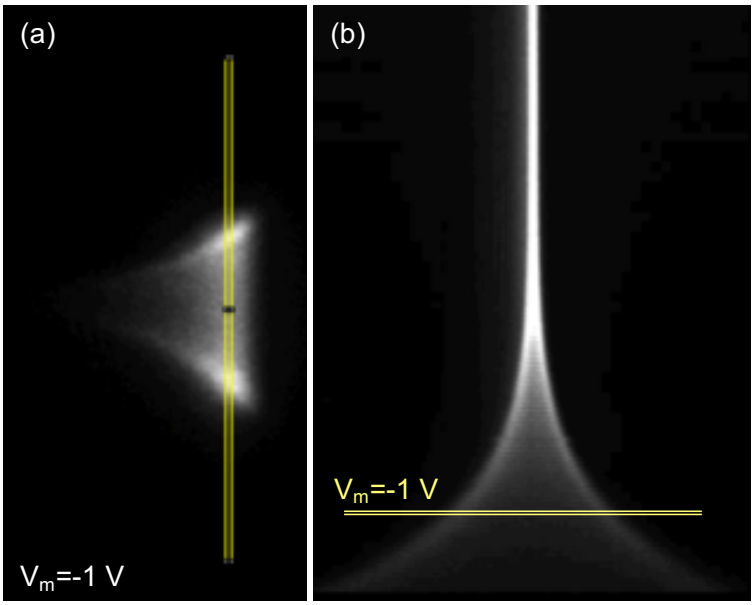

Figure 3.14: Fourier plane image at relative mirror voltage of $V_m = -1$ V (a), and composite energy scan image for mirror voltage range of −6 V (top) to 0 V (bottom) at intervals of 50 mV (b). Each horizontal line in the composite energy scan image comes from a vertical slice of a Fourier plane image as shown by the example of the $V_m = -1$ V. line scan.

direction with concentrated intensity near the top and bottom of the beam. This splitting is a consequence of the focusing power of the trough (concave) regions of the sinusoidal potential surfaces which will be discussed in more detail shortly.

After repeating the above experiment for a mirror potential range of $-6\text{ V} \leq V_m \leq 0\text{ V}$, with a step size of 50 mV, a composite energy scan image was created by taking a vertical slices from each Fourier plane image and placing it horizontally in a stack as shown in Fig. 3.14 (b). In this composite image, the vertical axis corresponds to electron landing energy while the horizontal axis is a spatial direction showing the spread of the beam at the Fourier plane. The yellow vertical slice shown in the Fourier image corresponds to the horizontal yellow slice in the composite image, showing the amount of beam spread at the nominal mirror voltage of $V_m = -1$ V. As expected, near the top of this composite image ($V_m = -6$ V), the beam experiences minimal spreading whereas near the bottom ($V_m = 0$ V), the beam is highly spread out.

The splitting of intensity shown towards the bottom of the composite image shown in Fig. 3.14 (b) may appear to be the result of electron diffraction; however, upon further analysis, it was made clear that another electron optical phenomenon known as caustics could lead to these

observations. Intensity splitting due to caustics may not be relied upon for the application of interest which is lossless electron beam splitters for use in QEM since caustics is not a coherent phenomenon. In fact, no phase effects are involved — pure ray optics (treating electrons as particles) could explain the above observation. Ray tracing simulations (Charged Particle Optics) performed by Dr. Tromp have captured this intensity splitting effect. Figure 3.15 juxtaposes experimental (left) and simulation (right) results for mirror voltages in the range of $-6\ \mathrm{V} \leq V_\mathrm{m} \leq 0\ \mathrm{V}$. Note that for clarity, the intensity in each line of the composite image has been normalized separately. The simulation results show concentrated signal intensity along the outer parameters of the beam. Moreover, the dependence of beam spread on mirror voltage is captured in the simulation results. Note that the experiment was performed at energy steps of 50 meV while the simulations were done for energy steps of 200 meV which explains the discrepancy in the smoothness of the composite images.

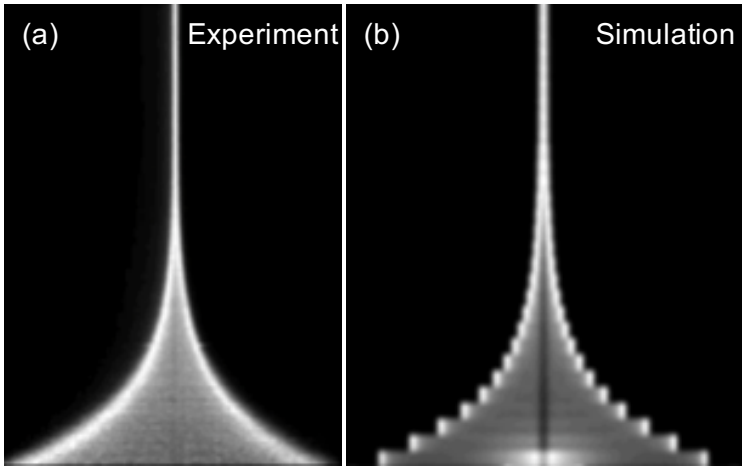

Figure 3.15: Composite energy scan images: (a) LEEM experiment, (b) Classical ray tracing simulation. Mirror voltage range: $-6\ \mathrm{V} \leq V_\mathrm{m} \leq 0\ \mathrm{V}$. Voltage step size: (a) 50 mV, (b) 200 mV. The dark line running through the center in (b) is an artifact of the simulation.

Up to this point, I have mainly discussed images of the back-focal plane of the LEEM objective lens (Fourier plane). However, the LEEM projection optics could be tuned to produced real images of the grating. Figure 3.16 shows experimental micrographs as well as simulated images of the diffraction grating under different amounts of defocus (vertical axis) for different electron landing energies (horizontal axis). Similar to the simulations of the Fourier plane, electrons were treated as particles. The white dashed line indicates perfect focus. Each panel in this figure is comprised of two sides that are color-coded for clarity: experiment on the left (blue), and simulation on

the right (red). As expected, when the electrons approach closer to the physical surface of the grating (panels on the right side), images with greater contrasts form. This increased contrast is the product of more pronounced field fluctuations near the surface of the grating.

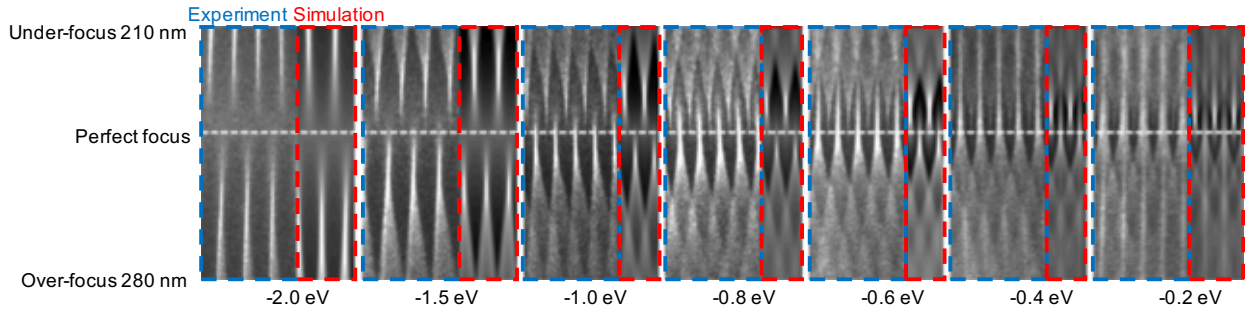

Figure 3.16: LEEM real images of the diffraction grating for different amounts of defocus (vertical axis) and different electron landing energies (horizontal axis). Each panel is comprised of two parts: experiment indicated by blue dashed lines, and classical ray tracing simulation indicated with red dashed lines.

It is worth noting that without taking into account the energy spread of the incident beam, the above simulations suffered from poor agreement with the experimental results. Therefore, although computationally intensive, the simulated images were convolved with the energy resolution of the incident beam.

The degree to which experimental and classical simulations agree both in real images as well as Fourier plane images is supportive of the hypothesis that so far the LEEM experiments have not shown coherent diffraction of electrons using my fabricated diffraction gratings. One may wonder about the mechanism by which contrast is created in the real images without coherent phase accumulation; however, S. M. Kennedy *et al.* have demonstrated that strong enough field fluctuations due to sample topography could produce image contrast due to caustics in mirror electron microscopy (MEM) [62].

As for intensity splitting at the Fourier plane, the highly simplistic MATLAB model shown in Fig. 3.17 may be illuminating. This simulation was constructed under the assumption that a collimated, monochromatic incident beam is reflected by a sinusoidal surface. Only the reflected rays are shown in order to reduce visual complexity. The focusing effects of the sinusoid's troughs send a higher concentration of rays in two distinct directions. Parallel ray clusters traveling in these two directions would form two prominent peaks on the back-focal plane of a lens placed

above the structure. The rays reflected on the crests of the sinusoid do not concentrate in such a way and contribute only to the areas in between the two prominent packs.

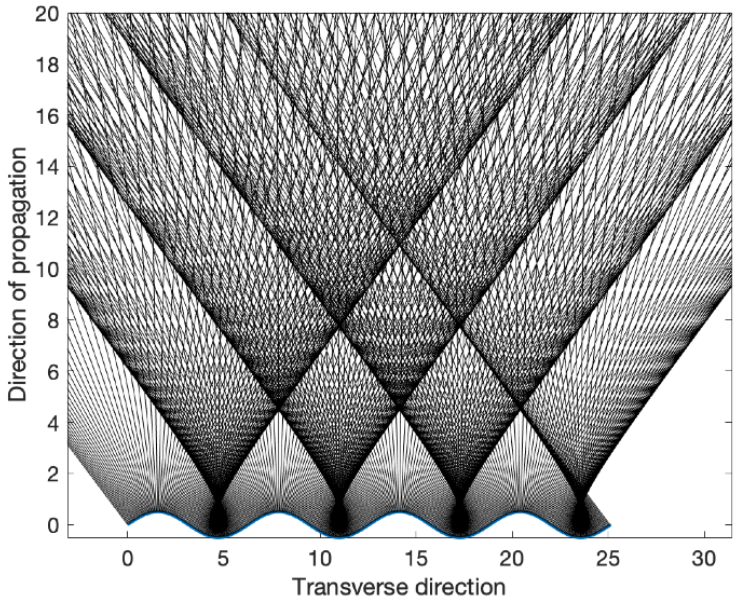

Figure 3.17: Simplistic model demonstrating the intensity splitting effects of caustics. A collimated incident beam (not shown) is reflected on a sinusoidal mirror surface. The lensing effect of the troughs concentrates reflected beams in two prominent directions. A lens (not shown) placed above this structure would focus parallel rays onto the back-focal plane, forming two bright spots.

So far, the limited $\vec{k}$-resolution of the LEEM system has prevented us from observing diffraction spots using the 500 nm period grating. After all, the LEEM system was originally designed to resolve diffraction spots caused by atomic lattices with diffraction angles up to three orders of magnitude larger. However, even after repeating the above experiments with smaller period gratings fabricated using electron-beam lithography, no diffraction spots were observed. Fundamentally, the two limiting factors of (1) $\vec{k}$-resolution and (2) beam energy spread (ΔE) are effectively at odds with each other. For instance, using smaller period gratings in an attempt to increase the diffraction angles to within the tool's $\vec{k}$-resolution entails the need to reflect the electrons at a closer distance to the surface of the grating, exacerbating the deleterious effects of chromatic dispersion. As discussed earlier, faster electrons obtain considerably more phase shift compared to slower electrons not to mention the risk of inelastic scattering resulting from collision with the grating surface.

3.3.3 Explaining the null results and future work

Although the intensity splitting observed in the LEEM experiments could be quite definitively attributed to caustics, the appearance of multiple repeated images in the SEM experiments are not fully explained as of now. The simulations and the toy model presented in Section 3.3.2 do paint a picture in which caustics lead only to two prominent intensity peaks in far-field. Therefore, for certain results such as the ones shown in Fig. 3.9 in which three distinct reflected images are observed, although caustics may be part of the explanation, it could not be the complete answer.

Other phenomena which may under certain circumstances lead to "side-images" in an SEM micrographs include AC noise and mechanical vibrations. Since the formation of a faithful image of a sample in an SEM relies upon precise placement of the scanning beam, any noise in the beam placement caused by stray electromagnetic fields or mechanical vibration may lead to appearance of side-images. However, the fact that in my experiments such images appear only in the reflected image, and never around the direct image is indicative of the fact that mechanical vibration could not be the cause. Similarly, if AC noise is the culprit, the source cannot be external for it would have impacted the direct image as well. The only noise source that would only affect the reflected image is the voltage supply used to bias the DEM system. However, noise measurements conducted on the output of this voltage supply did not reveal any systematic source structure.

Another factor distinguishing the direct image and the reflected images is the slowing down of the reflected electrons to almost a standstill near the surface of the mirror electrode. At the classical turning point where electrons spend a proportionally significant amount of time, the effects of stray electric field from potential sources such as local charges, space charge, image charge in the mirror electrode or AC noise from the supply could have a disproportionate impact on the reflected electrons.

A final experiment using a tetrode electron mirror performed in our SEM led further credence to the caustics hypothesis for the appearance of multiple reflected images. In this experiment, no diffraction grating was used; instead, the bare stainless steel mirror electrode was biased to the appropriate mirror voltage. It must be noted that although this surface was relatively flat and smooth, many small scratches left from the polishing process were present. These scratches were disordered and much larger in dimensions and depth than the nanofabricated grooves of

the diffraction gratings. As can be seen from the micrographs shown in Fig. 3.18, repeated side-images appear next to the reflected image after a deliberate misalignment of the SEM aperture is introduced. The irregular nature of these reflected images as well as the fact that they are present even at a relatively high mirror potential of $V_{\mathrm{m}} = -4050$ V when the beam acceleration voltage was -4 kV could be attributed to the less ordered and more pronounced surface topography of the stainless steel electrode. Note that similar to the previous experiments, caustics alone does not explain the appearance of more than two prominent peaks in the back-focal plane.

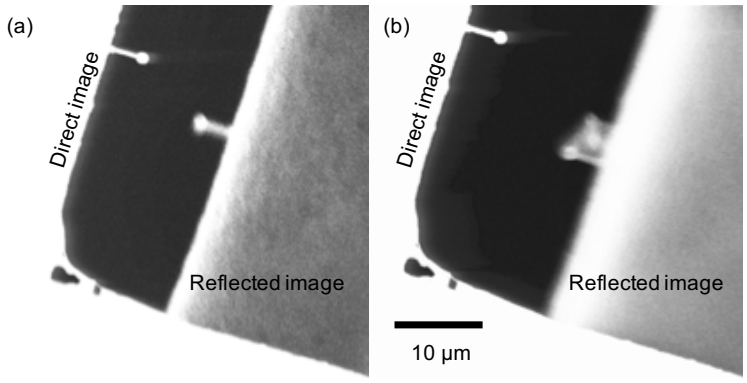

Figure 3.18: SEM experiment showing multiple reflected images even when using a "flat" stainless steel plate as mirror electrode. Direct image (left) is overexposed in order to make the reflected image (right) more visible). $V_{\mathrm{m}} = -4050$ V, $V_{\mathrm{c}} = 0$ V, $V_{\mathrm{L}} = -4853$ V. Electron acceleration voltage: -4 kV.

As discussed in Section 3.3.2, the main hypothesis as to why electron diffraction was not observed in the LEEM system is the limited $\vec{k}$-resolution of the tool used. Importantly, in 1983, in a conference proceeding, Hannes Lichte reported Fraunhofer diffraction observed from gratings with periods as large as 820 nm tested in a similar microscope as the LEEM used in our studies [63]. Figure 3.19 shows clear dependence of diffraction patterns on the mirror voltage (classical turning point height). However, the diffraction behavior shown in this result does not exactly follow the predictions of the theory as outlined by Krielaart and Kruit in [55]. Namely, central beams in Lichte's results are always the brightest region of the diffraction pattern despite the theory predicting dimming of the central beam at larger mirror potentials as shown in Fig. 3.2. Lichte attributes this deviation from the theory to the fact that the beam, with its inherent energy spread, obtains a range of phase shifts from potential surfaces above the grating. Although in many regards the LEEM system used to test my diffraction gratings is more advanced, perhaps due

to the stronger purpose-built projection lenses as well as possibly a longer microscope column, Lichte was able to resolve diffraction patterns with diffraction angles as small as 10 μrad.

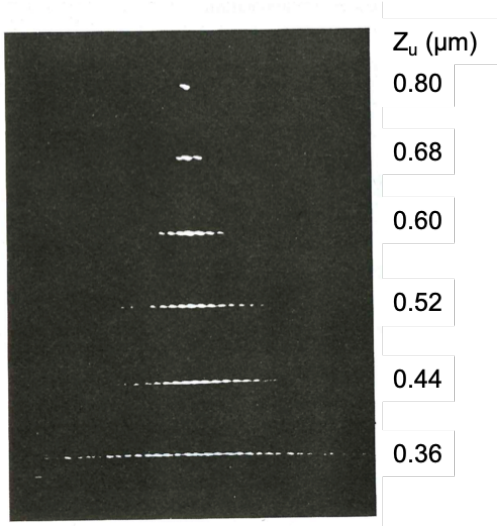

Figure 3.19: Hannes Lichte's experimental results from 1983 showing diffraction spots on the back-focal plane at various mirror voltages (indicated on the right by the height of the classical turning point). Figure adapted from [63].

Lichte's results suggest that it is possible to split electrons through diffraction using an appropriately biased diffraction grating. Given the beam energy spread in the current LEEM system, using smaller period gratings is not an option, and therefore, to replicate Lichte's results, one is faced with modifying the LEEM system to increase the distance between the mirror and the back-focal plane of the objective lens in order to take advantage of geometric magnification separating the diffraction spots. This modification would be rather complex and beyond the scope of this project at this time.

Chapter 4

Double-pass: proof-of-principle for multipass TEM

As discussed in Chapter 1, the promise of multipass transmission electron microscopy (multipass TEM) is to generate images of weak-phase objects — biological samples in particular — with a higher SNR than conventional shot-noise-limited microscopy would allow. While a 10 keV multipass TEM with an electron cavity is under construction [64], in this thesis, I discuss the simplest version of this experiment referred to as "double-pass" which could be carried out without a need for a fully developed electron cavity. This idea was first proposed by our collaborator Professor Mark Kasevich at Stanford. Designed to be conducted inside an SEM, the double-pass experiment is a proof-of-principle demonstration which takes advantage of my earlier work on SEM imaging with electrostatic electron mirrors in order to study the impact of one extra passing of incident electrons through a thin phase object. Although many aspects of this experiment including most of its components as well as its design are completed, the final assembly remains to be done.

The setup designed for the double-pass experiment is shown in Fig. 4.1. Note that with the exception of an added linear piezo stage holding a silicon detector, attached directly to the SEM pole piece, this experimental setup is identical to the one shown in Chapter 2. A stationary beam (non-scanning) is incident on a thin sample (phase grating) mounted on the nano-positioner. The transmitted beam, along with the diffracted beams (red arrows) are then reflected by the tetrode electron mirror installed below the sample atop a tilt stage. Note that the diffraction angles have been greatly exaggerated for clarity in this schematic. A P-N junction silicon detector, placed

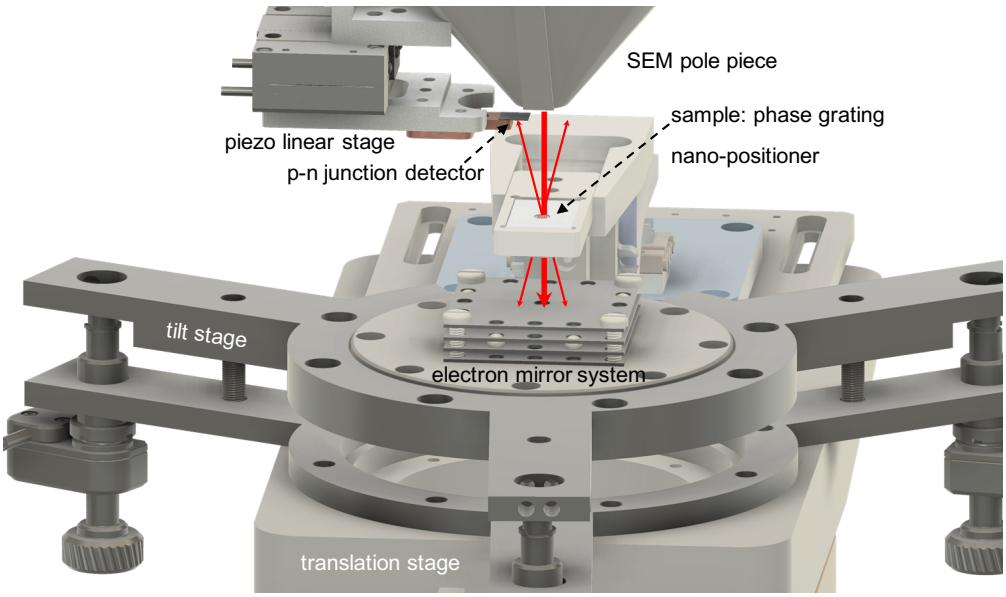

Figure 4.1: CAD of the double-pass experiment highlighting the various components involved: sample, detection, and mirror system and alignment stages. Diffraction angles have been exaggerated.

carefully near the optical axis would measure the amount of electric current present in diffracted beams. Theoretically, the double-pass experiment should yield four times as much current in diffracted beams after two passes through the sample compared to only a single pass (discussed in more detail shortly).

The experimental work in this chapter has been a joint effort between myself and John Simonaitis. Furthermore, I benefited from conversations with Dr. Akshay Agarwal, John Simonaitis, Dr. Phillip D. Keathley, and Dr. Stewart Koppell on the theory involved in this chapter.

4.1 Theory

In this section the theoretical background behind the relationship between the number of electron passes through a phase grating and intensity in the diffracted beams is discussed. Moreover, I examine the influence of phenomena such as beam shift and phase wrapping on the signal-to-noise ratio of images produced in multipass TEM.

4.1.1 Diffraction intensity as proxy for image contrast

On a fundamental level, the proposed double-pass experiment will not be able to directly show the improved SNR associated with multipass imaging precisely due to the fact that an SEM, unlike a TEM, is not capable of *imaging* in the true sense of the word. However, the amount of beam current that is transferred into the diffracted beams after the primary beam passes through a sample is an indirect measure of image contrast. An analogy between the effects of multipassing and those of sample thickness could clarify this proposed measurement. Given a purely phase object (no inelastic scattering), the thicker the sample, the greater the amount of phase shift that would be imparted onto the transmitted beam in conventional phase contrast TEM. Consequently, the amount of signal in diffracted beams increases and the end result would be an image with higher contrast and SNR. Note however that although thicker phase objects tend to produce superior image contrasts, multipass TEM addresses the issue that in practice, increasing the sample thickness is often not possible. In this section, I will discuss the theory behind the way an increase in the amount of beam phase shift after a second pass through the sample leads to higher intensity in the diffracted beams.

Consider a sinusoidal phase grating with a transmission function of $t(x, y) = \mathrm{e}^{i\frac{n}{2}\sin(\frac{2\pi x}{p})}$, where n is the phase contrast, dependent on the material and the electron energy, and p is the period of the nano-fabricated phase grating, of the order of ~ 100 nm. As shown in Fig. 4.2(a), an electron plane wave ψ_i incident on such a grating would exit the other side as the transmitted beam ψ_t, such that

$$\psi_\mathrm{t}(x, y) = \psi_\mathrm{i}(x, y)t(x, y). \tag{4.1}$$

Neglecting any normalization factor, we have

$$\psi_\mathrm{i}(x, y) = \mathrm{e}^{\mathrm{i}kz}, \tag{4.2}$$

where z is the direction of propagation and $k = \frac{2\pi}{\lambda_\mathrm{e}}$ [65]. Now, assuming that the transmitted beam exits the grating at $z = 0$, we have

$$\psi_\mathrm{t}(x, y) = t(x, y) = \mathrm{e}^{\mathrm{i}\frac{n}{2}\sin(\frac{2\pi x}{p})}. \tag{4.3}$$

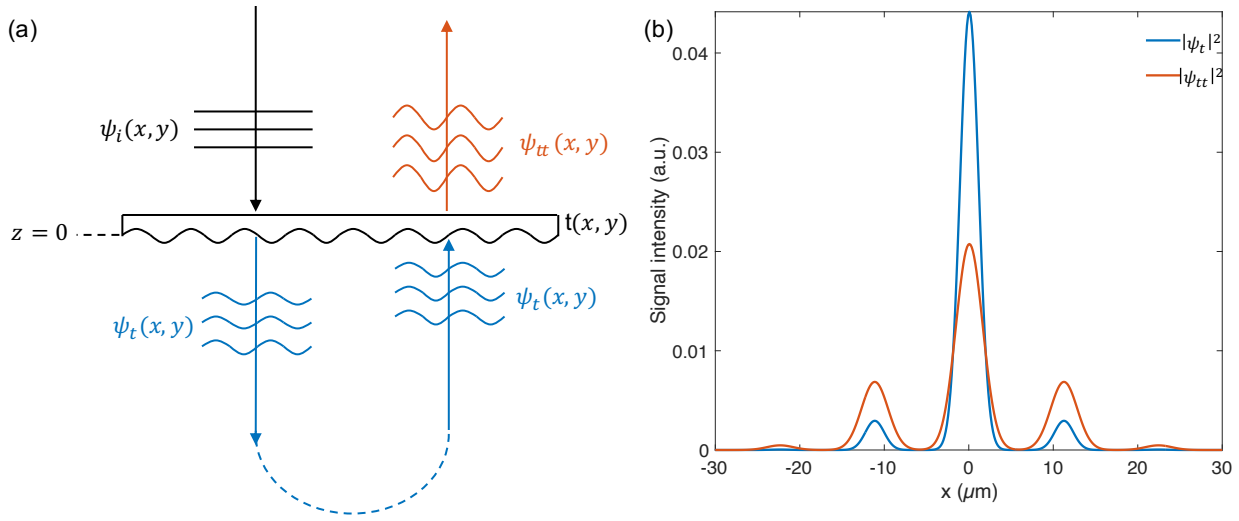

Figure 4.2: Diffraction intensity used as proxy for image contrast in the double-pass experiment. (a) An electron plane wave ψ_i is incident on a sinusoidal phase grating with a transmission function $t(x, y)$. After transmission, the exit-wave, ψ_t, is reflected and re-imaged onto the grating. The second pass through the grating produces ψ_tt. Note that technically, the reflected beam should enter the sample at the exact same region where the incident beam passed; these beams have been drawn spatially separated for clarity. (b) Calculated far-field diffraction intensities for single-pass (ψ_t) and double-pass (ψ_tt) for an electron energy of 3 keV, grating period of 100 nm, grating phase contrast of 1 (exaggerated for clarity), and grating to detector distance of 50 mm. The beam waist over the grating was set to 160 nm.

The voltages applied to the tetrode electron mirror must be set such that the exit-wave, on the bottom side of the grating would be reflected and re-imaged onto itself. This means that the same ψ_t transmits through the grating for a second time:

$$\psi_\mathrm{tt}(x, y) = t(x, y)t(x, y) = \mathrm{e}^{in\sin(\frac{2\pi x}{p})}, \tag{4.4}$$

where ψ_tt is the exit-wave after the second pass. Note that technically, the reflected ψ_t must pass through the sample at the exact same spot that ψ_i entered[1]. For visual clarity, the reflected beam is drawn with a lateral shift to the right.

The Fourier transform of the exit-waves would give us the far-field (Fraunhofer) representation of the waves. The following mathematical identity, however, would simplify this calculation

[1]For a periodic sample such as a phase grating, beam shifts that are integer multiples of the grating period lead to the same results.

[65]:

$$e^{i\alpha\sin\theta} = \sum_{q=-\infty}^{+\infty} J_q(\alpha)e^{iq\theta}, \tag{4.5}$$

where J_q is the Bessel function of the first kind. Using the above identity, we can rewrite equations 4.3 and 4.4 as

$$\psi_t(x,y) = \sum_{q=-\infty}^{+\infty} J_q(\frac{n}{2})e^{\frac{i2\pi xq}{p}} \tag{4.6}$$

and

$$\psi_{tt}(x,y) = \sum_{q=-\infty}^{+\infty} J_q(n)e^{\frac{i2\pi xq}{p}}. \tag{4.7}$$

The Fourier transform of the above equations could be written as

$$\mathcal{F}\{\psi_t(x,y)\}(x',y') = \sum_{q=-\infty}^{+\infty} J_q(\frac{n}{2})\delta(x' - \frac{2\pi q}{p}), \tag{4.8}$$

and

$$\mathcal{F}\{\psi_{tt}(x,y)\}(x',y') = \sum_{q=-\infty}^{+\infty} J_q(n)\delta(x' - \frac{2\pi q}{p}), \tag{4.9}$$

where x' and y' are the Fourier-space equivalents of the spacial variables x and y.

Equations 4.8 and 4.9 represent electron diffraction in the far-field after one and two passes through the phase grating, respectively. The δ-function captures the behavior of diffraction in the sense that only for discrete quantities of x' is the Fraunhofer field not zero.

Considering the first diffraction order, $q = 1$, it can be shown that for samples with a small phase contrast ($n << 1$), $J_1(n) = 2J_1(n/2)$ and thus $|\psi_{tt_{1st}}|^2 = 4|\psi_{t_{1st}}|^2$. In other words, by doubling the number of passes through the phase grating, the increase in phase contrast could be inferred as the intensity of the first order diffracted beam quadruples. Once again, a similar quadrupling of diffraction intensity could be expected from doubling the thickness of this diffraction grating; however, in practice increasing the sample thickness is often not an option.

Alternatively, one could simply use numerical methods to perform a Fourier transform on

the exit-waves after one (ψ_t) and two (ψ_{tt}) passes. Figure 4.2(b) shows the far-field diffraction intensities numerically calculated for a more realistic Gaussian beam, as opposed to a plane wave infinite in extent. The beam energy was set to 3 keV and the beam diameter was 160 nm at the sample plane. The sinusoidal phase grating had a period of 100 nm and a phase contrast of $n = 1$. While such a high phase contrast violates the weak-phase assumption, it was chosen for visual clarity in this example as small phase contrasts produce small diffraction intensities. Indeed the consequence of violating the weak-phase assumption becomes apparent when one computes the ratio between the amount of intensity in the first diffraction orders after one and two passes. For the example shown in Fig. 4.2(b), this ratio is 3.3, well short of the theoretical 4. Even if one incorporates higher order diffracted beams, this ratio would only increase to 3.47. For a phase contrast of $n = 0.1$, this ratio approaches 3.99.

Another consideration in the double-pass experiment is the beam diameter. In the theoretical analysis presented above, it was assumed that the incident beam was a plane wave with an infinite extent. However, in practice, electron beams have a finite extent and one must ensure that the beam diameter at the sample plane is at least as large as the period of the grating or else no diffraction could be observed. Moreover, for more efficient diffraction with well-defined spots, one should increase the beam diameter to include several periods within the beam.

4.1.2 Double-pass ray optics

The trajectory of the electrons involved in the double-pass experiment are captured in the toy model shown in Fig. 4.3 which was produced under the thin lens assumption via the ABCD matrix method on MATLAB. The effects of diffraction were manually added to the model. Note that only one positive diffracted beam is depicted to avoid clutter. As can be seen, the primary beam, shown in blue, is incident on the sample plane where a phase grating (black dashed line) is placed. As the primary beam passes through this sample, the $+1^{st}$ order diffracted beam (orange) is created and the two beams propagate towards the mirror. Note that diffraction angles have been greatly exaggerated for visual clarity. The primary and the diffracted beams are then reflected and re-imaged onto the image plane. However, the primary beam undergoes diffraction again as it passes through the sample a second time. The total diffraction intensity at the diffraction spot on the image plane has contribution from the first and the second passes. By placing an electron

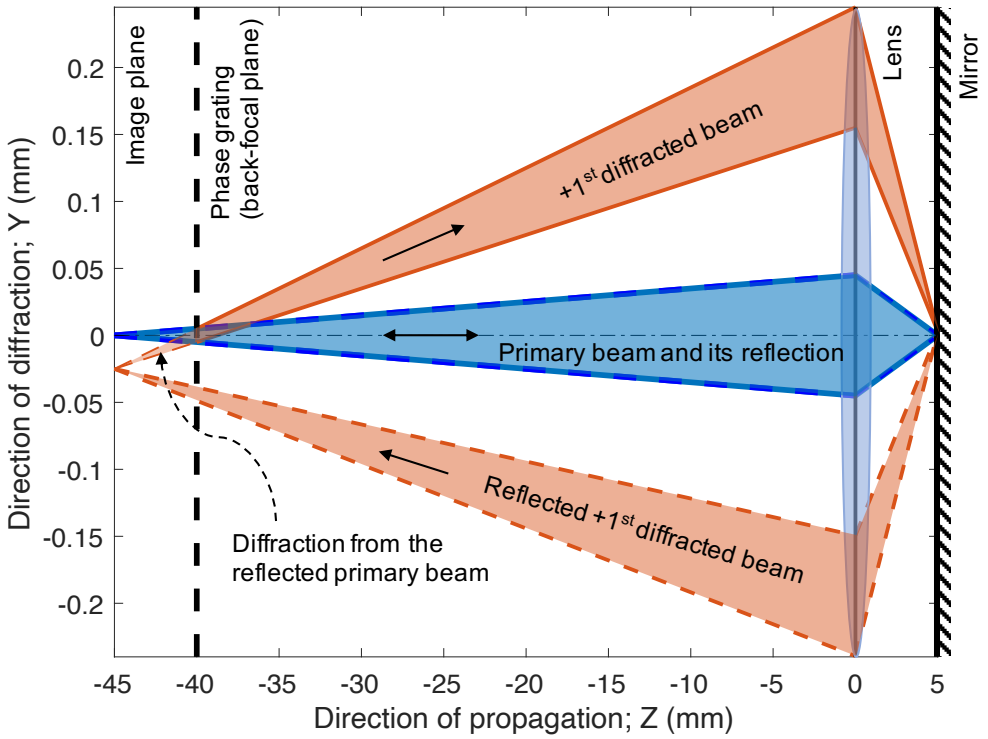

Figure 4.3: MATLAB toy model for the double-pass ray optics with exaggerated angles. The primary beam (blue) is incident on the phase grating (dashed black line), covering several periods in the illumination area. The $+1^{st}$ diffracted beam (orange) along with the primary beam propagate towards the electron mirror system. Both are reflected and re-imaged onto the image plane. The reflected, diffracted beam is outline with orange dashed lines. The reflected primary beam is once again diffracted upon its second pass, coherently adding intensity to the first diffraction spot. Note that the mirror system has been simplified to it's basic function, omitting the complexities associated with the negative lensing of the cap electrode. Diffraction angles have been greatly exaggerated for visual clarity.

detector on the image plane, one could measure the amount of current in the diffraction spot upon the second pass.

Among the practical challenges involved in this experiment is the need for the detector not to block the primary beam on its trajectory towards the sample. Furthermore, as a point of comparison, one must measure the amount of current present in the $+1^{st}$ diffracted beam after the first pass. I will discuss the potential solutions to these challenges in Sections 4.2.1 and 4.2.2, respectively.

As was mentioned above, the diffraction angle was exaggerated in Fig. 4.3 for clarity. Assuming a phase grating with a period of 100 nm and a beam energy of 3 keV, the diffraction angle would be 0.224 mrad. Using the smallest current-limiting aperture in our SEM, the smallest

convergence angle for the incident beam would be $\sim$ 1 mrad. Therefore, in reality, the primary and the diffracted beams would be overlapping throughout most of their trajectories as shown in Fig. 4.4(a). However, near the image plane where both the reflected primary and the reflected diffracted beams would be focused, the overlap is momentarily terminated and the two beams could be distinguished as shown in Fig. 4.4(b).

The concept of temporal coherence length was introduced in Section 3.1.2 but as a reminder, two parts of an electron wave are only capable of interfering with each other if the path length difference associated with the time-delay between them does not exceed the temporal coherence length. Since the double-pass experiment relies on constructive interference of diffracted beams from the first and the second passes, one must ensure that the time-delay due to the different paths the primary and the diffracted beams take is below the threshold associated with the temporal coherence length. For electrons with a nominal velocity of v_e in a continuous-wave beam, where it is assumed that the energy spread ΔE is due to incoherent phenomena, the temporal coherence length could be calculated using the following equation [66]:

$$d_{c,temp} = \frac{v_e h}{\Delta E}. \tag{4.10}$$

For a 3 keV electron with an energy spread of $\sim$ 1 eV, the temporal coherence length could be calculated to be $d_{c,temp} = 134$ nm. Based on the diffraction angle for the example of a phase grating with a period of 100 nm, and a distance of 40 mm between the sample and the lens of the tetrode mirror, the maximum path length difference could be calculated to be $\sim$ 1 nm. Therefore, the double-pass experiment with reasonable parameters for our SEM experimental setup, is well within the limit set by temporal coherence.

4.1.3 Effects of beam shift

Perhaps the most crucial aspect of multipass TEM is for the correct phase to be imparted onto the beam after each pass through the sample. Consider the case where the reflected beam does not pass through the sample at the exact same position where the original incident beam passed through. This shift would lead to the wrong phase shift being imparted onto the beam, completely nullifying any advantage from multipass TEM. Different regimes of electron mirror operation

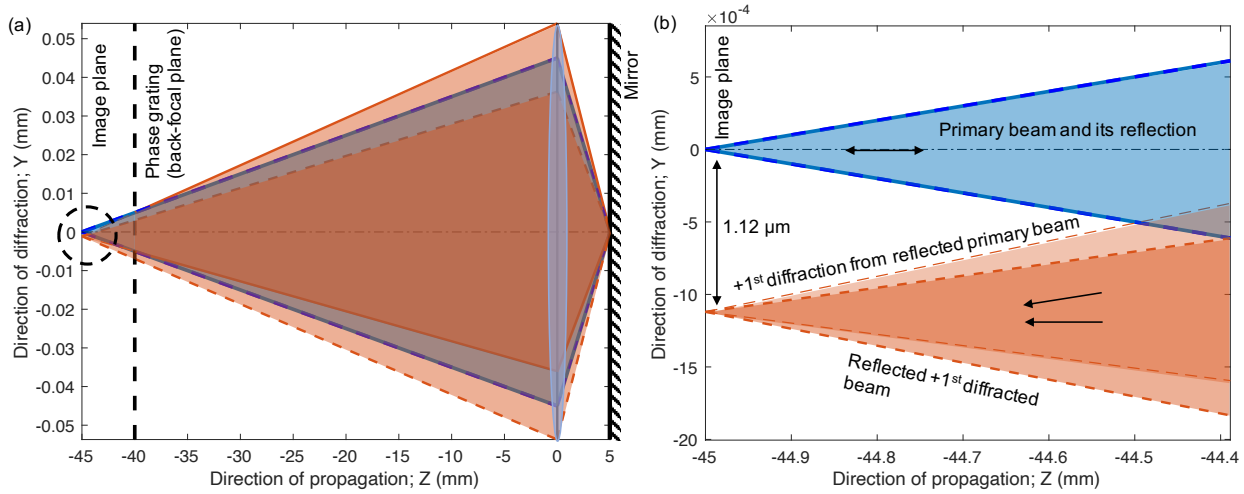

Figure 4.4: MATLAB toy model for the double-pass ray optics with realistic angles for the beam energy of 3 keV, diffraction grating period of 100 nm, and incident beam divergence angle of 1 mrad. (a) Reflected primary beam and reflected diffracted beam overlap due the divergence angle being larger than the diffraction angle. (b) The overlap is momentarily terminated near the image plane where both beams are focused. By carefully placing an electron detector on the image plane, one can measure the signal intensity in the $+1^{st}$ diffraction beam after the second pass.

were discussed in Chapter 2 and Fig. 2.3(c) shows the schematic of the regime that is appropriate for the double-pass experiment. Under this regime, the sample plane coincides with the image plane of the tetrode mirror system such that the reflected beam would be re-imaged back onto the sample. However, one of the lessons that I learned from working with the mirror system under this regime of operation is that aligning the direct image to the reflected image is not always possible due to the complexities involved in the alignment process as discussed in Chapter 2.

Alternatively, one may consider the easier-to-align mirror regime shown in Fig. 2.2(a) where the sample plane coincides with the back-focal plane of the tetrode mirror system. Under this regime, the 180°-rotated reflected beam would pass through the sample on the opposite side of the optical axis. Therefore, in general, this regime may not be used in the double-pass experiment. However, with the unique nature of the sample used in this experiment, namely a periodic one-dimensional phase grating, there is an invariance under a rotation by π about the optical axis. In other words, from the point of view of the beam, as long as the shift between the incident and the reflected beams is an integer multiple of the period of the grating, one can still ensure that the appropriate phase shift would be imparted onto the beam.

The problem arises when the beam is shifted by a non-integer multiple of the period. Figure

4.5 shows how various beam shifts defined as fractions of the grating period, p, would modulate the amount of intensity in the first diffraction order after the second pass. The expected intensity in the first diffraction order after a single pass (blue dashed curve) is included for reference. As can be seen, for certain beam shifts, not only there is no advantage to double-pass, there is a loss of signal in diffraction which equates to lower image contrast. The extreme case occurs when the beam shift after the first pass is half the period of the grating in which case due to total destructive interference, no signal is transferred to the diffracted orders and thus no image contrast could be expected. In practice, the most convenient way to ensure that the shift between the incident and the reflected beams is minimized is to try to maximize the diffraction signal after the second pass by moving the grating in the direction orthogonal to its lines by $\pm p/2$.

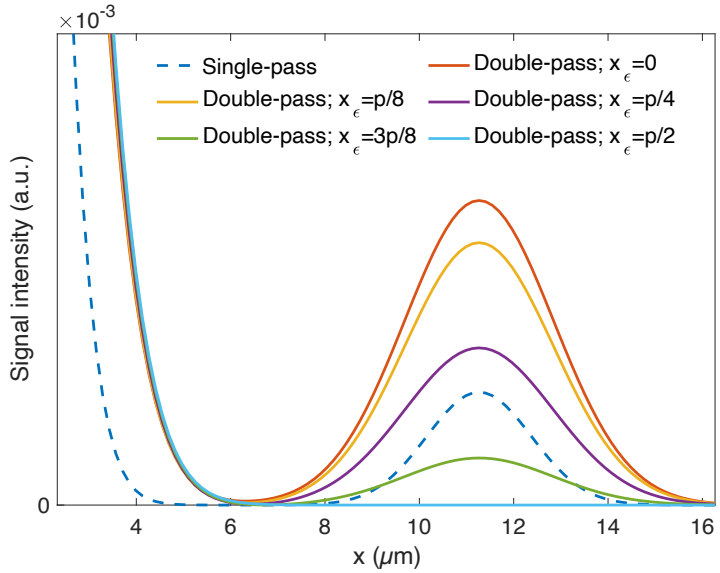

Figure 4.5: Intensity in $+1^{st}$ diffraction order for various amounts of shift between where the incident and the reflected beams passed through the sample. The shifts are defined in terms of fractions of the grating period, p. The simulation parameters were identical to the ones shown in Fig. 4.2

With beam shift having such a profound impact on the success of the double-pass experiment, one might wonder about the role of other factors such as mechanical vibration. After all, the $p/2$ beam shift from the above analysis corresponds to only a 50 nm shift for a grating with a period of 100 nm. Vibrations of this magnitude are fairly common in SEMs without active vibration cancellation platforms. However, it is important to note that the the timescales associated with mechanical vibrations and those associated with the round trip trajectory of electrons are quite

different. As it happens, mechanical vibrations tend to be most severe at lower frequencies (< 200 Hz) — milliseconds at the fastest. A 3 keV electron completes a round trip between the mirror and the sample, a distance of ~ 50 mm, in about 2 ns. Therefore, mechanical vibration, although deleterious for a multitude of other reasons, is not detrimental in the same way that beam shift due to poor alignment would be.

4.1.4 Phase wrapping

In their theoretical work on multipass TEM, Juffmann *et al.* noted that the contrast enhancing effects of phase accumulation due to electrons passing through a phase object multiple times run into diminishing returns [33]. In other words, it is not always the case that a larger number of passes through the sample would lead to images with higher SNR. The mechanism behind this phenomenon is phase wrapping. Given that the amount of phase shift imparted onto the electron beam grows linearly with the number of passes, m, at a certain point, the electrons' phase shift exceeds 2π. Beyond this point, consequent passes through the sample only add to the risk of damage and inelastic scattering without adding any useful contrast information to the final image. Figure 4.6 borrowed from [33] shows TEM simulation results demonstrating the deleterious effects of phase wrapping. In this case, an electron energy of 300 keV at a dose of 16 $e^-/Å^2$ was used to simulate images of a protein structure for different number of passes, m. Note that beyond 12 passes, there is a perceptible reduction in SNR due to phase wrapping.

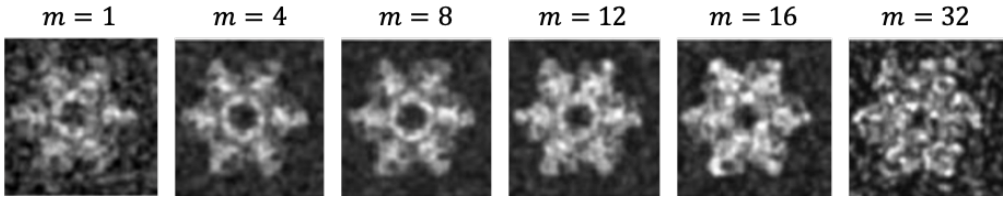

Figure 4.6: Multipass TEM simulation of a protein structure shows a decrease in contrast beyond 12 passes due to phase wrapping. Figure borrowed from [33].

The issue of phase wrapping becomes even more critical in my proposed double-pass experiment due to the fact that a given phase object imparts a more significant phase shift onto electrons at SEM energies compared to electrons at TEM energies. To avoid phase wrapping in the double-pass experiment with electron energies as low as 3 keV, one must choose samples with a low

mean inner potential: a material-specific property linearly proportional to how much phase shift a sample with a given thickness, t, imparts onto a beam with a given energy [67, 68]:

$$\Delta\phi = C_{\mathrm{E}} V_{\mathrm{MIP}} t, \tag{4.11}$$

where C_{E} is the interaction constant which depends only on the kinetic energy of the electrons.

Yang *et al.* in [68] gathered data showing the relationship between mean inner potential and mean free path for several materials as shown in Fig. 4.7. Materials appearing in the bottom right corner of this plot are generally desirable for the double-pass experiment for their low mean inner potential and high mean free path which would prevent phase wrapping and inelastic scattering, respectively. Amorphous carbon (a-C) is notable among the materials in this region of the plot. However, obtaining and handling extremely thin a-C films may not be practical. Luckily, graphene on holey carbon support structures are commercially available in thicknesses as small as a single layer of carbon atoms. Fabricating a phase grating on a single-layer suspended graphene film may be the ideal solution since this choice minimized both the thickness, t, as well as the mean inner potential, V_{MIP}, in Eq. 4.11, minimizing the potential for phase wrapping.

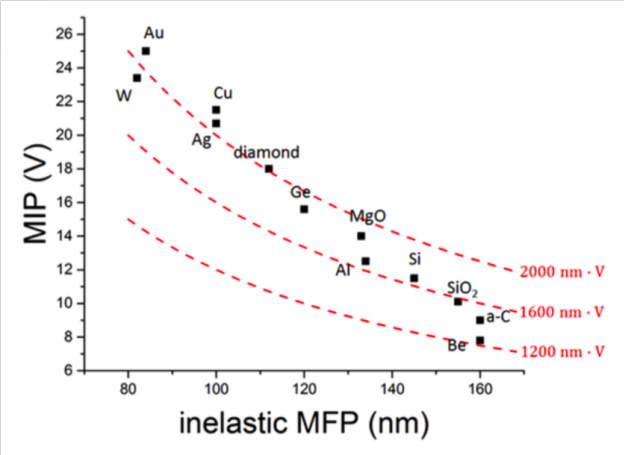

Figure 4.7: Mean inner potential and inelastic mean free path for various materials considered for the sample in the double-pass experiment. Plot borrowed from [68].

Based on Eq. 4.11 and mean inner potential estimate from [69], a single pass through single-layer graphene would impart a phase shift of $\Delta\phi = 0.08\pi$ on 3 keV electrons. In other words, this experiment is not in danger of phase wrapping until one exceeds 12 passes through the sample. Based on this calculation, if for reasons such as stability and robustness, it is more convenient

to work with thicker graphene, e.g. two-layer graphene, phase wrapping would still not be a concern in the double-pass experiment. It is only for graphene as thick as six layers that phase wrapping should be considered; however, at such thicknesses, loss due to inelastic scattering would become a major issue.

4.2 Components and challenges

In this section, I cover my progress in developing various components necessary to construct the double-pass experiment in our SEM. Furthermore, I review a number of challenges associated with this experiment as well as potential solutions to overcome them.

4.2.1 Detection

An ideal detector for the double-pass experiment would one with sub-micrometer spatial resolution in order to resolve diffracted beams (see Fig. 4.4). Furthermore, the ideal detector would have to be sensitive to currents as low as 100 fA, since only a small portion of the already-low-current primary beam would be transferred into diffracted beams. CCD-based direct electron detectors of the kind used in TEMs, or microchannel plate (MCP) detectors are two commonly used spatially resolved detectors; however, due to a number of limiting factors, they may not be used in the double-pass experiment under its current design shown in Fig. 4.1. Most importantly, the form factor of such detectors would not allow the detection of diffracted beams without blocking the primary beam. One can envision an annular detector, e.g. as an MCP with a small hole drilled into it, such that the primary beam would pass through while the reflected, diffracted beams would be intercepted by the detector. However, considering that the diffraction spot separation would be of the order of 1-2 μm, the hole would have to be smaller than the diameter of individual channels of the MCP. To make matters worse, the phosphor screen of an MCP would have to be optically imaged in order to read out the spatial information. Fitting bulky imaging optics in the current experimental setup would not be practical.

With spatially resolved detectors not being an option, a cleaved silicon P-N junction detector mounted on a linear piezo stage was used. Most commercially available P-N junctions have an oxide film protecting the surface. This transparent coating does not pose an issue for optics

applications; however, it causes charging when used for direct electron detection. Luckily, photodiodes for EUV applications are commercially available (Opto Diode Corp) without a coating which were used in this work. Figure 4.8(a) shows a picture of the cleaved P-N junction detector mounted on its holder (copper) while the inset shows the detector in its original case. Figure 4.8(b) shows a micrograph of the detector after it was cleaved and wirebonded to its holder (four wires were bonded for contingency). Appropriate measures were taken to insulate the two terminals of the P-N junction from each other. Figure 4.8(c) shows a picture of this solution implemented in our SEM. As can be seen, the piezo stage is mounted directly on the SEM objective lens pole piece while holding the detector near the optical axis.

To minimize dark noise, the P-N junction detector in this work was not biased as the inherent internal gain of the detector amplified the incident current of the 3 keV beam to levels measurable by a picoammeter. Furthermore, by adding a lock-in amplifier to this measurement setup, the noise floor was lowered significantly and in effect, the dynamic range of the current measurement was increased. With this improvement to the dynamic range, capturing different diffraction orders with significantly different amounts of signal would become easier.

With the linear motion of the stage aligned to the direction in which the diffraction pattern from the phase grating is expected to appear, one could in effect produce a spatially resolved map of the current in the diffracted beams. In practice, one could start the experiment with the detector held at a relatively large distance to the optical axis. Since very little current is expected to be transferred to high-order diffraction beams, the picoammeter would read only a background current at this initial position. Eventually, as the detector is brought closer to the optical axis, a stepwise increase in the current readout would indicate that the finite area of the detector is intercepting the diffraction pattern.

The spatial resolution of this detection scheme would be limited by the step size of the piezo as well as the sensitivity of the P-N junction detector near the cleaved edge. The piezo stage is rated for 50 nm minimum step size; however, in practice, I observed a lack of uniformity in the motion of the stage under open-loop operation which may lead to a distorted map of beam current over the image plane. Another stage with closed-loop operation may be needed. As for the edge sensitivity of the detector, it was observed that as long as the cleave resulted in an overhang, the device would be sensitive to the beam current even as close to the edge as 200 nm. As one would

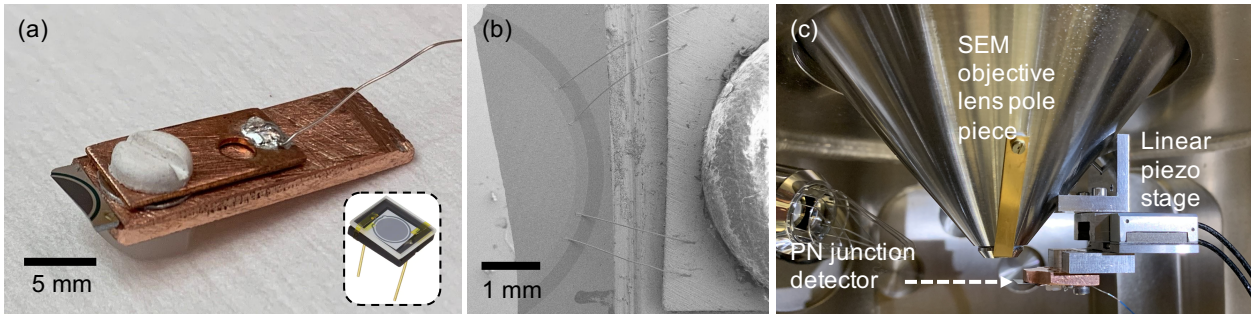

Figure 4.8: Silicon P-N junction detector used to measure the diffraction current. (a) The original detector (inset) was removed from its case, cleaved, and mounted onto a custom-made copper holder. (b) An SEM micrograph shows the four wires bonded between one of the terminals and the copper holder. (c) Photograph of the P-N junction mounted on a piezo stage that is attached to the SEM pole piece. Wire bonding done by Marco Turchetti and Marco Colangelo, MIT.

expect, the sensitivity increases with the beam incident on the bulk of the detector and away from the edge.

For convenience as well as accuracy, the movement of the linear piezo stage and the current measurement through the P-N junction and the lock-in amplifier were integrated and automated in a MATLAB script. I received significant help from John Simonaitis in this task.

4.2.2 Single-pass point of reference

As discussed in Section 4.1.1, the goal of the double-pass experiment is to demonstrate a four-fold increase in diffracted beam intensity when the electron beam passes through a phase grating twice as opposed to only once. So far, only the mechanism behind the experiment with two passes has been presented. The single-pass experiment by comparison may seem quite simple: pass the incident beam through the phase grating once and measure the current in the diffracted beams on the other side — no need to involve an electron mirror. However, such a simplistic experimental design does not take the effects of the extra optical path length, and those of the extra electron optics (tetrode electron mirror) involved in the double-pass experiment into account. As discussed in Chapter 2, the tetrode mirror, due to its inherent spherical and chromatic aberrations, would have an appreciable impact on how well the reflected beam could be focused and re-imaged. Therefore, a comparison between the results of the double-pass experiment and those of the single-pass under the aforementioned simplistic design is not exactly a comparison illuminating

of the effects of the extra pass through the sample. A valid comparison would involve minimal changes to the experimental setup between the single- and the double-pass runs.

Alternatively, one could perform a single-pass experiment in the same experimental setup designed for the double-pass experiment. Namely, the beam would pass through an intentionally created hole in the phase grating and towards the tetrode mirror system. In this case, due to a tilt in the mirror system, the reflected beam would pass through a different region of the phase grating and diffract. The upward moving primary and diffracted beams propagate towards the PN-junction detector. The carefully positioned P-N junction detector would intercept only the diffracted beams and measure their current. Figure 4.9 shows a cartoon schematic of electron trajectories associated with this proposed single-pass experiment. Note that for clarity and simplicity, all angles have been greatly exaggerated and only one diffracted beam (orange) is shown. Furthermore, the tetrode mirror system is represented by two simple elements: a flat mirror and a positive lens.

Due to a general violation of the thin lens approximation in electron optics, the effects of tilting the tetrode electron mirror system is not as intuitive as tilting light optics components. Tilting the tetrode electron mirror system would entail a reorientation of the electric fields that extend beyond the mirror system. As such, electron trajectory simulations are needed in order understand the exact behavior of the electrons and to find the appropriate mirror tilt angle for this experiment.

4.2.3 Sample fabrication

As was discussed in Section 4.1.4, in light of the two physical requirements of (1) low mean inner potential, and (2) high mean free path for the sample in the double-pass experiment, single-layer graphene would be the ideal material for the phase grating fabrication. Due to the fragile nature of suspended graphene, the only practical patterning technique which could be used to fabricate the phase gratings is focused ion beam (FIB) milling. Even with FIB, great care must be taken to optimize the energy, beam current, dwell time, and sharp focus in order to avoid rupturing the graphene. Physical criteria of the grating such as the period and the area also play a significant role in the likelihood of graphene rupturing. As one would expect, in our experience, larger areas and smaller periods were more likely to lead to failure. Figure 4.10(a) shows a micrograph of a

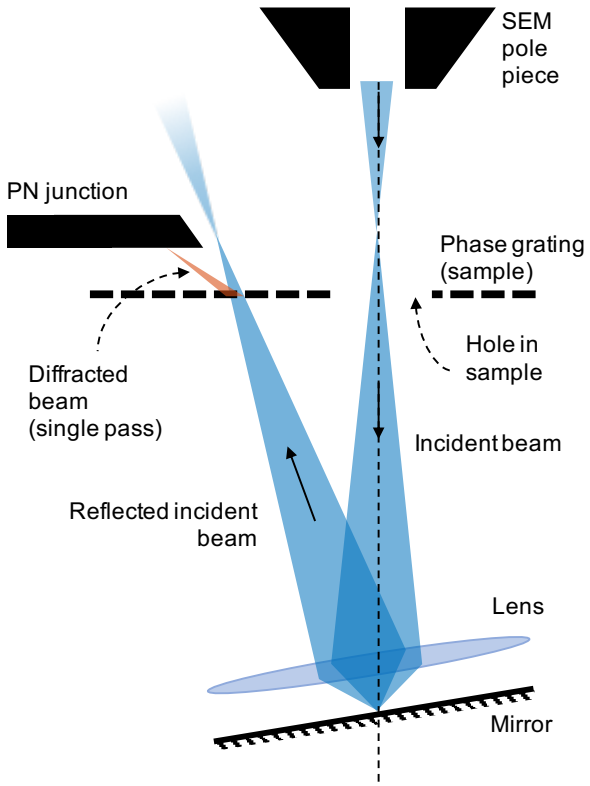

Figure 4.9: Cartoon of the proposed single-pass measurement. The incident beam (blue) would pass through a hole in the phase grating (dashed line) while a tilted tetrode electron mirror (shown in simplified form) reflects the beam towards a different region of the sample which leads to diffraction. The diffracted beam current (orange) after a single pass is measured by the P-N junction detector.

preliminary graphene grating fabricated using helium ions milling with with help from John Simonaitis and James Daley at MIT. Figures 4.10(b)-(c) show two failed attempts due to unoptimized FIB parameters. The high level of shot noise in these micrograph is due to the short averaging time and low ion beam current to avoid inadvertent milling of the sample.

The graphene grating shown in Fig. 4.10(a), has a period of 150 nm and covers an area of roughly 1.5 μm ×1.2 μm. Note that the vertical lines of the grating are not continuous since larger aspect ratio lines tended to lead to the rupturing of the graphene. This deviation from the ideal grating design is expected to limit the grating efficiency somewhat. Future fabrication efforts may be made easier if thicker, more robust graphene samples such as two-layer graphene are to be used. Phase wrapping calculations as shown in Section 4.1.4 indicate that two-layer graphene samples may still be used to fabricate a phase grating without the risk of phase wrap-

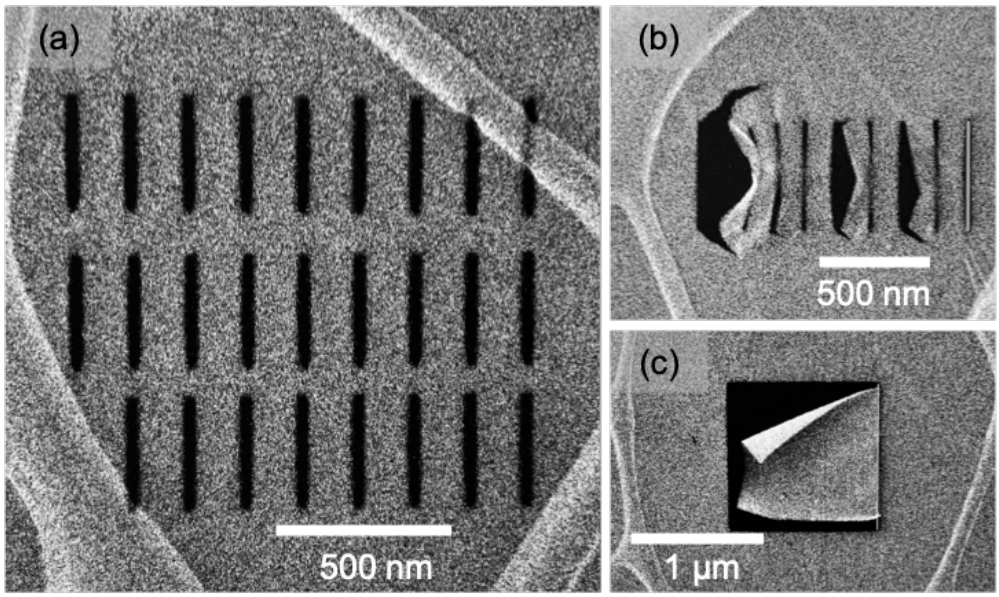

Figure 4.10: Graphene phase grating fabrication using helium ion beam milling. (a) To avoid rupturing the graphene membrane during the milling process, the grating lines had to be broken up into segments. (b)-(c) Two failed attempts due to unoptimized milling parameters. Fabrication with help from John Simonaitis and James Daley at MIT.

ping. However, one must recognize the increased likelihood of inelastic scattering when using thicker samples.

Most of my theoretical analysis for the double-pass experiment has been based on the assumption that the grating period would be 100 nm. With the thicker graphene samples, it may be possible to achieve this period without rupturing the graphene. Smaller grating periods have the advantage of increased diffraction angle which is generally desirable for ease of measurement. However, as my analysis in Section 4.1.3 demonstrated, beam shifts of the order of half the grating period between the first and the second passes through the sample would nullify any advantage due to the extra pass. Considering mirror imaging at its current state as shown in Chapter 2, the resolution of the reflected image is limited to about 100 nm. Therefore, faithful re-imaging of the reflected beam onto the grating with a period of 100 nm may require improvements to the design and assembly of the tetrode electron mirror.

4.2.4 Sample contamination

One of the challenges of the double-pass experiment, indeed a major challenge in the way of the ultimate multipass TEM tool, is sample contamination while the electron beam dwells on the sample. Made possible by the energy from the incident electron beam, polymerization of hydrocarbon molecules that are present in the vacuum chamber as well as on the surface of the sample is the process behind this contamination [6]. As Egerton and Malac point out, due to the low vapor pressure and low surface mobility of the polymerized hydrocarbons, further irradiation by the electron beam leads to the growth of a thicker contamination layer [6]. In the case of multipass TEM, where accurate phase accumulation is at the heart of the scheme, contamination which changes the effective thickness and therefore the phase of the sample could spell doom. Even in the simplified double-pass experiment, not knowing whether the increased phase shift is attributed to the second pass through the sample or due to accumulated contamination would lead to an inconclusive experiment.

Egerton and Malac listed several approaches in order to minimize the effects of hydrocarbon contamination during SEM and TEM imaging [6]. Desorbing the hydrocarbon molecules prior to polymerization in air or under vacuum through some sort of kinetic energy transfer to the sample is the underlying mechanism behind most of the suggested solutions. Examples of this approach include annealing (heating) the sample through resistive or riadiative heating [70], or ion sputtering in a plasma cleaner [71, 6]. Other innovative approaches such as cooling the sample in order to reduce the surface mobility of the hydrocarbons [72, 6] and dry cleaning using activated carbon [73] have been suggested.

Tripathi *et al.* report that for the specific case of graphene, *ex-situ* cleaning, heating the sample in atmosphere or under vacuum and then transferring it to the SEM or TEM chamber, while removing some contamination, does not accomplish an atomically clean surface over a large area. On the other hand, *pre-situ* cleaning, heating the sample in the same vacuum chamber in which viewing is performed does lead to large areas of atomically clean graphene [70]. They also show that *pre-situ* cleaning could be performed by shining a laser beam through a view port on the microscope chamber. For laser annealing, they used a diode laser: 445 nm; tunable up to 6 W. They observed effective cleaning of the graphene at 600 mW laser power with 10% duty cycle for

2 minutes which was estimated to heat the sample to a temperature range of 1100-1300°C [70].

In an effort to minimize the adsorption of hydrocarbons on the graphene surface for the double-pass experiment, a continuous wave (CW) 1470 nm, single-mode fiber-coupled laser, tunable to 11 W was used to induce *in-situ* sample heating while imaging the sample. To couple the laser beam into the chamber, we[2] installed an optics cage mount on the side of the SEM chamber such that the fiber could be affixed to a holder and held behind a lens before shining through the view port and onto the sample. Figure 4.11 shows a CAD of this structure. As can be seen, a second view port was used in order to inspect the alignment using an IR scope.

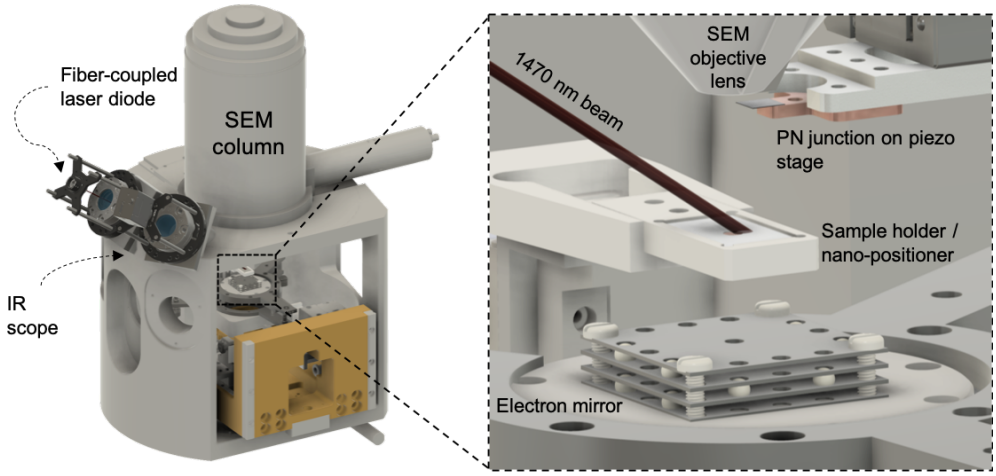

Figure 4.11: CAD of the designed laser heater solution for *in-situ* cleaning of the graphene sample. An optics cage mount holds a lens and the fiber from a continuous wave (CW) 1470 nm, single-mode fiber-coupled laser, tunable to 11 W. The laser beam is couple out of the fiber and into space before entering the chamber through a view port. Another optics cage mount holds an IR scope in front of the second view port for alignment inspection. Designed and constructed with the help of John Simonaitis, MIT.

Initial alignment of the optical cage mount, fiber holder and the lens were done using a green laser diode for convenience. Next, the alignment of the IR laser was fine-tuned by looking through the IR scope and making slight manual adjustments to the optical setup. After the alignment procedure, the optics cage was enclosed in an opaque box for safety. The laser beam covered an area of $\sim$ 3 mm^2 on the sample, similar to the area of the TEM grid on which the suspended graphene lies.

To test the efficacy of this *in-situ* cleaning approach, a plane single-layer suspended graphene

[2]I conducted all sample cleaning experiments with significant help from John Simonaitis, MIT

sample was placed in the path of the electron beam. The transmitted primary beam along with the diffracted beams induced by the graphene atomic lattice were recorded on an MCP detector placed ~ 10 cm below the sample. Note that the experimental setup inside the chamber shown in Fig. 4.11 was changed slightly: the electron mirror stack was removed to allow for transmission measurements with the MCP. Figure 4.12 shows the results of this experiment with the laser turned off (first row) and the laser operating at 2 W (second row). The electron energy was kept at 3 keV and the smallest current-limiting aperture with a nominal diameter of 7.5 µm was selected.

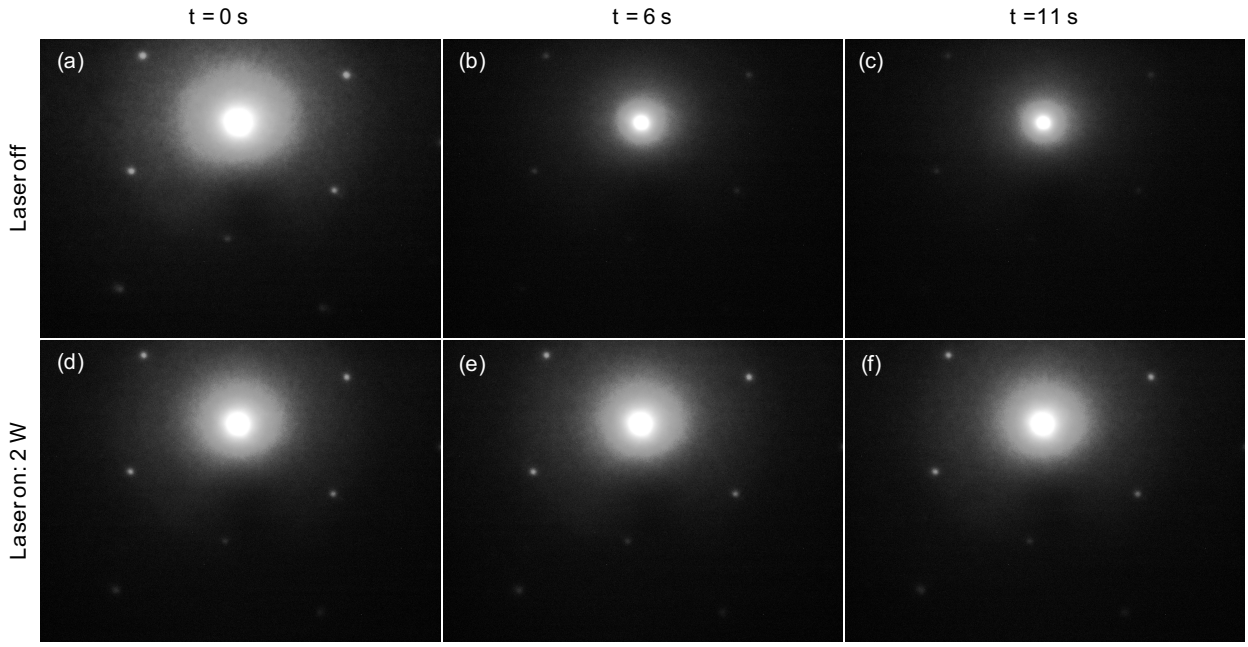

Figure 4.12: Graphene diffraction pattern recorded on an MCP detector as a 3 keV electron beam passed through a plane graphene sample. First row: (a)-(c) Without the laser shining onto the sample, the diffraction pattern fades after a few seconds due to adsorption of amorphous hydrocarbon contamination. Second row: (d)-(f) With the laser operating at 2 W, the diffraction pattern persists for a relatively long time.

As can be seen in Fig. 4.12(a)-(c), without the laser shining on the graphene sample, the diffraction pattern fades away within a few seconds. This phenomenon could be attributed to the adsorption of amorphous hydrocarbons on the otherwise crystalline graphene and reducing the overall crystallinity. Perhaps more severely, the added contamination effectively increases the sample thickness which leads to a reduction of electron transmission as apparent from the dimming of the central beam in Fig. 4.12(b)-(c). This effect would be greatly detrimental to the

double-pass experiment. Next, the laser was turned on and the power was gradually increased while viewing the diffraction pattern. As shown in Figure 4.12(d)-(f), it was observed that at 2 W, the diffraction pattern persisted over a relatively long time with no visible damage appearing on the surface of the sample upon later investigation.

To quantify the effectiveness of the laser heater in maintaining a clean graphene surface and by extension preserving the diffraction pattern over time, an image processing code was developed on MATLAB to track the time evolution of intensity in the first-order diffraction spots. Figure 4.13 shows the results for the two cases of "laser on" and "laser off". As can be seen, with the laser shining on the graphene, aside from the initial drop within the first few seconds, the diffraction intensity persists with only a small decrease over the 40 s duration of the experiment. with the laser turned off on the other hand, a rapid accumulation of contamination led to a severe decrease in diffraction intensity to the point that the experiment was terminated in less than 10 s. It is believed that through optimizing the laser power, it would be possible to minimize the observed initial drop in diffraction intensity as well as the consequent gradual decrease in the intensity with the laser shining over the sample.

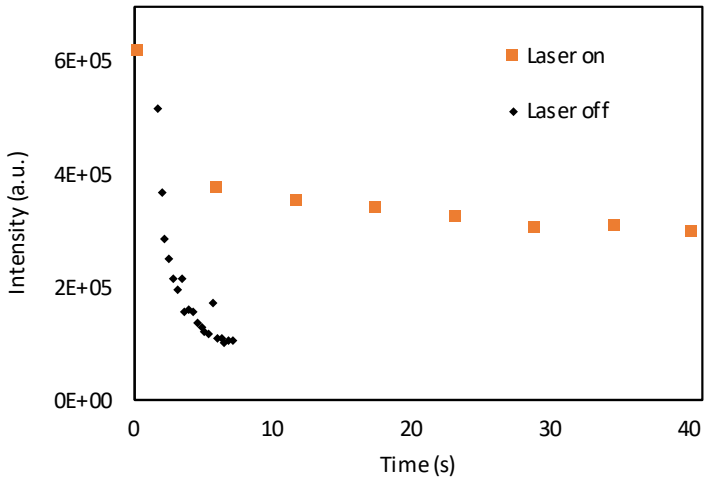

Figure 4.13: Time evolution of intensity in the first diffraction order with the laser off (black diamonds) and the laser on (orange squares). The initial rapid drop as well as the gradual decrease in diffraction intensity with the laser shining on the graphene is attributed to unoptimized laser power.

Similar to the approach taken by Tripathi *et al.* in [70], in all the above experiments, the laser power was iteratively increased until cleaning was observed. With an accurate understanding of

radiative heat absorbed into the sample and heat radiated and conducted out of the sample into the holder and ultimately the chamber, one could construct a model relating laser power to sample temperature. Without such a model at this time, the steady state temperature of the graphene in this work is unknown. It has been reported that graphene samples are destroyed when heated to above 1100—1300° C [70]. Evidenced from the appearance of cracks on the graphene at 3 W as shown in Fig. 4.14(b), one can make a broad estimate that at 2 W, the power at which effective cleaning was observed, the graphene was heated to just below that temperature range. At even higher laser powers, the crack formation on the graphene is exacerbated as seen in Fig. 4.14(c). The appearance of speckles distributed fairly uniformly over the graphene as well as the holey carbon support film is another evidence of damage to the sample shown in Fig. 4.14(d). The exact nature of these speckles are not currently known; future measurements are needed to determine their elemental composition.

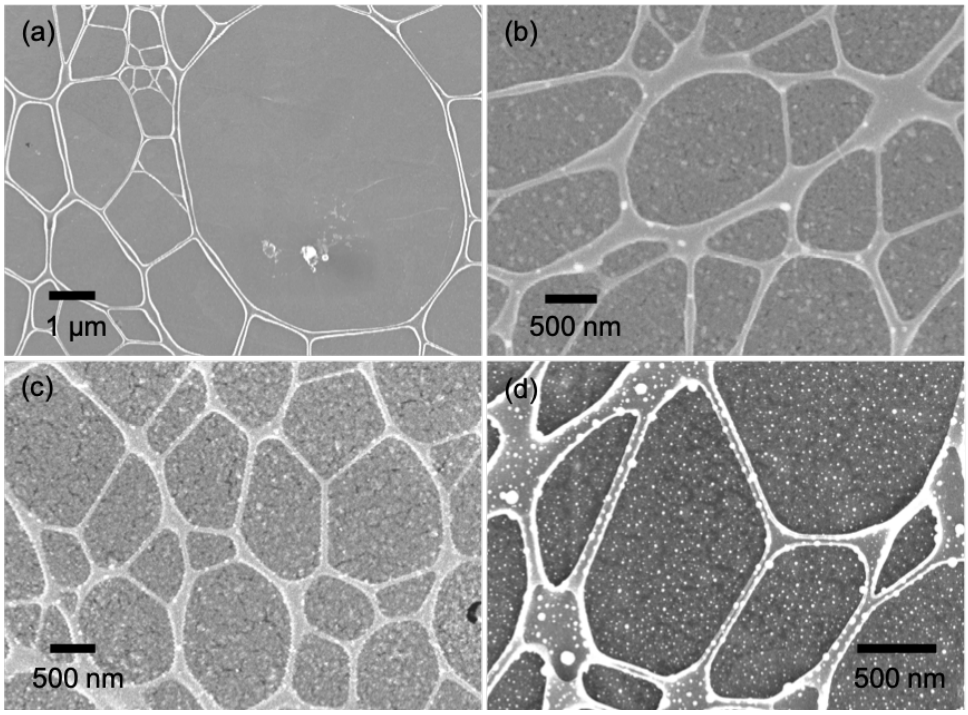

Figure 4.14: Laser beam-induced damage to the graphene sample. (a) Reference micrograph showing the smooth surface of the graphene sample when the laser power does not exceed 2 W. Cracks and bright speckles appear on the surface after exposure to laser powers of (b) 3 W; (c) 5 W; (d) 7 W. Note that due to an unknown coupling efficiency, it is not clear how much of the nominal laser power is directly involved in heating the sample.

Another factor determining the fraction of the laser power that is deposited into the graphene

as heat is the laser polarization. It is known that when polarized in the direction parallel to the surface of the graphene, the laser radiation would be more effective at heating the graphene. In this work, due to the availability of sufficient laser power, I did not experiment with laser polarization. Through a minor adjustment to the setup: adding a $\pi/2$-phase plate, one could polarize the incident laser beam and in theory achieve a similar level of cleaning at a lower laser power.

It must be noted that although the laser-induced cleaning discussed in this work does prevent the hydrocarbon molecules from polymerizing and forming a strong bond to the surface, if such polymerization has already occurred, laser heating will not remove the contamination. To demonstrate this phenomenon, a stationary focused electron beam was incident on a graphene sample for several seconds. Next, the laser was turned on and the same experiment was repeated while the sample was being heated. Hydrocarbon contamination deposited while the laser was off appears as bright spots on the surface of the graphene as shown in Fig. 4.15. The contamination induced with the laser turned on appears as much fainter streaks as indicated in Fig. 4.15. The brighter nature of the contaminated spots compared to their surroundings is due to the higher efficiency of secondary electron generation in the now thicker contaminated regions. Note that upon laser irradiation, the contaminated regions were not cleaned. Egerton and Malac attribute this to the low mobility of the polymerized hydrocarbon molecules. At sufficiently high laser powers it may be possible to remove the contamination but at great risk of destroying the sample.

Although the apparent contamination is notably less severe with the laser turned on, it must be noted that the streak-like shape of the contaminated regions as indicated in Fig. 4.15 suggests significant sample drift. The most likely cause of sample drift in this experiment is thermal expansion due to heating. A dedicated experiment was designed and conducted in order to better understand the drift behavior. Figure 4.16 shows a plot of sample drift along two directions as a function of time since the laser was turned on.

In general, the x-directed drift is more severe than the y-directed drift. This observation may be attributed to the form factors of the sample holder as well as the nano-positioner atop which the sample is mounted: both are longer in the x-direction. As can be seen, the x-directed drift does largely subside during the 1 h period of this experiment perhaps due to the system reaching

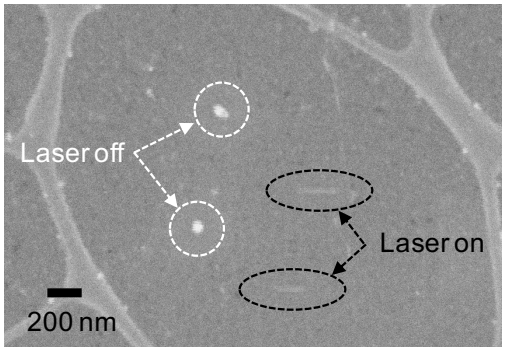

Figure 4.15: Polymerized hydrocarbon molecules cannot be removed upon laser irradiation. To demonstrate this effect, the electron beam was focused onto the graphene surface in two trials while the laser was turned off. Next, the laser was turned on and the experiment was repeated. The contamination was not removed after turning the laser on. The streak-like nature of contamination with the laser on is due to sample drift caused by thermal expansion.

thermal equilibrium. Two lessons can be drawn from this experiments: (1) some conditioning may be necessary before one begins the double-pass experiment; (2) orienting the lines of the diffraction grating along the x-direction may minimize the deleterious effects of drift on adding the phase shift of the drifted sample onto the beam. Ultimately, drifts of this speed would not pose a serious risk to the double-pass experiment as the time-scales associated with an electron round trip are orders of magnitude shorter than the time-scales associated with drift as measured in these experiments.

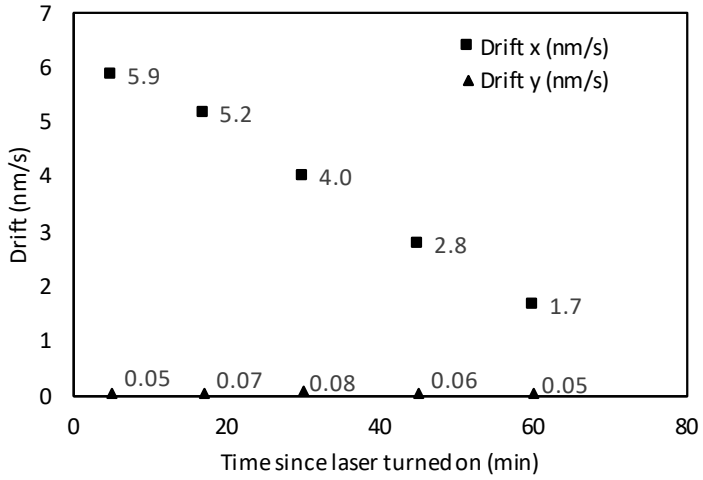

Figure 4.16: Heating-induced sample drift as a function of time since the laser was turned on.

By taking the concept of *pre-situ* laser-induced cleaning introduced by Tripathi *et al.* [70] one step further, I demonstrated true *in-situ* cleaning by maintaining laser irradiation on the

graphene while imaging with electrons to ensure minimal adsorption of hydrocarbon molecules. This development would be critical to the success of the double-pass experiment. As for the ultimate multipass TEM, as long as the sample under investigation can withstand the kind of temperatures needed to desorb hydrocarbon molecules, this technique would prove beneficial in preventing contamination. However, it is safe to assume that laser-heating of the sort shown in this work would be highly damaging to biological samples. More work is needed to understand the effects of short laser pulses in removing surface contamination without increasing the temperature of biological samples to the point of destruction.

4.3 Putting it all together and future work

With many of the components of the double-pass experiment such as the tetrode electron mirror, the laser heater, and the P-N junction detector being completed and other components such as the graphene phase grating nearing completion, the next major step in this project is assembly inside the SEM chamber.

Eventually, improvements to the performance of the tetrode electron mirror would be necessary as currently the resolution of the reflected images is limited to $\sim$ 100 nm as demonstrated in Chapter 2. This resolution limit places a lower bound on how small the period of the phase grating could be without beam shift after reflection impacting the results to an appreciable degree (see Section 4.1.3). One promising approach to improving the performance of the electron mirror system is to use high-precision MEMS fabrication techniques, as demonstrated by Kruit in [57], to achieve a higher degree of aperture roundness and alignment between the mirror electrodes.

The importance of lateral (spatial) coherence in the context of the double-pass experiment was discussed in Section 3.1.2: the lateral coherence length must be longer than the period of the phase grating being tested. However, measuring the lateral coherence length of the beam is not straightforward. An indirect way to triangulate this length is to place gratings of incrementally increasing periods in the path of the beam and recording the diffraction pattern that they produce. The beam must be defocused over the grating such that several periods of the grating are within the are of illumination. So long as a given grating produces a diffraction pattern, one can assume that the lateral coherence length of the beam is at least as long as the period of that particular

grating. Eventually, for a grating with a large enough period, no diffraction would be recorder — an upper limit on the beam's lateral coherence length. Suspended gold-coated silicon nitride gratings of the kind shown in [74] were acquired in order to attempt this experiment soon.

To make matters more complex, it is possible for a grating to produce a diffraction pattern even if the beam is not fully coherent over the entire area of illumination. In the context of Young's double slit experiment, one would observe a lower fringe contrast if the beam is only partially coherence. McMorran and Cronin studied the effects of partial coherence in the context of a two-grating experiment using the Gaussian Schell-model (GSM) [75]. The schematic of the experiment under study is shown in Fig. 4.17. Avoiding all the gory details, their approach works by calculating the mutual intensity function, a tool that keeps track of the beam's intensity, lateral coherence length, and phase of a partially coherence optical field. Next, Zernike's general propagation law for fields with arbitrary coherence properties is used under the paraxial approximation in order to advance the fields along the direction of propagation after transmission through the gratings [75].

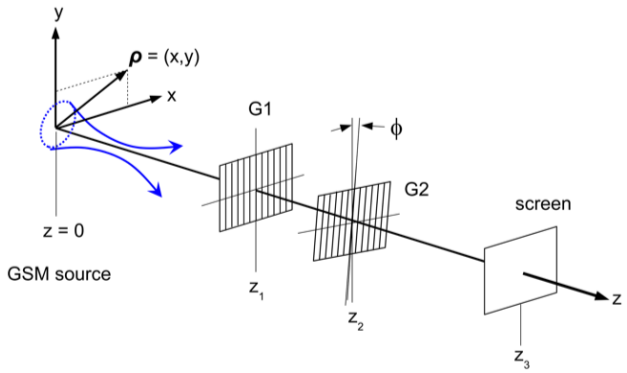

Figure 4.17: Schematic of a two-grating experiment used by McMorran and Cronin to study the effects of beam partial coherence through the Gaussian Schell-Model (GSM). Figure borrowed from [75].

As suggested by the schematic shown in Fig. 4.17, many variables such as the distance between the gratings and their relative rotational angle could be adjusted in this model. In certain ways, the double-pass experiment is similar to this experiment: with a lens added between the two gratings, such that the first grating could be imaged onto the second grating, one achieves a simplified version of the double-pass experiment omitting the need for an electron mirror element. In fact, in my research into the effects of partial coherence, I made an attempt to model the

double-pass experiment using GSM. However, without computational optimization, the calculations proved to be too intensive in terms of the need for processing power and memory. Future work in this area could be beneficial not just for understanding the effects of partial coherence but also for understanding the effects of less-than-perfect re-imaging of the beam onto the grating due to effects such as beam rotation.

Chapter 5

Conclusions and outlook

In this thesis, I presented my contributions in developing various components for two novel electron microscopy schemes referred to collectively as Quantum Electron Microscopy (QEM). The ultimate goal of QEM is to allow for atomic-resolution imaging of biological samples such as proteins while reducing electron beam-induced damage to them. Accomplishing this goal would equip us with a tool to study phenomena such as protein misfolding, the basis for numerous diseases.

In the first of the two aforementioned low-damage electron microscopy schemes, the aim was to bring the concept of interaction-free measurement (IFM) to electron microscopy. To that end, I developed electrostatic electron mirrors which could be installed in an SEM. I demonstrated that the mirror could be used to produce simultaneous scanned images of the top and the bottom surfaces of a sample. Moreover, by adjusting the voltages applied to the mirror, I demonstrated various regimes of mirror operation defined by the electron trajectories and the properties of the resulting micrographs. The resolution of images produced with the mirror was approximated to be 100 nm.

Building upon my work on electron mirrors, I designed and fabricated diffractive electron mirrors (DEMs) in order to demonstrate the other crucial component of the IFM experiment: a lossless electron beam splitter. I attempted to demonstrate coherent electron diffraction using the fabricated DEMs in our SEM; however, due to the shortcomings of the SEM system as outline in the body of this thesis, I was not able to demonstrate coherent splitting of electrons by diffraction. Our collaboration with Dr. Tromp and the consequent testing of my DEMs in his LEEM system,

although informative, failed to yield the results that we were hoping for. Namely, we observed splitting of the electron beam at the Fourier plane; however, more in-depth analysis suggested that an incoherent electron optical phenomenon known as caustics was responsible for the splitting.

In the second scheme, multipass TEM, the aim was to improve the signal-to-noise ratio of phase contrast TEM imaging by passing the probe electrons through a weak phase object multiple times in order to accumulate phase. With an electron cavity being at the center of this scheme, my work on tetrode electron mirrors would be an integral part of multipass tool currently under construction. Furthermore, I developed a number of components for a proof-of-principle to demonstrate the simplest form of multipass with electrons: the double-pass experiment. I investigated the criteria that one must consider before fabricating the phase grating test sample for the multipass experiment. For instance, my calculations into the effects of beam shift indicate that the period of the phase grating must not be smaller than the resolution of the image that the electron mirror forms on the sample upon reflection. Moreover, I demonstrated how critical it would be in the multipass scheme to avoid hydrocarbon contamination in order to prevent the wrong phase shift being imparted onto the beam. I believe the laser heater developed in this thesis to prevent hydrocarbon contamination would be an important accessory to the ultimate 10 keV multipass TEM tool which is currently under construction.

In the next two sections, I will outline the future work needed in order to improve upon the components and the proof-of-principle demonstrations that I presented in this work, as well as the potential applications of the aforementioned components in areas other than the QEM project.

5.1 Future work

In this section I will present ways in which the tetrode electron mirror, the diffractive electron mirror, the laser heater, and the graphene phase grating could be improved in the future. Moreover, I will introduce potential analyses which may illuminate the reasons behind the null results associated with the DEM experiments.

5.1.1 Improvements to the tetrode electron mirror

With my current approach to fabricating tetrode electron mirrors, namely using traditional machining techniques, the best observed resolution for the reflected image is about 100 nm. Further improvements to the mirror quality would have to involve higher-precision fabrication methods in order to achieve rounder aperture holes, smoother aperture edges and flatter mirror electrodes. Furthermore, the method by which the four electrodes of the tetrode electron mirror are assembled plays a crucial role in how well the central apertures line up. I used precision ceramic balls, plastic bolts and nuts to assemble the electrodes. However, with the holes in each plate being machined independently, the alignment between the central apertures would not be optimal. MEMS fabrication techniques are known to provide superior precision compared to traditional machining [57]. I believe that the next generation of tetrode electron mirrors for use in the QEM project would allow for imaging at a significantly better resolution.

5.1.2 Improving LEEM's $\vec{k}$-resolution

A hypothesis as to why we did not observe coherent electron diffraction using my fabricated DEMs in the LEEM system is the limited $\vec{k}$-resolution of the tool. LEEM was originally designed to resolve the diffraction patterns created by the atomic lattice of crystals. The diffraction angles associated with atomic crystal diffraction is about three orders of magnitude larger than that of the nanofabricated DEMs in the LEEM experiments. Therefore, it is possible that with an improved $\vec{k}$-resolution, the LEEM system would be able to resolve the diffraction spots on the Fourier plane of the objective lens. Improving the $\vec{k}$-resolution of the system could be achieved by modifying the projection optics or by increasing the length of the LEEM column in order to take advantage of the geometric magnification further separating the diffraction spots to the point that they could be resolved with the projection lenses.

5.1.3 Optimizing the Laser heater

As demonstrated in Chapter 4, the laser heater designed to keep the graphene sample clean from hydrocarbon contamination proved effective in my experiments. However, it was also observed that the diffraction intensity goes through an initial dip associated with adsorption of hydrocar-

bon contamination. It is noteworthy that in this work, I incrementally increased the laser power until I observed persistent diffraction patterns. I believe that with an optimized laser power, it is possible to avoid the initial deposition of hydrocarbon molecules on the surface. Furthermore, by developing a model in the future to relate the laser power to the sample temperature, it would be possible to more effectively clean the sample while not exceeding the temperatures that cause damage to the graphene. Such a model would have to capture the form factor of the graphene-on-holey-carbon sample accurately in order to determine the rate at which the laser power is absorbed and the rate at which heat is radiated or conducted away from the sample. Finally, by polarizing the laser beam in the direction parallel to the surface of the graphene, it would be possible to more effectively heat the sample at a lower laser power since a higher portion of the power would be involved in heating the graphene.

5.1.4 Graphene phase gratings

In Chapter 4, I demonstrated the prototype single-layer graphene phase grating fabricated using helium ion milling. However, due to the graphene rupturing, we were limited to a period of 150 nm. In light of my analysis of beam shift and the limited resolution of my current mirror design, periods smaller than 150 may not even be desirable. But it must be noted that with higher quality mirrors, and with the ultimate multipass TEM tool, phase gratings with smaller periods would be needed.

Brand *et al.* demonstrated the use of suspended graphene gratings as matter-wave beam splitters [76]. In their work, they achieved grating periods as small 88 nm using a single-layer graphene film. However, they observed that with relatively long aspect ratios, the graphene ribbons rolled up into a tube as shown in Fig. 5.1(a)-(b). The issue was resolved when they moved to two-layer graphene as the extra rigidity prevented the ribbons from rolling up as shown in Fig. 5.1(c). Considering that my analysis of the mean inner potential of graphene indicated that even with two-layer graphene we would be safe from phase wrapping, I believe that using two-layer graphene for more uniform, larger area phase gratings is the ideal solution.

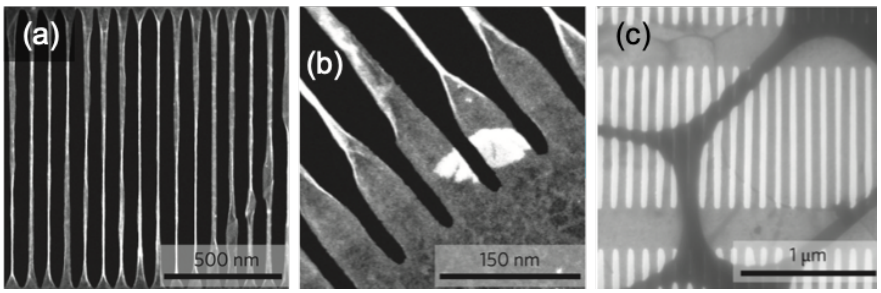

Figure 5.1: Graphene phase gratings fabricated through focused ion beam milling into (a)-(b) single-layer and (c) two-layer graphene. Large aspect ratio of the lines in the single-layer graphene gratings led to rolling up of the ribbons. Figure adapted from [76].

5.1.5 Further investigation into the DEM null results

Aside from general alignments and electron optical improvements to the system in the hope of observing electron diffraction in the DEM experiments, one must consider more fundamental obstacles as well. One such obstacle is the lateral coherence length of the electron beam. As I mentioned in Chapter 3, no diffraction could be expected if the lateral coherence length of the beam is smaller than the period of the DEM. In all SEM experiments presented in this thesis, I operated the tool with the smallest current-limiting aperture in place in the hope of maximizing the portion of the beam that is fully coherent. Although this strategy negatively impacts shot noise, maintaining spatial coherence takes precedence. Loss of coherence through various mechanisms such as inelastic scattering, aloof beam excitation, Johnson noise [77], etc must be considered as a potential cause of the null results. In a future experiment, one can place diffraction gratings of increasing periods in the path of the spread-out incident electron beam while recording the diffraction pattern underneath as a test of the upper bound of the beam coherence length. At the point when a diffraction grating does not produce a diffraction pattern, one can conclude that that period is larger than the coherence length of the beam.

Another fundamental obstacle in the way of observing electron diffraction with the DEMs is surface nonuniformity. In discussions with Professor Peter Hagelstein at MIT[1], it became clear that although the exponential decay expressed in Eq. 3.1 would ensure that the higher-frequency terms from the surface would decay quickly, any slow-varying nonuniformity over the length scales of one period would cause sufficient phase disturbances to prevent any observation of co-

[1]Prof. Hagelstein is a member of my thesis committee

herent diffraction. Moreover, such nonuniformities could be detrimental to the DEM experiments even at ångstrom-level surface nonuniformities. Perhaps on a hopeful note, this issue could be somewhat avoided in the QEM application of the DEM since it is a requirement for the beam splitter to sends only a small portion of the signal to the diffracted beams, and hence one must tune the mirror voltage such that the electrons are reflected at a relatively large distance from diffraction grating, where the effects of surface nonuniformities are attenuated. I would be beneficial to study the surface nonuniformities of the sample in a future study.

Appendix

The SEM used in all diffractive electron mirror (DEM) experiments is a Zeiss LEO 1525 with a Schottky field-emission source, equipped with a custom three-axis stage attached to the door. The smaller form factor of the custom stage in comparison with the original five-axis Zeiss stage, provided us with extra space in order to construct various electron optical experiments. Furthermore, a designed through-hole at the center of the stage allows for transmission experiments. The CAD in Fig. 5.2 shows the SEM. This tool is quipped with a turbomolecular pump installed on the bottom of the chamber, offset from the optical axis in order to allow for transmission measurements along the optical axis. The chamber vacuum tends to reach mid-10^{-6} mBar.

In DEM experiments conducted in this SEM, due to the tendency of the electron optical elements biased to high voltages to experience electrical breakdown (arcing), I had to gradually increase the voltages applied to the tetrode mirror and allow for conditioning. This entails waiting for several hours until an acceptable vacuum level is established (mid-10^{-6} mBar), ramping up the voltages until arcing is observed and then waiting until arcing subsides. The incremental voltage increase followed by conditioning time is repeated until the desired voltages are reached. This process would take between 1 hour to 2 hours depending on the vacuum level and the cleanliness of mirror electrodes in terms of dust and other particles. To reduce the arcing probability, I sonicated the mirror electrodes in acetone and IPA for 5 min each and then assembled the tetrode mirror in a cleanroom.

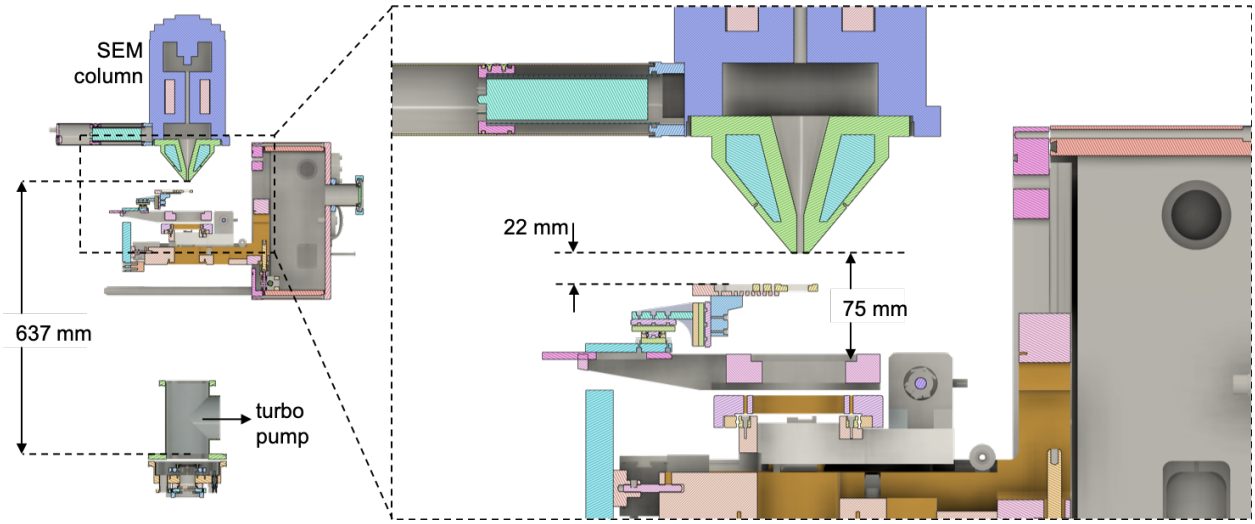

Figure 5.2: CAD of the SEM in which the DEM and the double-pass experiments were conducted. Note that the distances as they are indicated, correspond to the stage's lowest position. Often in my experiments, I raised the stage in order to avoid an unnecessarily long electron working distance. In this CAD, the distance from the bottom of the SEM objective lens pole piece to the bottom electrode of the mirror system (not depicted) would be 75 mm. CAD made by John Simonaitis.

Bibliography

[1] D. B. Williams and C. B. Carter, "The Transmission Electron Microscope," in *Transmission Electron Microscopy: A Textbook for Materials Science*, pp. 3–17, Boston, MA: Springer US, 1996.

[2] U. Kaiser, J. Biskupek, J. C. Meyer, J. Leschner, L. Lechner, H. Rose, M. Stöger-Pollach, A. N. Khlobystov, P. Hartel, H. Uller, M. Haider, S. Eyhusen, and G. Benner, "Transmission electron microscopy at 20 kV for imaging and spectroscopy," *Ultramicroscopy*, vol. 111, pp. 1239–1246, 2011.

[3] M. Haider, H. Rose, S. Uhlemann, B. Kabius, and K. Urban, "Towards 0.1 nm resolution with the first spherically corrected transmission electron microscope," *Journal of Electron Microscopy*, vol. 47, pp. 395–405, 1 1998.

[4] M. Haider, H. Rose, S. Uhlemann, E. Schwan, B. Kabius, and K. Urban, "A spherical-aberration-corrected 200 kV transmission electron microscope," *Ultramicroscopy*, vol. 75, pp. 53–60, 1998.

[5] N. De Jonge and D. B. Peckys, "Live Cell Electron Microscopy Is Probably Impossible,"

[6] R. Egerton, P. Li, and M. Malac, "Radiation damage in the TEM and SEM," *Micron*, vol. 35, pp. 399–409, 8 2004.

[7] V. E. Cosslett, "Radiation damage in the high resolution electron microscopy of biological materials: A review*," *Journal of Microscopy*, vol. 113, pp. 113–129, 7 1978.

[8] M. J. Prieto, T. Schmidt, and E. Bauer, "Low energy electron microscopy," *Reports on Progress in Physics Rep. Prog. Phys*, vol. 57, pp. 895–938, 1994.

[9] O. Hayes Griffith and W. Engel, "Historical perspective and current trends in emission microscopy, mirror electron microscopy and low-energy electron microscopy: An introduction to the proceedings of the second international symposium and workshop on emission microscopy and related techn," *Ultramicroscopy*, vol. 36, pp. 1–28, 5 1991.

[10] R. M. Tromp, "Low-energy electron microscopy," *IBM Journal of Research and Development*, vol. 44, pp. 503–516, 7 2000.

[11] H.-W. Fink, W. Stocker, and H. Schmid, "Holography with low-energy electrons," *Physical Review Letters*, vol. 65, pp. 1204–1206, 9 1990.

[12] J.-N. Longchamp, T. Latychevskaia, C. Escher, and H.-W. Fink, "Low-energy electron holographic imaging of individual tobacco mosaic virions," *Applied Physics Letters*, vol. 107, p. 133101, 9 2015.

[13] O. H. Griffith, K. K. Hedberg, D. Desloge, and G. F. Rempfer, "Low-energy electron microscopy (LEEM) and mirror electron microscopy (MEM) of biological specimens: Preliminary results with a novel beam separating system," *Journal of Microscopy*, vol. 168, pp. 249–258, 12 1992.

[14] G. F. Rempfer and O. Hayes Griffith, "Emission microscopy and related techniques: Resolution in photoelectron microscopy, low energy electron microscopy and mirror electron microscopy," *Ultramicroscopy*, vol. 47, no. 1-3, pp. 35–54, 1992.

[15] F. Martin, P. D. Burrow, Z. Cai, P. Cloutier, D. Hunting, and L. Sanche, "DNA Strand Breaks Induced by 0–4 eV Electrons: The Role of Shape Resonances," *Physical Review Letters*, vol. 93, p. 068101, 8 2004.

[16] E. Bauer, "The resolution of the low energy electron reflection microscope," *Ultramicroscopy*, vol. 17, pp. 51–56, 1 1985.

[17] R. Henderson, "The potential and limitations of neutrons, electrons and X-rays for atomic resolution microscopy of unstained biological molecules," *Quarterly Reviews of Biophysics*, vol. 28, no. 2, pp. 171–193, 1995.

[18] H. Yang, R. N. Rutte, L. Jones, M. Simson, R. Sagawa, H. Ryll, M. Huth, T. J. Pennycook, M. Green, H. Soltau, Y. Kondo, B. G. Davis, and P. D. Nellist, "Simultaneous atomic-resolution electron ptychography and Z-contrast imaging of light and heavy elements in complex nanostructures," *Nature Communications*, vol. 7, p. 12532, 8 2016.

[19] K. Nagayama and R. Danev, "Phase-plate electron microscopy: a novel imaging tool to reveal close-to-life nano-structures.," *Biophysical reviews*, vol. 1, pp. 37–42, 3 2009.

[20] H. Lichte, "ELECTRON HOLOGRAPHY APPROACHING ATOMIC RESOLUTION *," *Ultramicroscopy*, vol. 20, pp. 293–304, 1986.

[21] E. Knapek and J. Dubochet, "Beam damage to organic material is considerably reduced in cryo-electron microscopy," *Journal of Molecular Biology*, vol. 141, pp. 147–161, 8 1980.

[22] J. L. S. Milne, M. J. Borgnia, A. Bartesaghi, E. E. H. Tran, L. A. Earl, D. M. Schauder, J. Lengyel, J. Pierson, A. Patwardhan, and S. Subramaniam, "Cryo-electron microscopy - a primer for the non-microscopist," *FEBS Journal*, vol. 280, pp. 28–45, 1 2013.

[23] E. E. H. Tran, M. J. Borgnia, O. Kuybeda, D. M. Schauder, A. Bartesaghi, G. A. Frank, G. Sapiro, J. L. S. Milne, and S. Subramaniam, "Structural Mechanism of Trimeric HIV-1 Envelope Glycoprotein Activation," *PLoS Pathogens*, vol. 8, p. e1002797, 7 2012.

[24] J.-N. Longchamp, T. Latychevskaia, C. Escher, and H.-W. Fink, "Non-destructive imaging of an individual protein," *Applied Physics Letters*, vol. 101, p. 093701, 8 2012.

[25] V. Giovannetti, S. Lloyd, and L. Maccone, "Quantum-enhanced measurements: beating the standard quantum limit.," *Science (New York, N.Y.)*, vol. 306, pp. 1330–6, 11 2004.

[26] C. M. Caves, "Quantum-mechanical noise in an interferometer," *Physical Review D*, vol. 23, pp. 1693–1708, 4 1981.

[27] J. P. Dowling, "Correlated input-port, matter-wave interferometer: Quantum-noise limits to the atom-laser gyroscope," *Physical Review A*, vol. 57, pp. 4736–4746, 6 1998.

[28] A. C. Elitzur and L. Vaidman, "Quantum Mechanical Interaction-Free Measurements," *Foundations of Physics*, vol. 23, no. 7, 1993.

[29] P. Kwiat, H. Weinfurter, T. Herzog, A. Zeilinger, and M. A. Kasevich, "Interaction-Free Measurement," *HYSICAL .REVIEW*, vol. 74, 1995.

[30] W. P. Putnam and M. F. Yanik, "Noninvasive electron microscopy with interaction-free quantum measurements," *Physical Review A*, vol. 80, p. 040902, 10 2009.

[31] P. Kruit, R. Hobbs, C.-S. Kim, Y. Yang, V. Manfrinato, J. Hammer, S. Thomas, P. Weber, B. Klopfer, C. Kohstall, T. Juffmann, M. Kasevich, P. Hommelhoff, and K. Berggren, "Designs for a quantum electron microscope," *Ultramicroscopy*, vol. 164, pp. 31–45, 2016.

[32] T. Juffmann, B. B. Klopfer, T. L. Frankort, P. Haslinger, and M. A. Kasevich, "Multi-pass microscopy," *Nature Communications*, vol. 7, p. 12858, 9 2016.

[33] T. Juffmann, S. A. Koppell, B. B. Klopfer, C. Ophus, R. M. Glaeser, and M. A. Kasevich, "Multi-pass transmission electron microscopy," *Scientific Reports*, pp. 1–7, 2017.

[34] N. Abedzadeh, M. A. Krielaart, C. S. Kim, J. Simonaitis, R. Hobbs, P. Kruit, and K. K. Berggren, "Electrostatic electron mirror in SEM for simultaneous imaging of top and bottom surfaces of a sample," *Ultramicroscopy*, vol. 226, no. April, p. 113304, 2021.

[35] G. Hottenroth, "über Elektronenspiegel," *Zeitschrift für Physik*, vol. 103, p. 460, 1936.

[36] G. Hottenroth, "Untersuchungen über Elektronenspiegel," *Annalen der Physik*, vol. 30, no. 5, p. 689, 1937.

[37] R. Orthuber, "Über die Anwendung des Elektronenspiegels zum Abbilden der Potentialverteilung auf metallischen und Halbleiteroberflächen," *Z. angew. Phys.*, vol. 1, p. 79, 1948.

[38] R. M. Oman, "Electron Mirror Microscopy," *Advances in Electronics and Electron Physics*, vol. 26, pp. 217–250, 1969.

[39] A. E. Luk'yanov, G. V. Spivak, and R. S. Gvozdover, "Mirror Electron Microscopy," *Soviet Physics Uspekhi*, vol. 16, no. 4, p. 529, 1974.

[40] W. Telieps and E. Bauer, "An analytical reflection and emission UHV surface electron microscope," *Ultramicroscopy*, vol. 17, no. 1, pp. 57–65, 1985.

[41] R. M. Tromp and M. C. Reuter, "Design of a new photo-emission/low-energy electron microscope for surface studies," *Ultramicroscopy*, vol. 36, no. 1-3, pp. 99–106, 1991.

[42] R. M. Tromp, "Low-energy electron microscopy," *IBM J. RES. DEVELOP.*, vol. 44, no. 4, pp. 503–516, 2000.

[43] G. F. Rempfer, "A theoretical study of the hyperbolic electron mirror as a correcting element for spherical and chromatic aberration in electron optics," *Journal of Applied Physics*, vol. 67, no. 10, pp. 6027–6040, 1990.

[44] G. F. Rempfer, D. M. Desloge, W. P. Skoczylas, and O. H. Griffith, "Simultaneous correction of spherical and chromatic aberrations with an electron mirror: An electron optical achromat," *Microscopy and Microanalysis*, vol. 3, no. 1, pp. 14–27, 1997.

[45] R. M. Tromp, J. B. Hannon, W. Wan, A. Berghaus, and O. Schaff, "A new aberration-corrected, energy-filtered LEEM/PEEM instrument II. Operation and results," *Ultramicroscopy*, vol. 110, pp. 825–861, 2010.

[46] M. Turchetti, C. S. Kim, R. Hobbs, Y. Yang, P. Kruit, and K. K. Berggren, "Design and simulation of a linear electron cavity for quantum electron microscopy," *Ultramicroscopy*, vol. 199, no. February, pp. 50–61, 2019.

[47] A. V. Crewe, S. Ruan, P. Korda, and F. C. Tsai, "Studies of a magnetically focused electrostatic mirror . I . Experimental test of the first order properties," vol. 197, pp. 110–117, 2000.

[48] H. Andersson and C. Persson, "In-situ SEM study of fatigue crack growth behaviour in IN718," *International Journal of Fatigue*, vol. 26, no. 3, pp. 211–219, 2004.

[49] E. A. Torres and A. J. Ramírez, "In situ scanning electron microscopy," *Science and Technology of Welding and Joining*, vol. 16, no. 1, pp. 68–78, 2011.

[50] W. Wan, J. Feng, and H. A. Padmore, "A new separator design for aberration corrected photoemission electron microscopes," *Nuclear Instruments and Methods in Physics Research, Section A: Accelerators, Spectrometers, Detectors and Associated Equipment*, vol. 564, no. 1, pp. 537–543, 2006.

[51] H. Dohi and P. Kruit, "Design for an aberration corrected scanning electron microscope using miniature electron mirrors," *Ultramicroscopy*, vol. 189, pp. 1–23, 2018.

[52] G. F. Rempfer and O. H. Griffith, "The resolution of photoelectron microscopes with UV, X-ray, and synchrotron excitation sources," *Ultramicroscopy*, vol. 27, no. 3, pp. 273–300, 1989.

[53] C. B. Carter and D. B. Williams, "Transmission electron microscopy: Diffraction, imaging, and spectrometry," *Transmission Electron Microscopy: Diffraction, Imaging, and Spectrometry*, pp. 1–518, 2016.

[54] M. Krielaart and P. Kruit, "Flat electron mirror," *Ultramicroscopy*, vol. 220, no. October 2020, p. 113157, 2021.

[55] M. A. R. Krielaart and P. Kruit, "Grating mirror for diffraction of electrons," *Physical Review A*, vol. 98, no. 6, p. 063806, 2018.

[56] H. Okamoto, "Adaptive quantum measurement for low-dose electron microscopy," *Physical Review A - Atomic, Molecular, and Optical Physics*, vol. 81, no. 4, pp. 1–16, 2010.

[57] P. Kruit, "The role of MEMS in maskless lithography," *Microelectronic Engineering*, vol. 84, no. 5-8, pp. 1027–1032, 2007.

[58] P. Kruit, "Introduction to Charged Particle Optics," *Unpublished Lecture Notes*, 2014.

[59] N. Abedzadeh, *Diffractive Electron Mirror for Use in Quantum Electron Microscopy*. PhD thesis, Massachusetts Institute of Technology, 2018.

[60] M. E. Walsh, "On the design of lithographic interferometers and their application," no. 1997, pp. 1–300, 2004.

[61] R. Tromp, "Towards 2 λ Resolution (Limits of Aberration Corrected Electron Microscopy)," *Unpublished Lecture Notes*.

[62] S. Kennedy, C. Zheng, W. Tang, D. Paganin, and D. Jesson, "Caustic imaging of gallium droplets using mirror electron microscopy," *Ultramicroscopy*, vol. 111, pp. 356–363, 4 2011.

[63] H. Lichte, "Coherent electron optical experiments using an electron mirror," *Proceedings of the international symposium foundations of quantum mechanics in the light of new technolog*, no. 16072908, pp. 29–31, 1983.

[64] S. A. Koppell, M. Mankos, A. J. Bowman, Y. Israel, T. Juffmann, B. B. Klopfer, and M. A. Kasevich, "Design for a 10 keV multi-pass transmission electron microscope," *Ultramicroscopy*, vol. 207, no. April, 2019.

[65] T. R Harvey, J. S Pierce, A. K Agrawal, P. Ercius, M. Linck, and B. J. McMorran, "Efficient diffractive phase optics for electrons," *New Journal of Physics*, vol. 16, 2014.

[66] T. K. Werner Lauterborn, *Coherent Optics: Fundamentals and Applications*. Springer, 2003.

[67] M. Wanner, D. Bach, D. Gerthsen, R. Werner, and B. Tesche, "Electron holography of thin amorphous carbon films: Measurement of the mean inner potential and a thickness-independent phase shift," *Ultramicroscopy*, vol. 106, no. 4-5, pp. 341–345, 2006.

[68] Y. Yang, C. S. Kim, R. G. Hobbs, P. Kruit, and K. K. Berggren, "Efficient two-port electron beam splitter via a quantum interaction-free measurement," *Physical Review A*, vol. 98, no. 4, pp. 1–8, 2018.

[69] D. Cooper, C. T. Pan, and S. Haigh, "Atomic resolution electrostatic potential mapping of graphene sheets by off-axis electron holography," *Journal of Applied Physics*, vol. 115, no. 23, 2014.

[70] M. Tripathi, A. Mittelberger, K. Mustonen, C. Mangler, J. Kotakoski, J. C. Meyer, and T. Susi, "Cleaning graphene: Comparing heat treatments in air and in vacuum," *Physica Status Solidi - Rapid Research Letters*, vol. 11, no. 8, 2017.

[71] T. C. Isabell, P. E. Fischione, C. O'Keefe, M. U. Guruz, and V. P. Dravid, "Plasma cleaning and its applications for electron microscopy," *Microscopy and Microanalysis*, vol. 5, no. 2, pp. 126–135, 1999.

[72] J. Wall, "Contamination in the STEM at ultra high vacuum," *Scanning electron microscopy*, vol. 1980, pp. 99–106, 1980.

[73] G. Algara-Siller, O. Lehtinen, A. Turchanin, and U. Kaiser, "Dry-cleaning of graphene," *Applied Physics Letters*, vol. 104, no. 15, 2014.

[74] B. McMorran, J. D. Perreault, T. A. Savas, and A. Cronin, "Diffraction of 0.5 keV electrons from free-standing transmission gratings," *Ultramicroscopy*, vol. 106, no. 4-5, pp. 356–364, 2006.

[75] B. McMorran and A. D. Cronin, "Model for partial coherence and wavefront curvature in grating interferometers," *Physical Review A - Atomic, Molecular, and Optical Physics*, vol. 78, no. 1, pp. 1–10, 2008.

[76] C. Brand, M. Sclafani, C. Knobloch, Y. Lilach, T. Juffmann, J. Kotakoski, C. Mangler, A. Winter, A. Turchanin, J. Meyer, O. Cheshnovsky, and M. Arndt, "An atomically thin matter-wave beamsplitter," *Nature Nanotechnology*, vol. 10, no. 10, pp. 845–848, 2015.

[77] S. Uhlemann, H. Müller, P. Hartel, J. Zach, and M. Haider, "Thermal magnetic field noise limits resolution in transmission electron microscopy," *Physical Review Letters*, vol. 111, no. 4, pp. 1–5, 2013.